Influence of Strain Rate Sensitivity (SRS) of Additive Manufactured Ti-6Al-4V on Nanoscale Wear Resistance

by

Angelo Pelini

Submitted in Partial Fulfillment of the Requirements

for the Degree of

Master of Science in Engineering

in the

Mechanical Engineering

Program

YOUNGSTOWN STATE UNIVERSITY

December, 2017

Influence of Strain Rate Sensitivity (SRS) of Additive Manufactured Ti-6Al-4V on Nanoscale Wear Resistance

Angelo Pelini

I hereby release this thesis to the public. I understand that this thesis will be made available from the OhioLINK ETD Center and the Maag Library Circulation Desk for public access. I also authorize the University or other individuals to make copies of this thesis as needed for scholarly research.

Signature:

_____

Angelo Pelini, Student Date

Approvals:

_____

Dr. Jae Joong Ryu, Thesis Advisor Date

_____

Dr. Hazel Marie, Committee Member Date

_____

Dr. Jason Walker, Committee Member Date

_____

Dr. Salvatore A. Sanders, Dean of Graduate Studies Date

Abstract

The widespread use of titanium alloys such as Ti-6Al-4V and the expense of manufacturing it, leads to a need of new manufacturing processes such as the innovative additive manufacturing technology of today. Ti-6Al-4V was studied in a series of experiments to determine the strain rate sensitivity of the material that was manufactured by conventional, mill-annealing, and additive manufacturing processes of electron beam melting and selective laser melting. Due to the high thermal cycles required in the hatching processes involved in building each layer of the part, and the rapid cooling, the grain size of dual phase titanium becomes very fine. Grain structure of each manufacturing process was studied and compared with the results. Constant rate of loading tests were performed on all three samples. Then the samples were tested in a multiple loading test where it was loaded at increasing maximum peak loads four times. The application of run-in wear can cause high friction where single asperity contact causes wear. Because of this, progressive scratch tests were performed at different loading rates and sliding speeds to compare to the indentation tests. Results show that grain size and structure influence the strain rate sensitivity as well as the scratch loading rate sensitivity. The results also show that the strain rate was affected by the fatigue induced by the multiple peak loads involved in the second test.

Table of Contents

List of Figures

List of Tables

List of Abbreviations

Abbreviation	Definition
3D	3-Dimensional
AM	Additive Manufacturing
ASTM	American Society of Testing and Materials
CAD	Computer Aided Design
CAM	Computer Aided Manufacturing
CL	Constant Load
CLA	CenterLine Average
CNC	Computer Numerical Control
CRL	Constant Rate Loading
CSR	Constant Strain Rate
E	Modulus of Elasticity
EBM	Electron Beam Melting
EDX	Energy-Dispersive X-Ray Spectroscopy
HF	Hydrogen Flouride
HM	Martens Hardness
HNO_3	Nitric Acid
HV	Vickers Hardness
Kc	Fracture Toughness
MA	Mill-Annealed
Ms	Martensite Start
S	Stiffness

SEM	Scanning Electron Microscope
SiNi	Silicon Nitride
SLM	Selective Laser Melting
SRS	Strain Rate Sensitivity
Sy	Yield Strength
Ti64	Titanium Alloy Ti-6Al-4V
XRD	X-Ray Diffraction

CHAPTER 1: INTRODUCTION

1.1 Background

1.1.1 Ti-6Al-4V

The titanium alloy, Ti-6Al-4V, often abbreviated Ti64, has some desirable characteristics, including high tensile strength, toughness, and corrosive resistivity. These characteristics make it an exceptional material. Additional characteristics such as corrosive resistivity and biomedical compatibility make it excellent for medical applications such as total joint replacement or dental implants. Combining this with other characteristics such as the low density and its temperature resistivity make it ideal for aerospace and chemical applications (1). Ti64 is the most widely used titanium alloy (2).

Titanium is often expensive to produce because titanium parts are difficult to make. Generally, the part must be cast into shape, and then finally machined to net size. In the case of medical implants, the part will then need polished for final assembly. This process is limiting on size and time requirements. A suggested alternative is to use near net additive manufacturing to create these complex parts and reduce machining time as well as increase specialized shape availability.

Ti-6Al-4V is of special interest as it is shown to have promising ability to be powdered and used in additive manufacturing processes. Using a method such as this would create less time and resource consumption in manufacturing of components made from titanium alloys.

1.1.2 Additive Manufacturing

Additive Manufacturing (AM) is a general term used for a type of part manufacturing that involves adding material to create parts and features, rather than the

more conventional method of subtracting material from a piece of stock. Usually a designer creates a model using Computer Aided Design (CAD) software and then creates printing instructions using Computer Aid Manufacturing (CAM) software. These instructions are fed to a Computer Numerical Control (CNC) machine that builds material in such a fashion that a thin layer is repeatedly added to the top of the surface until the shape is created.

There are several types of additive manufacturing methods available with several different materials. These materials can range from wax, resins, ceramics, metal, polymer, and plastics. The two most common printers produce parts made from plastics or metals. Colloquially, the term "3D Printing" is most often used when referring to printing with plastics or polymers and the term "Additive Manufacturing" is used when referring to printing with metals. ASTM F2792 lists seven families of processes:

- *Vat Photopolymerization*: Liquid resin is contained in a vat where a laser converts the top layer of the resin to solid and the solid moves down to expose a new layer of liquid.
- *Powder Bed Fusion*: Sintered material is laid on a bed where a laser melts the uppermost layer before a new layer of powder is added.
- *Binding Jetting*: A liquid glue or resin is applied to a layer of powdered material to bind the material together in that location. Then a new layer of powder is added.
- *Material Jetting*: Liquid material is sprayed one thin layer at a time and then cured either by cooling or by some other method such as ultraviolet light.

- *Sheet Lamination*: Thin sheets of specific shape are laminated together to create the object.
- *Material Extrusion*: Material is fed through an extruder and applied as a thin layer to create the object.
- *Direct Energy Deposition*: Material is fed into a small, melted area of base material where it will freeze and create a new layer for the process to continue.

There are two specific processes that are of particular interest to this paper and they are Selective Laser Melting (SLM) and Electron Beam Melting (EBM). Both of these processes fall under the powder bed fusion family, but each are unique.

SLM was originally introduced in the 1980's and like many other AM processes, it has been continually improved on since. Today, it is one of the most common methods of additive manufacturing due to its high precision and high speed of manufacture. The process of SLM involves the use of a power bed of material inside a cylinder surrounded by an inert gas. Once a high-powered laser is reflected onto the bed, it melts a pool of metal which quickly freezes to create a layer of the object. A new layer is then established by lowering the cylinder and filling the bed with more powder. As each layer is built, the material gains thickness in that direction. The thickness of the layer is based on the particle size and is usually in the range of 50μm.

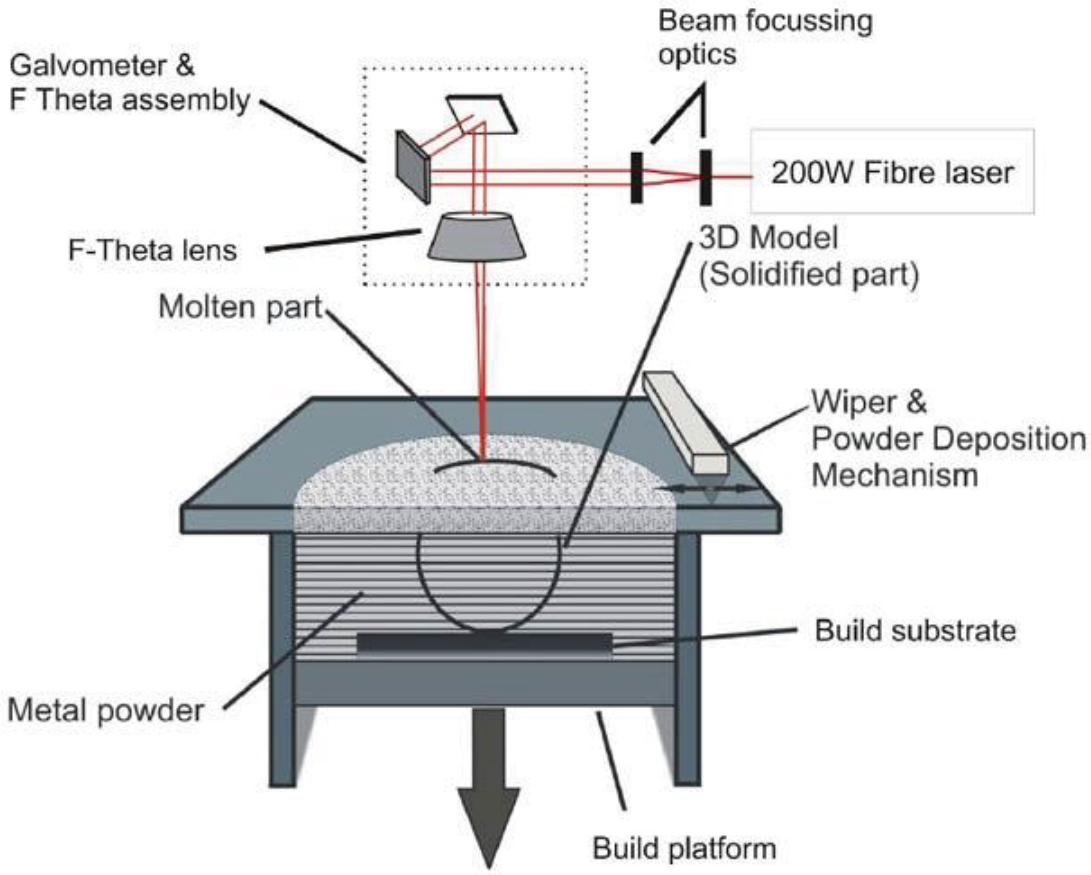

Figure 1: Diagram of Selective Laser Melting (SLM) process. (3)

The process of EBM is similar to the SLM process; however, it uses an electron beam in a vacuum to melt the metal into a pool which causes built in stress relief. Where SLM creates porosity in the final product, EBM creates a perfectly dense part during its manufacturing. Not only this, but certain EBM manufactures have the ability to use multiple beams at once creating an even faster result. (4)

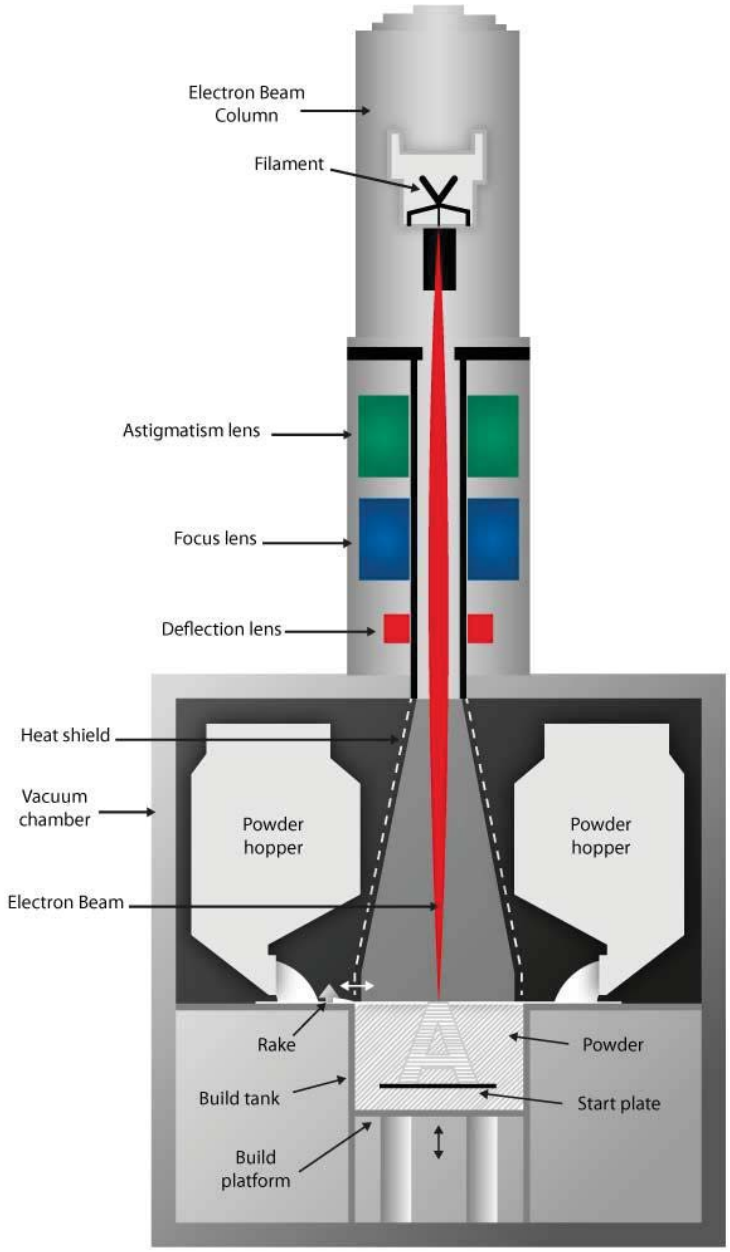

Figure 2: Diagram of EBM process. (4)

Since both of these processes involve constructing the object layer by layer, it is important to note the direction of build for the sample. The surface in question could be parallel to the build direction or perpendicular and it is known that this will affect material characteristics such as tensile properties, ductility and fatigue resistance (5).

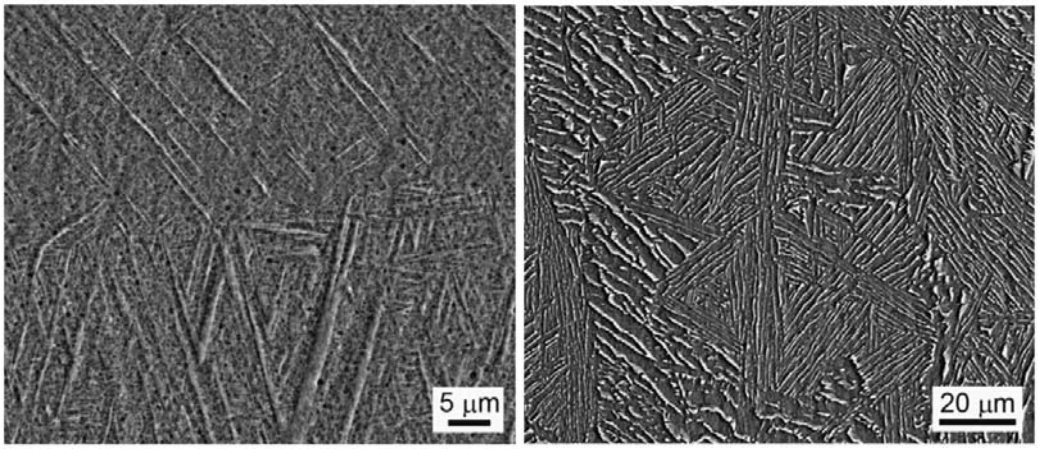

Figure 3: SEM Image of SLM (left) and EBM (right) built samples (6).

1.1.3 Nanoindentation

Although there are several methods of determining material properties, few can characterize local behavior. Nanoindentation is a process of pushing an indenter with known geometry into a surface of a material to determine the material properties. As the indenter is loaded or unloaded using a piezo sensor, the travel depth of the indenter is precisely measured using a capacitor. Using this information some characteristics that can be found are hardness, yield strength, elastic modulus, and toughness.

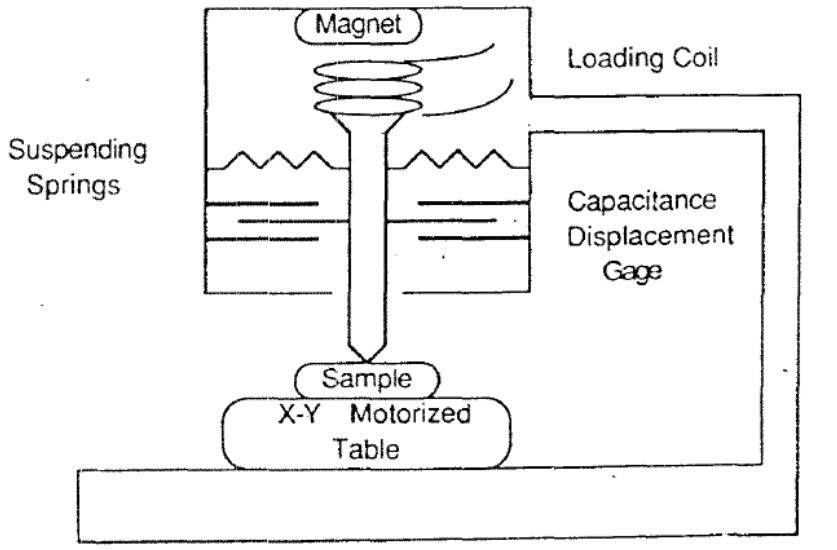

Figure 4: Diagram of traditional nanoindentation machine (6)

Some common indenter shapes that are used with nanoindentation are:

- Conical
- Vickers
- Berkovich
- Cylindrical Flat Tip
- Spherical

The indenters of interest here are the Berkovich and spherical indenters. A Berkovich tip is a self-similar pyramid shaped indenter with three sides and an included angle of 142.3°. It has the same area function (used to determine contact area when depth is known) as the Vickers and conical indenter, but it is generally easier to manufacture the point. The tip is made from a hard, stiff material; usually diamond. This is to help prevent wear and to keep flexibility to a minimum for accurate data collection.

During a typical test, an indenter is plunged into the material sample with a specified load and loading rate. At the peak load, it is retracted, again with a specified loading rate. The properties of the material can be measured from this data (7) (8).

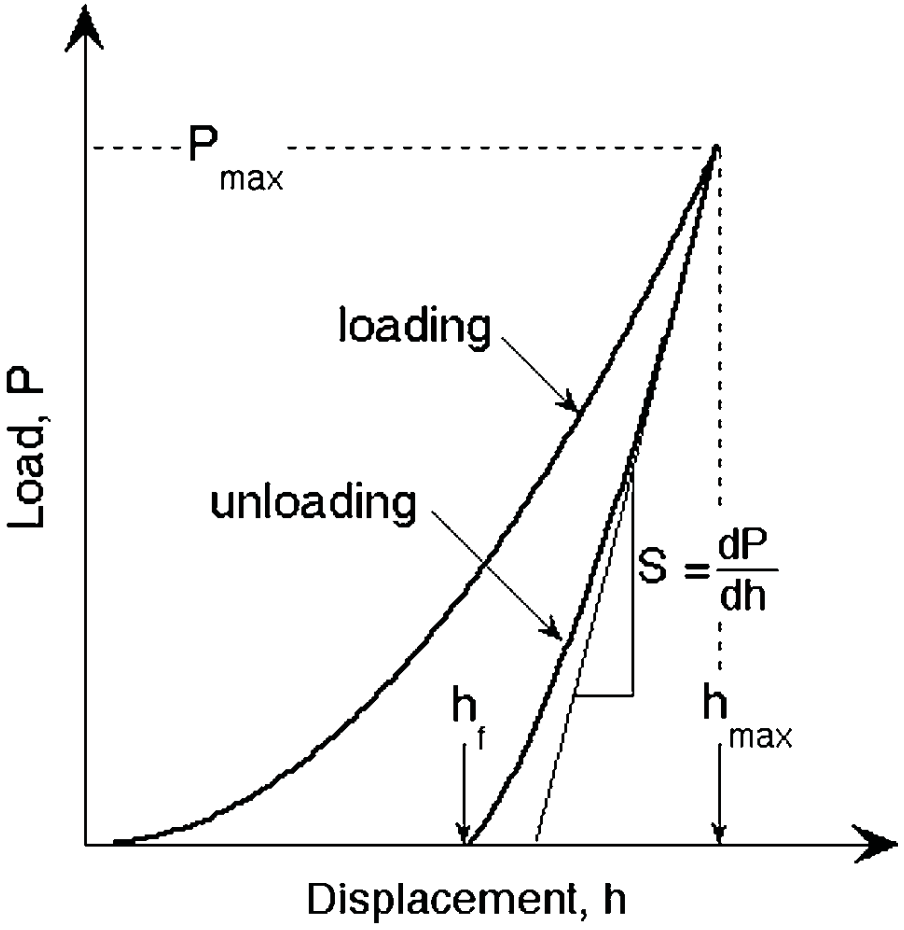

Figure 5: Typical Load vs Displacement Curve for a Nanoindentation Test (9)

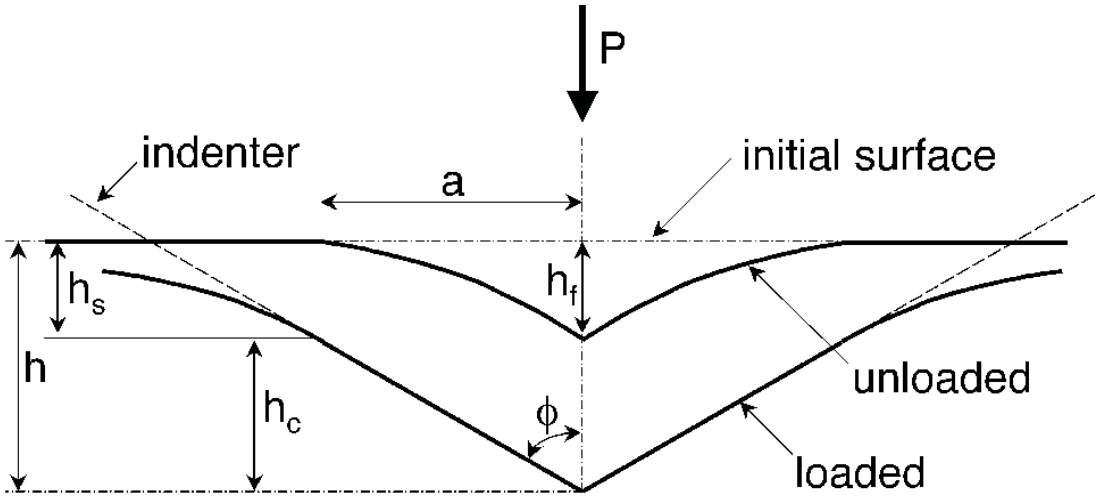

Figure 6: Surface loading and residual depth left after unloading (9)

- *Vickers Hardness (HV)*: This is a measure of the load applied to a self-similar tip divided by the projected residual contact area left when the tip is retracted.

$$HV = \frac{P_{max}}{A_c} \quad \text{Eq. (1)}$$

- *Martens Hardness (HM)*: Similar to Vickers hardness, but the area used is the area under peak load.

$$HM = \frac{P_{max}}{A_{max}} \quad \text{Eq. (2)}$$

- *Yield Strength (Sy)*: It is shown that using a cylindrical, flat tip indenter can produce reliable yield strength calculations by finding the inflection point in the load vs. depth curve (10).
- *Fracture Toughness (Kc)*: As the sample is loaded, the fracture toughness can be visually measured from the cracks from the residual mark on the material.

$$K_c = \alpha \left(\frac{E}{H}\right)^{\frac{1}{2}} \left(\frac{P}{c^{\frac{3}{2}}}\right) \quad \text{Eq. (3)}$$

- *Stiffness (S)*: Measured with the load vs depth curve by taking the slope at initial unloading.

$$S = \frac{dP}{dh_{peak\ unloading}} \quad \text{Eq. (4)}$$

- *Modulus of Elasticity (E)*: Calculated using the wide accepted Oliver & Pharr method of power function match of the unloading curve of load vs depth.

$$E = \frac{\frac{\sqrt{\pi}}{2}S}{\sqrt{A_c}} \qquad \text{Eq. (5)}$$

- *Creep*: At peak load, the load can be help constant for a duration to determine any change in depth.
- *Strain rate sensitivity*: There are several methods that will be discussed on using an indentation test to derive strain rate sensitivity.

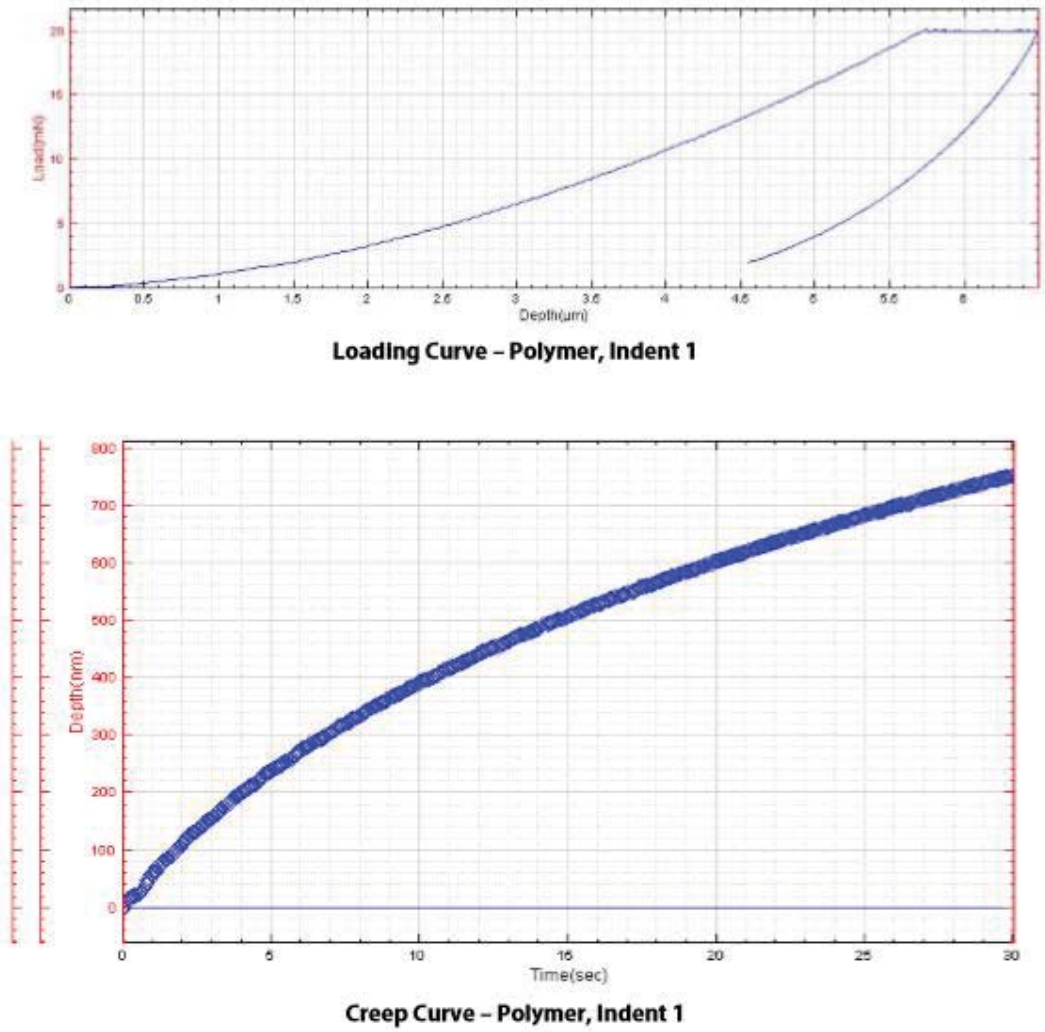

Figure 7: Diagram showing load vs depth curve to describe a typical creep test (8)

There are limitations to nanoindentation testing that need to be accounted for. When calculating area of the surface, the area function mentioned before is used. An ideal area function would have this format:

$$A = Ch^2 \qquad \text{Eq. (6)}$$

Where A is the area, C is the geometric correction factor, and h is the depth. For an ideal Berkovich indenter, C is equal to 24.5. However, since it is impossible to manufacture anything to ideal, it is important to calibrate the indenter. In most machines, calibration to

a new area function will be inclusive of not only incorrect geometry, but also deflection of the frame of the machine which would distort depth readings. The output is a polynomial function of usually less than seven degrees (11). More than seven degrees can cause the polynomial to follow the noise of the indentation instead of the general curve.

$$A = C_1h^2 + C_2h + C_3h^{\frac{1}{2}} + C_4h^{\frac{1}{4}} \ldots \quad \text{Eq. (7)}$$

Another issue with nanoindentation is thermal drift. Thermal drift generally comes from an expansion or contraction of the tip material due to changes in temperature while testing. This can cause the indenter tip to go into or out of the material. Since it is constantly changing during the test, it is difficult to compensate for. The result is that the depth sensor readings can be higher or lower than actual results and compensation for it is an estimate at best (11).

1.1.4 Panoramic vs Local Characteristics

Since many of these properties can be measured with a traditional macroindentation method, it's important to mention differences associated with each. Macroindentation techniques use the entire sample or a large portion of the sample to measure average material properties across the sample. In nanoindentation, it is possible to measure a shallow thickness of the material. It is also possible to measure in such a way that data is collected on a localized location. When a sample is needed for a tribological task, the material characteristics that help determine wear properties are based on local asperities of the surface, therefore it is more valuable to obtain data on a local level than a macro level. Macroindentation can provide results of strain rate sensitivity and yield strength by an ultimate tensile test of the material whereas it cannot determine if those properties relate to wear on a single grain of the material.

1.1.5 Dependence of Wear on Strain Rate Sensitivity

Although nanoindentation is primarily used for hardness and elastic modulus measurements, new studies are using nanoindenters to study time dependent characteristics such as creep and strain rate hardness. Strain rate sensitivity (SRS) is a material property that makes the object yield at different points depending on the rate at which it is deformed. There are a few methods of calculating strain rate sensitivity using nanoindentation.

- *Constant Rate of Loading (CRL):* Mayo and Nix provided this method of studying plastic deformation in materials. The indenter is plunged into the material, increasing force at a constant rate. Several tests are completed with each test using a constant loading rate. The combination of the tests with different loading rates provide accurate strain rate sensitivity. (12)
- *Constant Strain Rate (CSR):* The indenter is plunged into the material with load varying per an exponential function to keep strain rate constant. Again, multiple tests are done with varying strain rate. (13)
- *Constant Load (CL):* The sample is rapidly loaded and held at the maximum load for a duration long enough for displacement to change at a constant rate. (14)
- *Strain Jump:* A relatively new method where the exponential loading rate is changed for a section or several sections of the loading portion of the test. (15)

There are some drawbacks for each case which must be considered before a method is decided. The Constant Strain Rate and the Constant Load method require several indentation points to determine the strain rate sensitivity. This can spread data points over a large area on the surface.

In the case of the Constant Load method, thermal drift can add up to significant error in the solution unless a large displacement is used. With large displacement, the material tip can pass through several grains of an additive manufactured material and the resulting hardness values would not be representative of the surface where wear contact would happen.

Strain jump is a rather new concept and seems to account for both of these drawbacks however, many nanoindentation machines do not have software and PID controller capabilities to perform a test like this.

Strain rate sensitivity is known to have a power law relationship with flow stress as follows:

$$\sigma_F = K(\dot{\epsilon}_F)^m \qquad \text{Eq. (8)}$$

Where σ_F is the flow stress, K is the material constant, $\dot{\epsilon}_F$ is the flow strain rate, and m is the strain rate sensitivity.

For a hardness test, the strain rate is calculated as:

$$\dot{\epsilon} = \frac{\dot{h}}{h_{max}} \qquad \text{Eq. (9)}$$

Where $\dot{h}$ is the change in depth and h_{max} is the maximum depth of the indentation.

The strain rate sensitivity (m) is then calculated by:

$$m = \frac{dln(HM)}{dln(\dot{\epsilon})} \quad \text{Eq. (10)}$$

Several studies show that strain rate sensitivity is affected by temperature, so it is important that the strain rate sensitivity be determined by holding temperature constant.

1.1.6 Grain Morphology of Additive Manufactured Components

The microstructure of Ti-6Al-4V is made up of a α + β matrix. However, the method used in processing can change whether it is bi-modal, lamellar, or equiaxed.

Specifically, the cooling rate can determine how the β phase transforms. For example, if it is cooled rapidly, there will be a martensitic transformation of the β phase (5). Regardless of manufacturing method, the primary mode of solidification always remains β (16).

Titanium manufactured from conventional milling and annealing processes, sometimes referred to as wrought, generally show fully equiaxed microstructure with intergranular β between the α grains and α/β colonies.Er

When Ti-6Al-4V is produced from SLM process, the rapid cooling of the melted material does not give the β phase time to transform and results in a fine α' phase with a much smaller grain size. Usually resulting in a lamellar or basket-weave morphology and completely martensitic. However, the scanning parameters used in SLM can greatly affect the microstructure due to the high localized heat, short interaction times, local heat transfer conditions, scanning velocity and hatch spacing (16). In general, changing the quantity of energy delivered will change the output grain structure (2).

When samples are produced via the EBM process, the result is an acicular α with associated β. There is very little β in the results, but the β grain boundaries are columnar. The difference is associated with the higher temperatures in the build chamber which are above the Martensite start (Ms) temperature for Ti64. Even though the EBM cools rapidly at the highest temperatures, the isothermal temperature is high enough that it prohibits the transformation of α to α' (16).

The grain structure plays a critical role in determining material characteristics for the sample used. In a martensitic sample, the properties will show high strength and low ductility. Courser acicular α will result in a reduction in tensile strength. It has also been

shown that generally, SLM produced Ti64 is harder than EBM produced which is harder than wrought (16) (17), but again, the parameters that are used in each specific process play a role in grain structure which could affect results significantly. Not only that, but post treatment such as heat treatment or stress relief can also affect grain structure (5). The fractional volume of α and β will also affect the fatigue strength (16).

1.1.7 Dry Sliding Friction and General Wear Mechanisms

Removal of material from one or both of two surfaces in contact is considered wear. This can happen from sliding, rolling, or impact motion of two surfaces. Since it is impossible to make a perfectly flat surface, when two surfaces interact with each other, instead of touching over the entire surface, they are only touching on a few peaks of each surface. For general wear considerations, these asperities are where the wear is happening.

Wear is complex and can be of several forms. Bhushan (18) divides wear into these several functions:

- *Adhesive wear:* When Asperities touch one another, there is a large force over a small contact area. This causes cold-welding. When the surfaces try to slide in different relative directions, that weld needs to break. Usually, it will break at the boundary between the asperities in which case there is no wear, but sometimes it will break into the body of one of the surfaces.

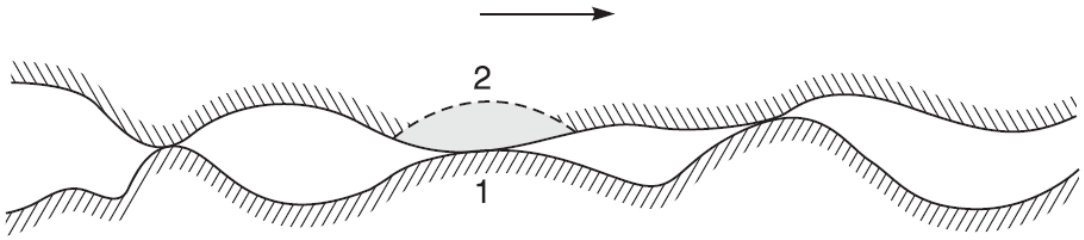

Figure 8: Diagram showing possible breaks during adhesion. If the break happens at the boundary between the surfaces (path 1) there is no wear, but if the break happens into the surface body (path 2) then wear can occur (18).

- *Abrasive wear:* This kind of wear can occur when a much harder surface slides onto a softer surface. At low loads, asperities from the harder surface plastically deform the softer surface or cause fractures via plowing, wedge formation, or cutting. In many cases, wear starts as adhesive which causes hard particles to break off and get trapped in the interface resulting in three body wear. Above a higher threshold load, the wear surface will cause brittle fracture and lateral cracking and a sharply increased rate.

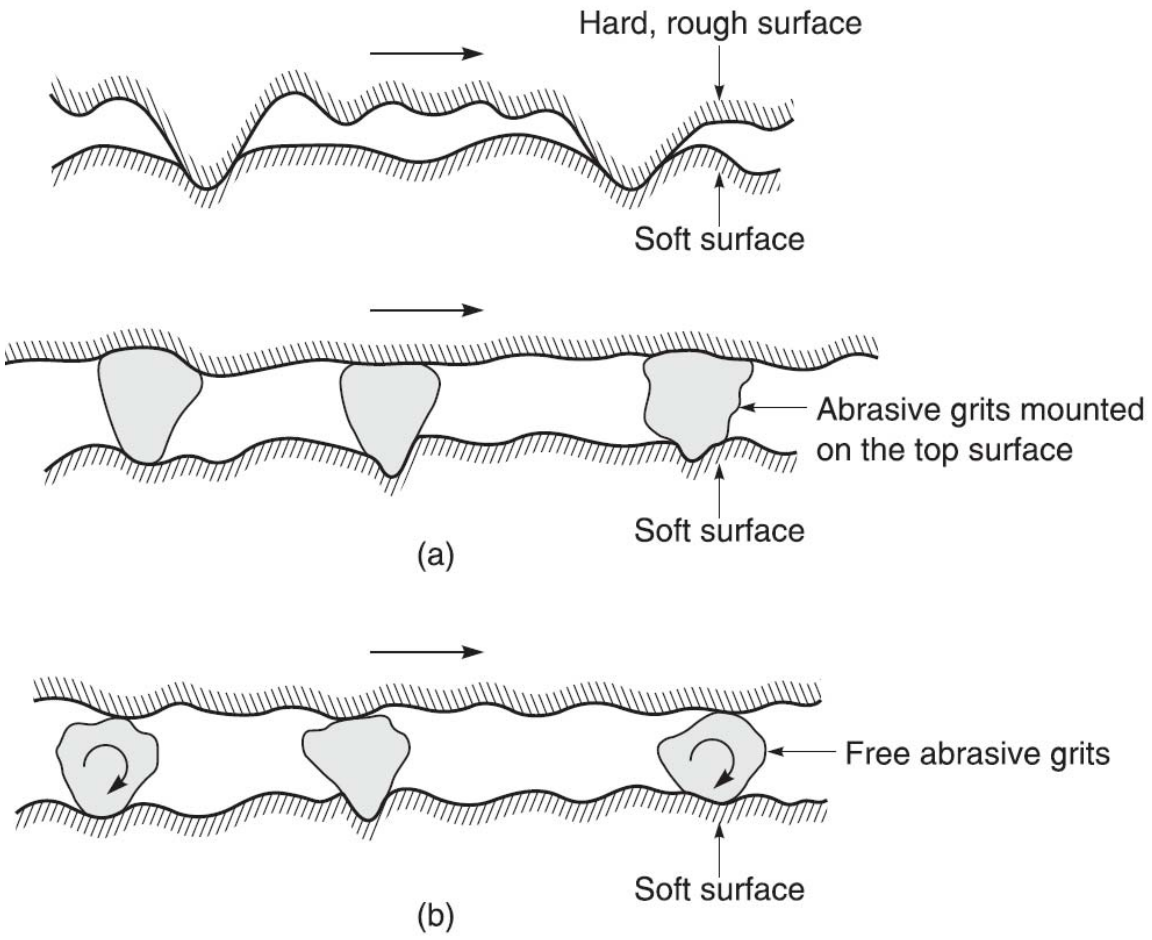

Figure 9: Description of abrasive and three body wear (18).

- *Fatigue wear:* Fatigue happens when repeated loading and unloading cycles cause surface and subsurface cracking. A surface pair subject to repeated sliding motion may have surface fatigue, while a surface pair subject to repeated rolling motion may exhibit subsurface fatigue. As these cracks are forming, there may be negligible wear, but once the fatigue critical point is past, the surface may have large breaks of particles and exhibit very large wear.
- *Impact by Erosion and Percussion:* Erosion occurs as a form of abrasion when particles with kinetic energy inside a stream of air or water encounter a surface.

The repeated encounters induce wear on the surface. Percussion wear occurs when a solid body repeatedly impacts the surface causing surface failures.

- *Chemical Corrosion:* When wear occurs in a corrosive environment (including air), it results in the wearing away of the normally thin, protective, oxide layer that prevents further reaction of the base material with the environment. Once this is worn away, a new layer of base material is exposed to oxide again. Some sources refer to this as tribocorrosion. It is highly important to Ti64 use in the medical field because most instances of replacement joint failures are due to tribocorrosion in the body fluid environment.
- *Electrical-Arc-Induced Wear:* This happens when there is an electrical potential across a thin film. There is an arc that passes onto the second surface and causes a shallow heat affected zone. The result is a melt and solidification of a small section of the surface and a change in material properties. This could be a change in hardness or grain structure. These new material properties can break that piece of material off and cause large craters in the surface.
- *Fretting/Fretting Corrosion:* Fretting occurs when two surfaces that are normally stationary with respect to each other move with a low amplitude oscillatory motion. The normal load between the two components causes initial adhesion and then there is a small oscillatory motion causing repeated ruptures in the surface. These ruptures can result in loose particles changing the primary mechanism for wear from adhesive to three body abrasive wear.

1.1.8 Effect of Grain Morphology on Wear

Wear is a complex action. It is not an internal material property and, instead, is subject to the entire tribo-system which may include physical circumstance and material properties such as yield strength, toughness, and hardness. It may also include other situational properties such as friction.

Given materials under the same circumstance, generally harder materials will wear more or faster than softer materials (19). It has also been shown that there is an increase in hardness with titanium as grain size decreases (20). Although additive manufactured Ti-6Al-4V always have smaller grain size than mill-annealed, the wear rate becomes more complicated than that. There is a study that agrees that wear rate decreases as hardness increases, but also shows that wear rate increases with fracture toughness (21). As well as the smaller grain size in the additive manufactured material, it also has lamellar grain morphology. Research shows lamellar grain morphology can have higher fracture toughness with some titanium alloys (22). Also, bimodal grain structure is reported to have advantages in yield, tensile strength, and ductility which may also contribute to wear rate (23).

There is still more to consider. For many applications of titanium alloys, especially biological applications where titanium is used in joint implants, the mode of wear is fretting or surface fatigue delamination. In this situation, fatigue strength becomes an important quality to consider. It's shown that decreasing grain size in a material reduces fatigue strength in various metals (24). As well, in a study comparing different alloys of titanium without grain size modification, it resulted in a finer grain alloy having greater fatigue strength (21). Also, when high cooling rates are involved, the resulting

martensitic transformation can cause large differences in crystallographic orientation of the lamellae resulting in low coincidence. It takes more energy for the crack to change direction, so it results in a reduction of slip length and instead it must be an intergranular fracture (23).

A general principle that should be noted is the Hall-Petch relationship. This well-known relationship shows an inverse relationship between yield strength and grain size. It is based on the idea that as material is stressed, dislocations occur which cause yielding. When these dislocations reach a grain boundary, they must change direction which requires energy so the more grain boundaries there are, the more resistant the material is to plastic deformation. This implies that the smaller grain boundary will be less susceptible to plastic deformation during wear.

1.1.9 Strain Rate Effect on Wear

Like many metals, Ti-6Al-4V has been shown to have a positive strain rate sensitivity in previous macro experiments including tensile testing, compressive testing, and shear testing (25) (26) (27). This includes a test on strain rate sensitivity for electron beam melted samples (28). The tests show that titanium and alloys generally have a strain rate sensitivity of 0.018-0.03. It is thought that there is significant strain hardening which is the cause for the increase in strength at higher strain rates. In certain wear (pin-on-disk) experiments, there has been a correlation between an increase in plastic flow and higher sliding rates (29).

There are limited sources of strain rate's effect on the wear mechanisms and rate of metals, but what there is shows that at low wear rates, oxidation wear is the primary wear mechanism. However, as wear rate rises, the wear mechanism changes to

delamination. It is important to note that wear rate is not related to the coefficient of friction between the surfaces. It has been shown that as sliding rate increases, friction between the surfaces decreases (30). At lower rates, sliding friction causes an abrasive wear and allows time for oxidation to occur, but also allows time for heat dissipation. At higher sliding rates, thermal effects from friction become a problem as there is less time for heat to dissipate, and less time for oxidation to occur and the result is metallic delamination. Because of this, the result is that the slower sliding rate (strain rate) oxidizing wear is more damaging to the surface than the faster strain rate delamination.

1.2 Motivation

Most sources agree that the manufacturing of titanium alloys is extremely expensive. There is a need for a new manufacturing process for all titanium alloys. Additive manufacturing processes, such as electron beam melting and selective laser melting, could create the cost reductions the market is requiring. However, many applications that use titanium alloys are critical applications that are highly sensitive to failures such as landing struts. This makes a requirement for strong, repetitable research to determine all characteristics of new manufacturing technologies such as additive manufacturing. Given the tribological wear nature of components made from Ti-6Al-4V in applications such as biomedical total joint replacements or dental implants, there needs to be strong proof of the wear nature of these new components that relates strongly to the real situation. There have been studies done on the wear rate of titanium alloys in different situations, however, the results are scattered. This study shows that there is another variable to consider when doing a study on wear behavior: strain rate sensitivity, which includes sliding speed and loading rate of the samples tested.

1.3 Thesis Organization

There are four chapters in this thesis. Chapter 1 presents an introduction to the research and some background prerequisites to reading the other research. Section 1.1 is background on the material properties, grain morphology, manufacturing processes, tools, and formulas used throughout this paper. 1.2 is the motivation for this study and 1.3 is the organization of the paper.

Next is Chapter 2 which details the experimental processes used to determine strain rate sensitivity on a local level using nanoindentation. 2.1 details the materials used for the research of this paper. 2.2 explains the microstructure of the materials due to the different manufacturing processes. 2.3 shows the method and results of the nanoindentation techniques single indentation constant rate loading and multi-load constant rate loading indentations used in this paper.

Chapter 3 involves the experiments done to show a correlation between strain rate and wear rate. Section 3.1 is an introduction to the wear rate involving an overview of the wear mechanics involved. Section 3.2 explains the methods used in the test and the results obtained.

Finally, the conclusion details thoughts on the results shown and recommendations for future work that could be done to further the understanding in the field.

CHAPTER 2: INDENTATION TESTING

2.1 Materials

This paper uses three samples of titanium alloy Ti-6Al-4V produced by three different manufacturing methods. One of wrought (mill-annealed) material, one of electron beam melted material, and one of selective laser melted material.

The mill-annealed sample was used as a control variable to compare the other samples with. It was prepared by first heating to 730°C, then was held for 4 hours and slowly cooled to 25°C. A 25mm diameter bar stock was cut 2.5mm long. It was then cut again into a 2.5mmx15mmx15mm section.

The additive manufactured material was printed using powdered Ti-6Al-4V. For the electron beam melted sample, a particle size of 45-100μm was used on an Arcam A2 machine. The machine was set to default power and feed settings. It was printed into a 15mmx15mmx15mm cube that was cut into 4mm thick sections. The SLM processed material was printed with the default laser and print settings on the machine. It was printed into a 6mmx6mmx9mm cube which was cut into 4mm thick section.

The surface chosen for these tests on the samples of EBM and SLM was perpendicular to the build orientation. Some sources call this surface top or Z.

All 3 samples were then mounted into a stage using a Struers Primopress. Once mounted the rough surface was sanded and polished using a Struers Planopol-2 and a fixed mounting stage used to hold the three samples. Increasingly fine grit paper was used on the samples for 3-5 minutes until the surface was plane. The surface was then polished using Buehler MasterMet Colloidal Silica Polishing Suspension 40-6370-006 until the entire surface had a mirror finish. Using a SharperTEK XP-Pro ultrasonic

machine, the samples were cleaned with acetone, then methanol, then distilled water for 3 minutes in each medium. The surface was then inspected under an optical microscope to ensure no flaws or scratches. The final surface centerline-average roughness was below 0.22μm over a 0.5mm scanning span.

Table 1: Method and order of surface grinding.

Surface Preparation	
Abrasive	Finish
180 Grit	Planar
220 Grit	Planar
320 Grit	Planar
1000 Grit	Planar
2400 Grit	Planar
4000 Grit	Planar
Polishing Suspension	Mirror

The surface was then etched using a solution of Kroll's reagent, a solution of hydrofluoric acid and nitric acid, for 3 minutes. The use of this etchant changes the α phase to a lighter color and the β phase to a darker color making it easier to distinguish intergranular β, and α/β colonies. The microstructures were then visually analyzed.

Table 2: Kroll's reagent (31)

Kroll's Reagent		
H2O	HF	HNO3
100mL	3ml	6ml

2.2 Microstructure

2.2.1 Introduction

Ti-6Al-4V is a dual phase alloy, therefore, the mechanical properties are dependent on the α + β configuration of the microstructure. Specifically, with Ti-6Al-4V, there is 6 parts aluminum to help stabilize the α phase of the material as it cools, and 4

parts vanadium to help stabilize the β phase. When more α stabilizers are present, the α phase is stable at higher temperatures. Conversely, the more β stabilizers in an alloy, the lower the temperature in which the β phase is stable.

In the process of creating titanium parts, the titanium is heated high enough that there is only β phase. The cooling rate of the material has a huge impact on the final grain morphology and therefore the material properties of this alloy. If it is cooled slowly, as the β phase transforms to α phase, the α phase has time to grow the grains together and it is left as a bimodal equiaxed microstructure.

On the other hand, if it is cooled too fast, it can be left with several other structures. For example, the electron beam melted sample shows that because it was cooled fast at higher temperatures, it was left with acicular grain structure that includes several smaller α phase lamellae since they did not have time to grow together as the melt pool was freezing. As the α freezes, the β is forced into the boundaries between the lamellae.

In some instances, such as the selective laser melted sample, the α phase is cooled so fast that the material is left with a Widmanstatten or a basket weave structure. This is because the α phase is freezing so rapidly, it is competing with other α phases for space. At the same time, the β phase is cooled so rapidly that it transforms completely to martensite.

2.2.2 Wrought (Mill-Annealed)

The mill-annealed sample that was used in this experiment was analyzed under an optical microscope after etching to view the microstructure. In the images shown in Figure 10 and Figure 11, the β crystals (dark colored) are clearly visible in the α matrix

(light color) as well as the α/β colonies. The average grain size was measured using imagine software ImageJ as well as the area percent of α phase. There is also a generated histogram to show the composition of grain sizes throughout the matrix.

Table 3: Grain morphology of mill-annealed Ti-6Al-4V.

Grain Morphology	
Manufacture Process	Mill-Annealed
Grain Structure	Equiaxed Bimodal
Percent α	46%
Average α Grain Size	6.3μm

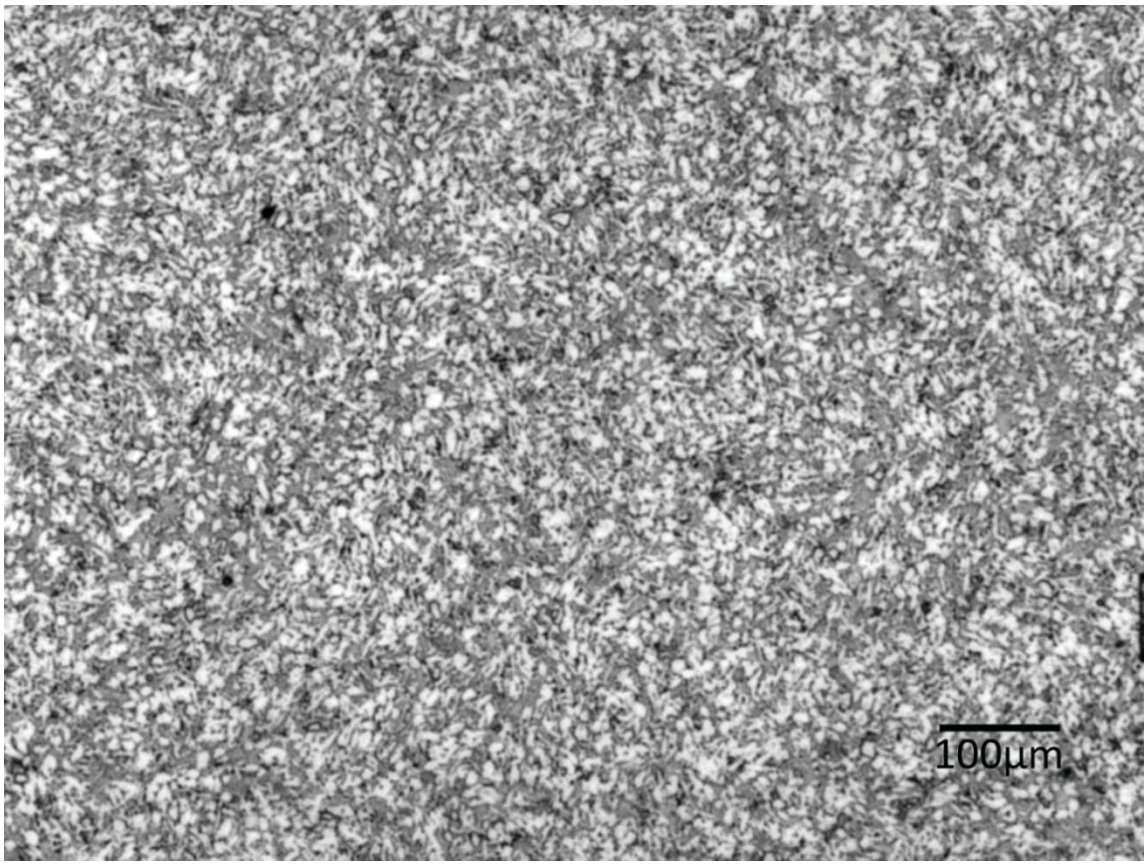

Figure 10: Micrograph showing the bimodal grain structure of the mill-annealed titanium sample surface.

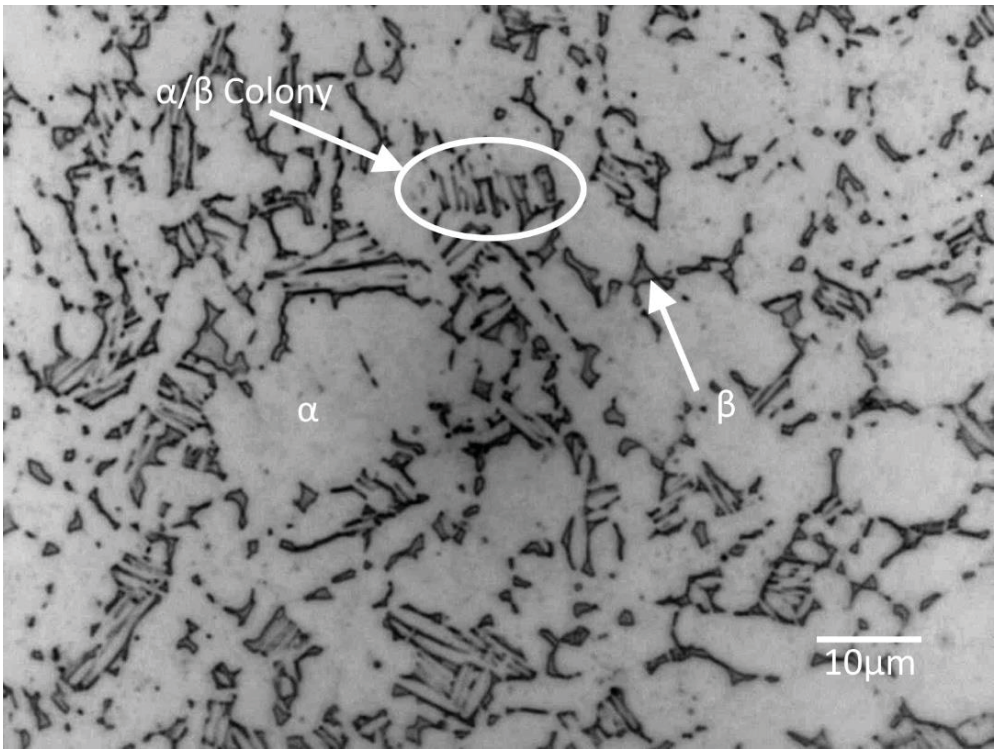

Figure 11: Micrograph showing the bimodal grain structure of the mill-annealed titanium sample surface.

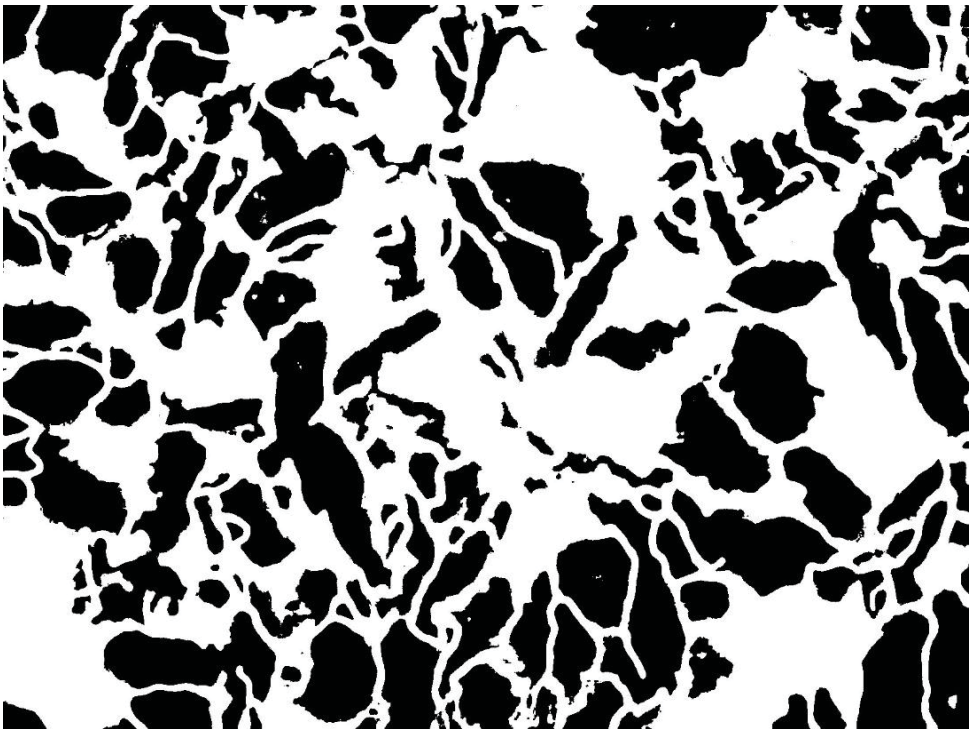

Figure 12: Micrograph modified by ImageJ to find grain size and percent of α phase.

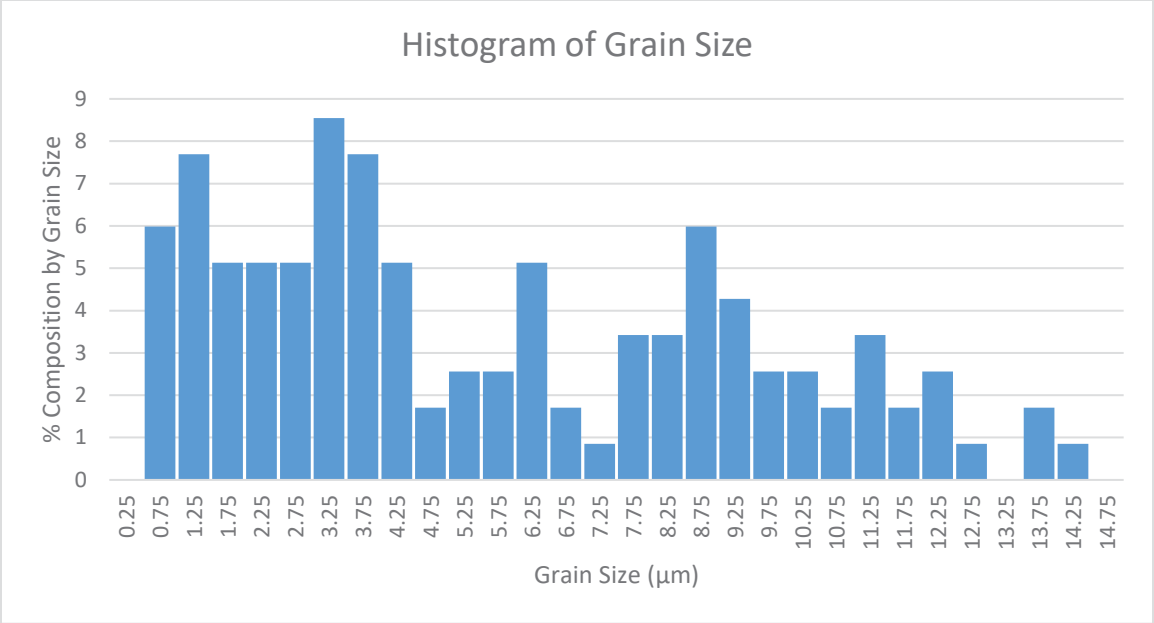

Figure 13: Histogram of grain area of mill-annealed sample surface.

2.2.3 Electron Beam Melted

Next, the electron beam melted samples were inspected under the optical microscope after etching. In Figure 15, the acicular grain structure is visible. The β phase that is between each of the lamellae have been darkened by Kroll's reagent. Again, the grain sizes are measured as well as the percent of α. The α/β fraction is higher, however, the grain size is significantly smaller.

Table 4: Measured grain morphology of electron beam melted sample. Calculated by ImageJ software.

Grain Morphology	
Manufacture Process	Electron Beam Melted
Grain Structure	Acicular
Percent α	74%
Average α Grain Size	1.8µm

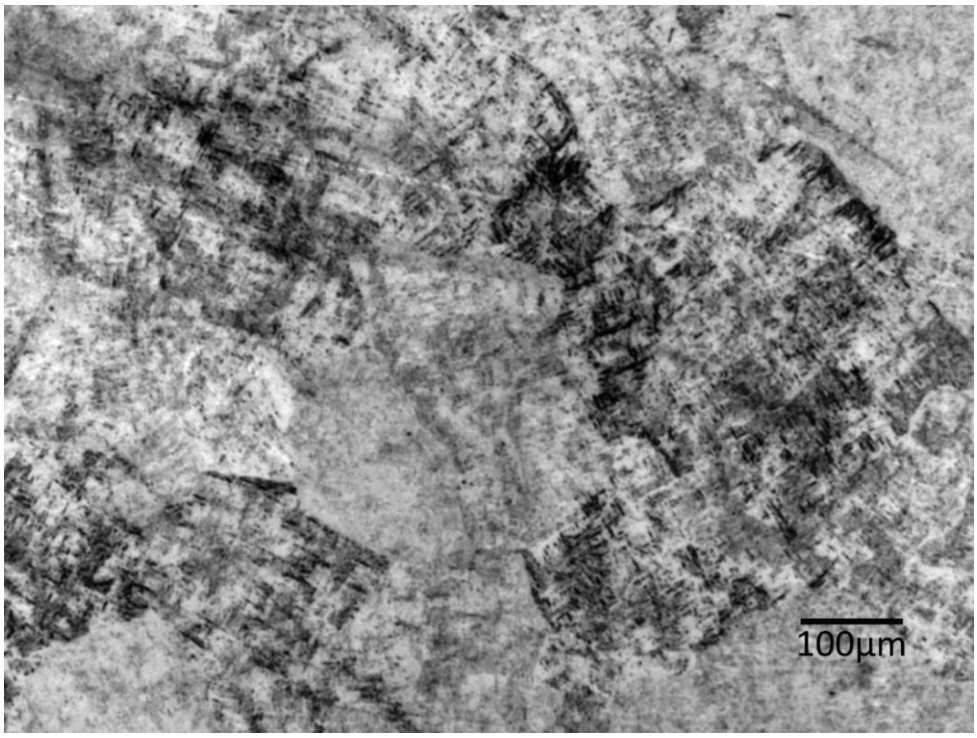

Figure 14: Micrograph of EBM sample after it was etched showing much smaller grain size than mill-annealed.

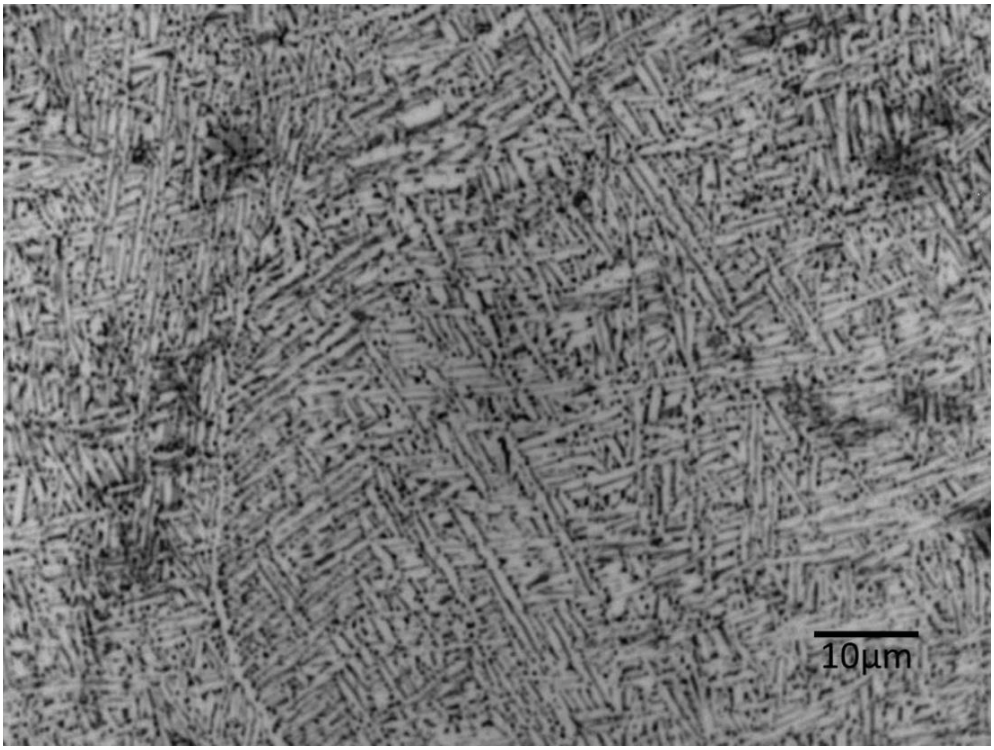

Figure 15: Micrograph of EBM after etching showing acicular grain structure.

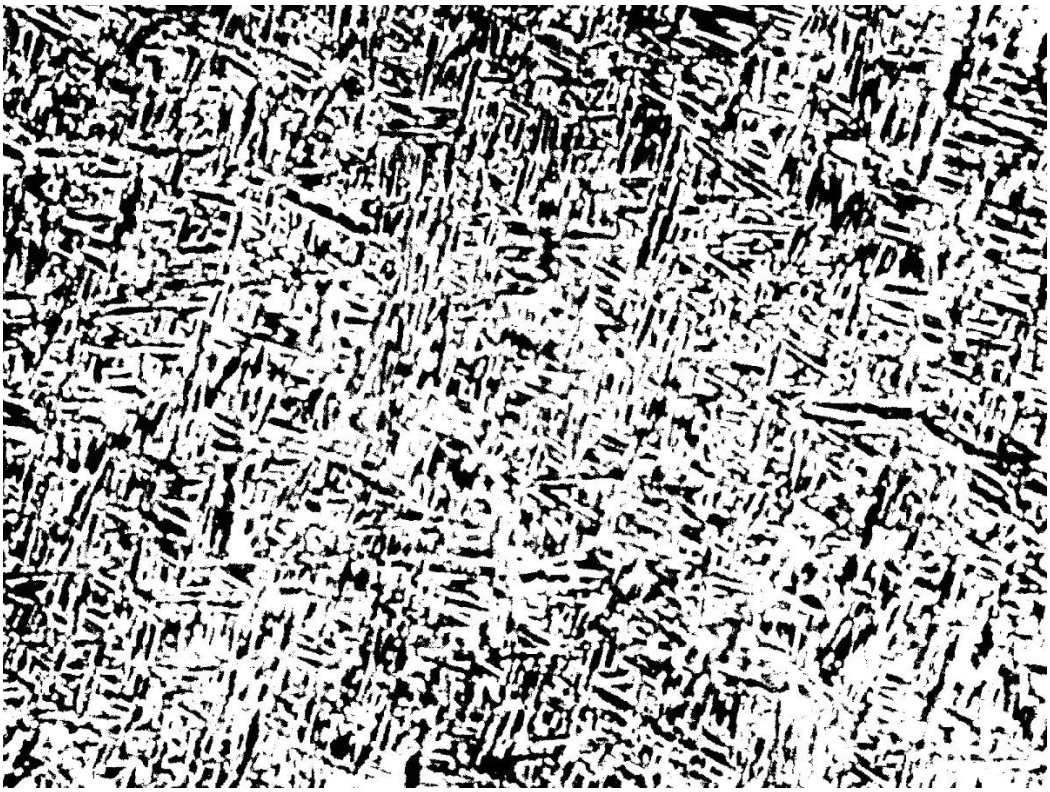

Figure 16: Image used by the software ImageJ to process grain sizes. Note that with such fine grain structure it is extremely difficult to accurately measure grain sizes.

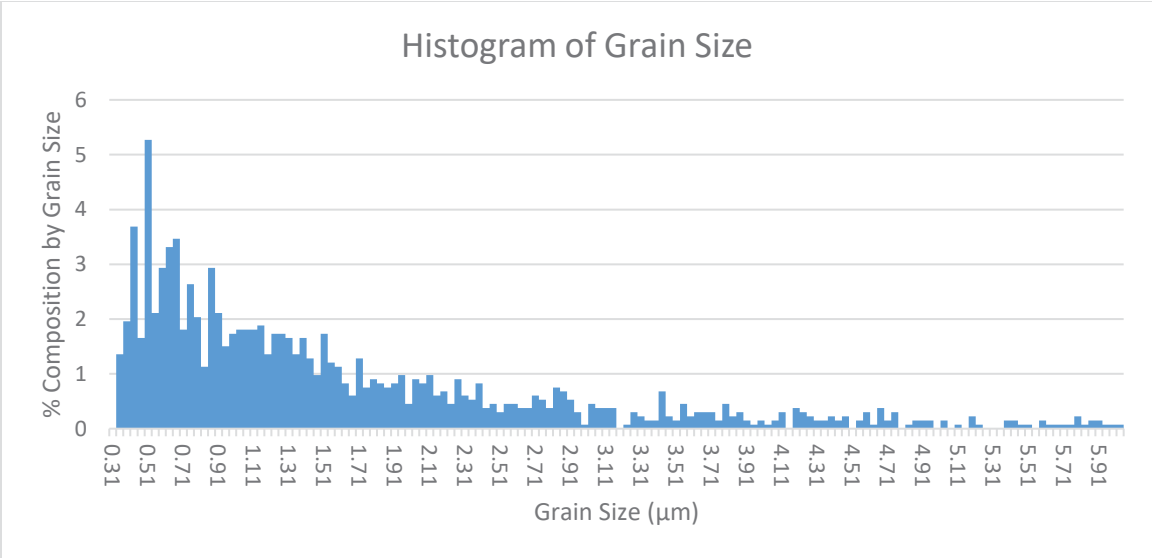

Figure 17: Histogram of the grain area of the EBM surface.

2.2.4 Selective Laser Melted

Similar to the electron beam melted micrographs, after etching the selective laser melted sample with Kroll's reagent, image analysis shows smaller grain size as well. However, there is now a clear Widmanstatten pattern weaving the alloy was cooled very rapidly creating interwoven α phase lamellae that interfere with one another.

Table 5: Measured grain morphology of selective laser melted sample. Calculated by ImageJ software.

Grain Morphology	
Manufacture Process	Selective Laser Melted
Grain Structure	Widmanstatten
Percent α	58%
Average Grain Size	1.6μm

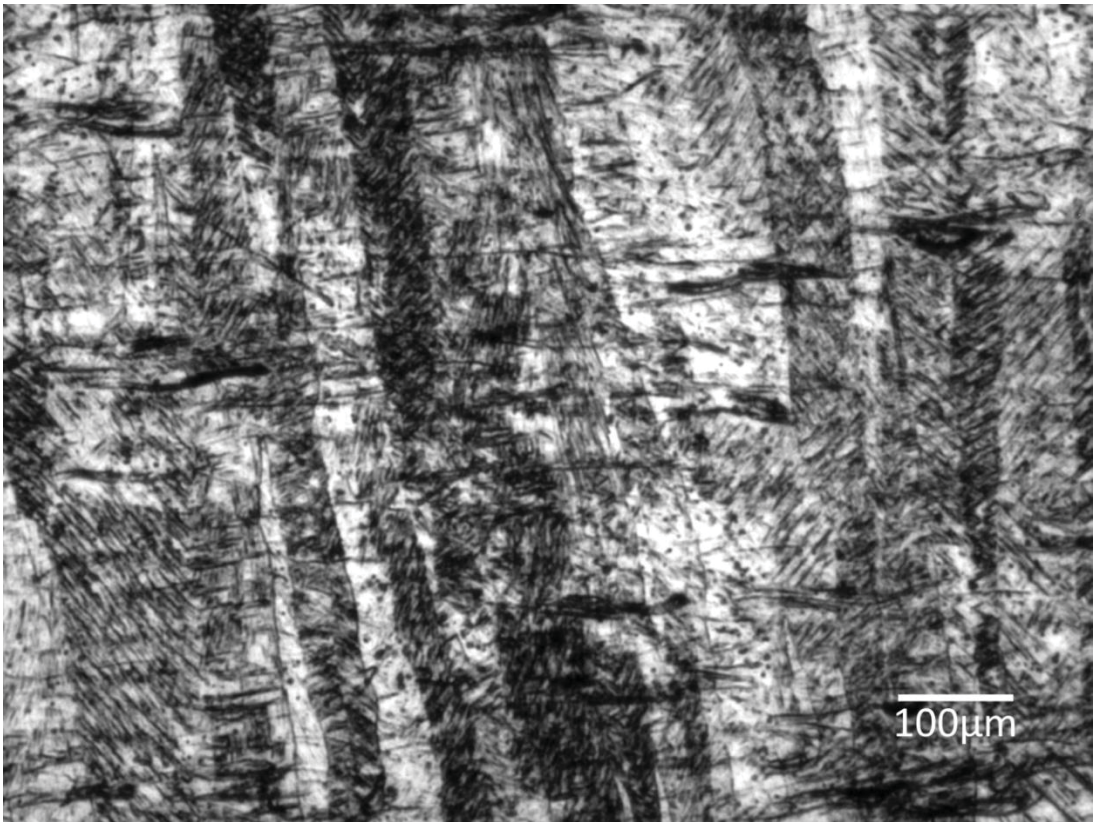

Figure 18: Micrograph of the selective laser melted sample.

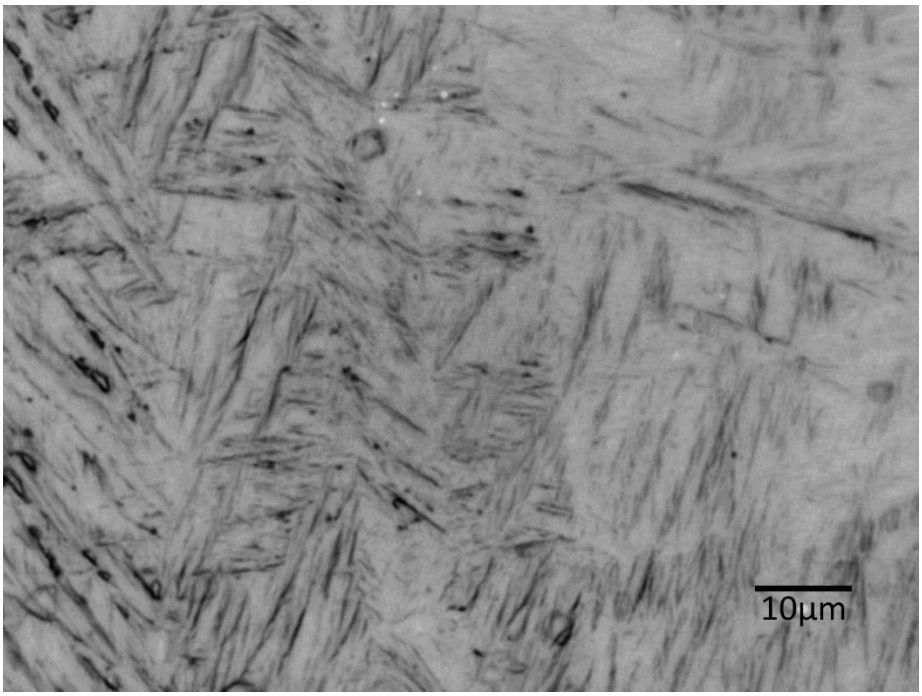

Figure 19: Micrograph of the selective laser melted sample showing Widmanstatten structure.

Figure 20: Image used by the software ImageJ to process grain sizes.

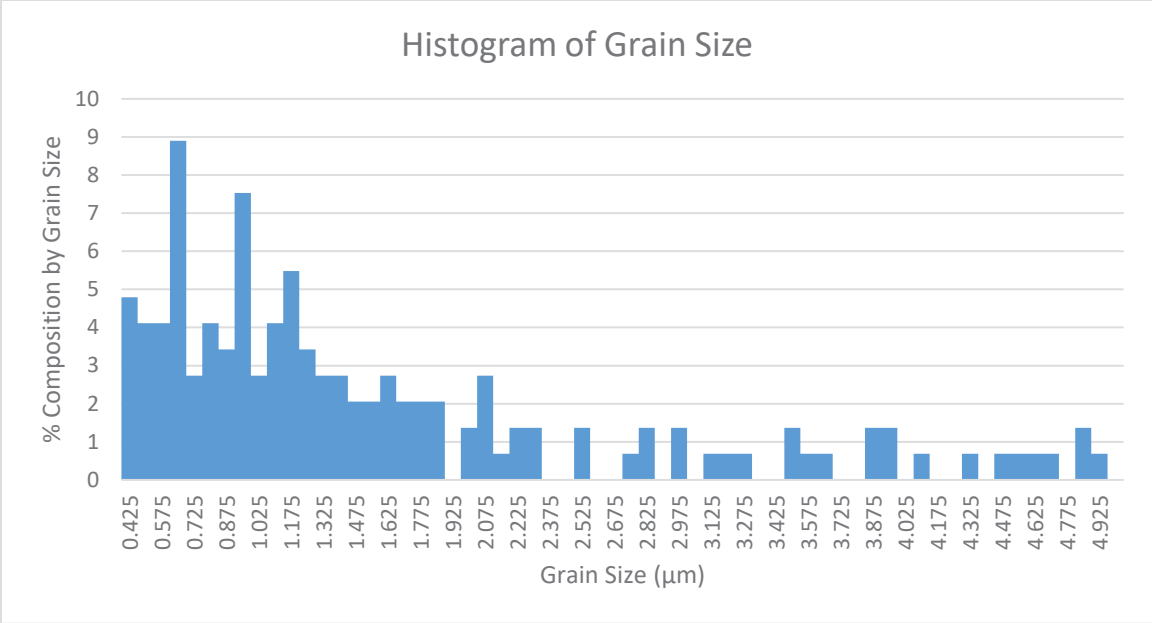

Figure 21: Histogram of the grain area of the SLM surface.

2.3 Nanoindentation based characteristics

2.3.1 Berkovich Indenter Calibration

Before beginning any indentation tests with the nanoindenter, the Berkovich indenter had to be inspected and calibrated. First, it was placed underneath the optical microscope to visually inspect for flaws in the tips such as jagged edges or rounded sides. Once that was complete, it was calibrated using a sample of fused silica with known hardness and the calibration function on the machine. Calibrating the tip involved performing several indentations at several peak forces in different locations to cover several ranges of depths. Using the load and the depth sensor in the machine, it calculated the real area function of the indenter tip which was now a seventh-degree polynomial.

$$A_{corrected} = 24.49h^2 - 29174h + 5445531h^{\frac{1}{2}} - 123460508h^{\frac{1}{4}} + 738450724h^{\frac{1}{8}} - 1441924856h^{\frac{1}{16}} + 821714956h^{\frac{1}{32}} \qquad \text{Eq. (11)}$$

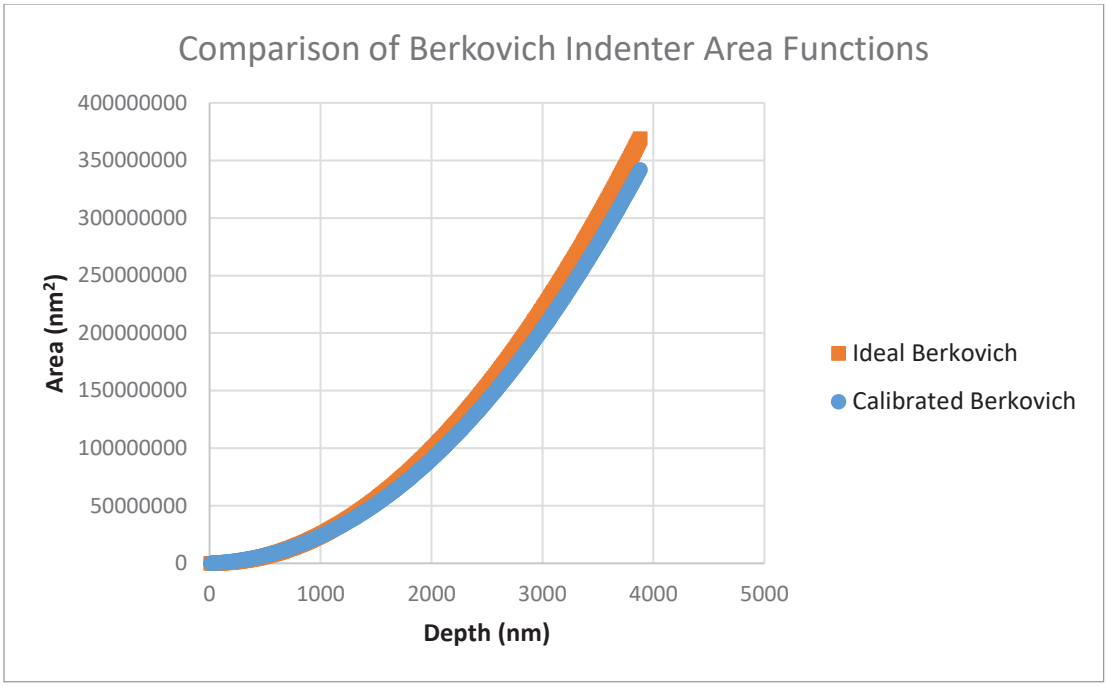

Figure 22: Comparison of the calibrated Berkovich indenter against the ideal shape.

2.3.2 Single Constant Rate of Loading (CRL) Experiment

After analysis of the grain structure was complete and the Berkovich indenter was calibrated, the samples were sonicated with acetone, methanol, and distilled water as before. They were then placed on a Nanovea Nanoindentation machine. They were securely fastened in a vice and positioned under an optical microscope to inspect the surface to be tested. Once a suitable area on the surface with no flaws was found, the samples were then moved to an optical profilometer equipped to the nanoindenter. Using the optical profilometer, the surface flatness was measured and adjusted in both the x and y horizontal directions to ensure the sample was as flat as possible. At the same time, the surface roughness was measured to ensure a smooth surface.

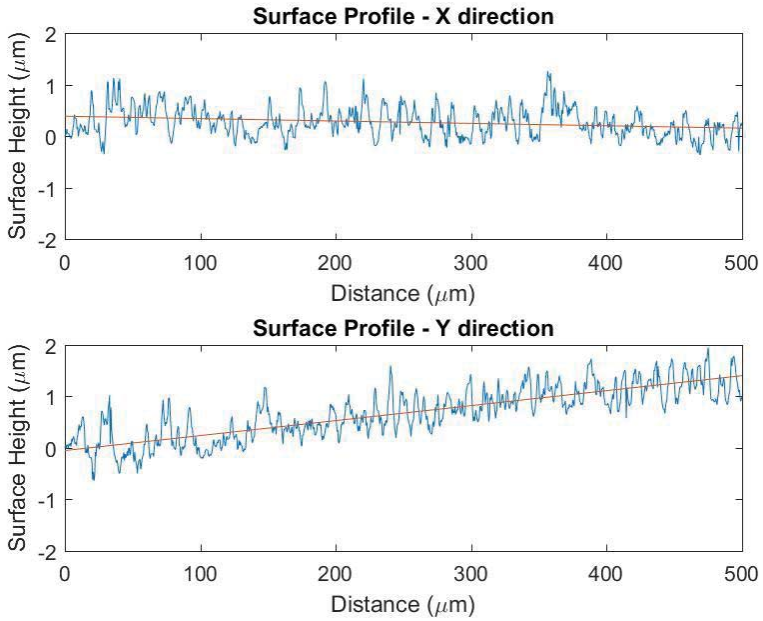

Figure 23: Surface Profile of the area of the mill-annealed surface near where the single indent tests would occur.

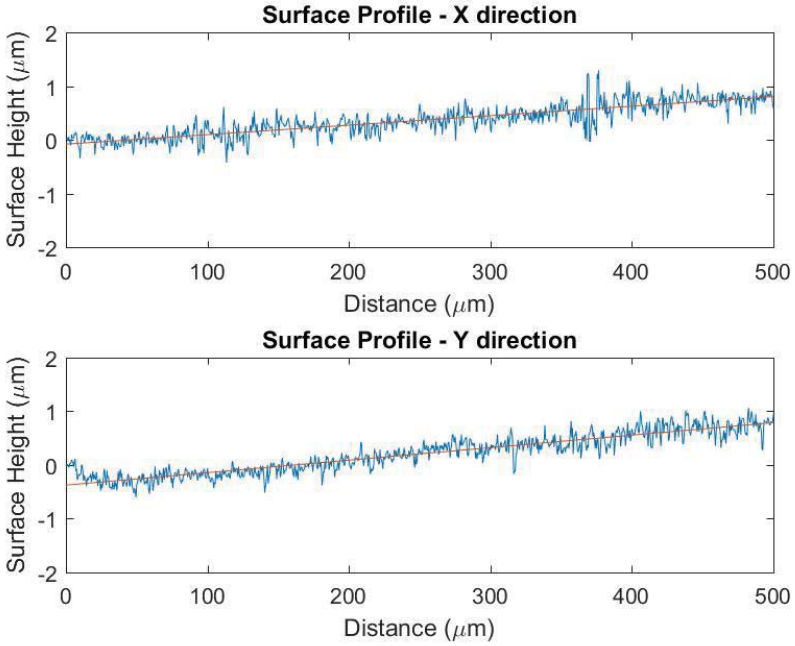

Figure 24: Surface Profile of the area of the EBM surface near where the single indent tests would occur.

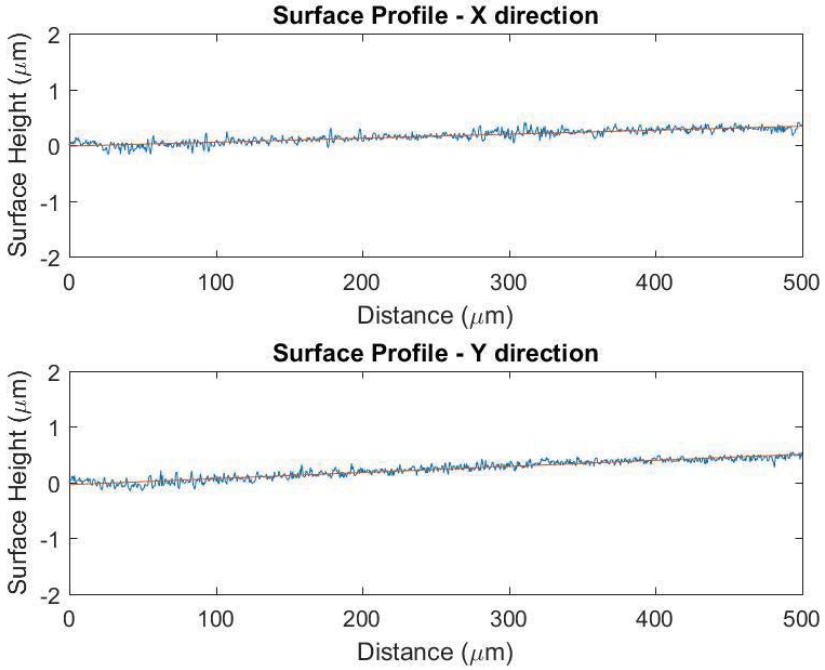

Figure 25: Surface Profile of the area of the SLM surface near where the single indent tests would occur.

Table 6: Surface Profilometry of the samples used for single indentation testing.

Surface Profilometry

	M-A	EBM	SLM
Slope - X	-0.0265	0.1012°	0.0409°
Slope - Y	0.1664°	0.1332°	0.0626°
CLA - X	0.2074µm	0.1099µm	0.0418µm
CLA - Y	0.2187µm	0.0975µm	0.0384µm

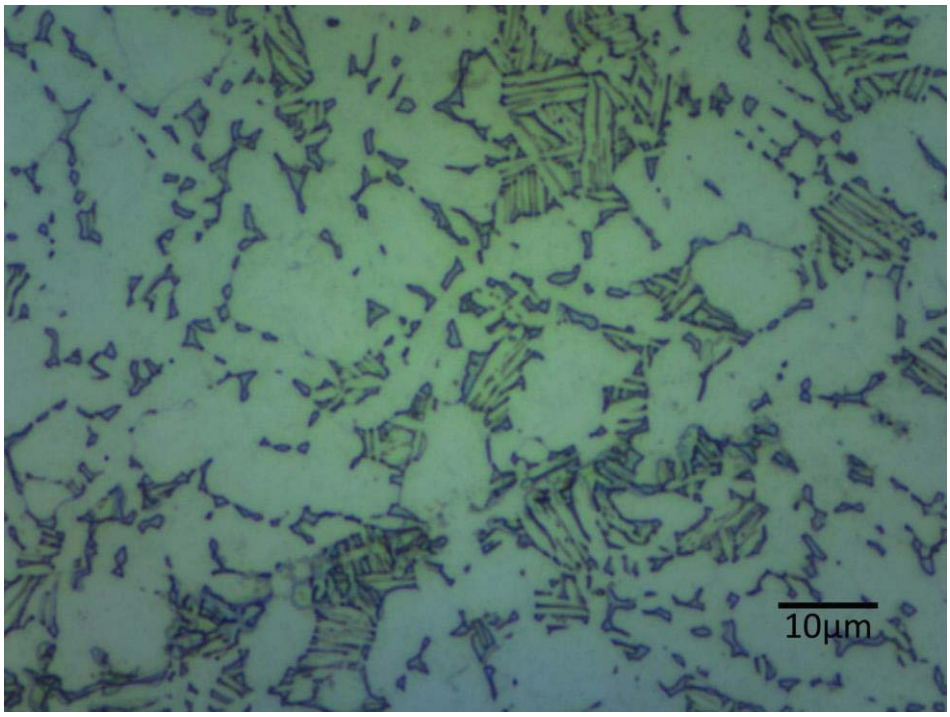

Figure 26: Micrography of the test surface used for single indent tests on mill-annealed sample.

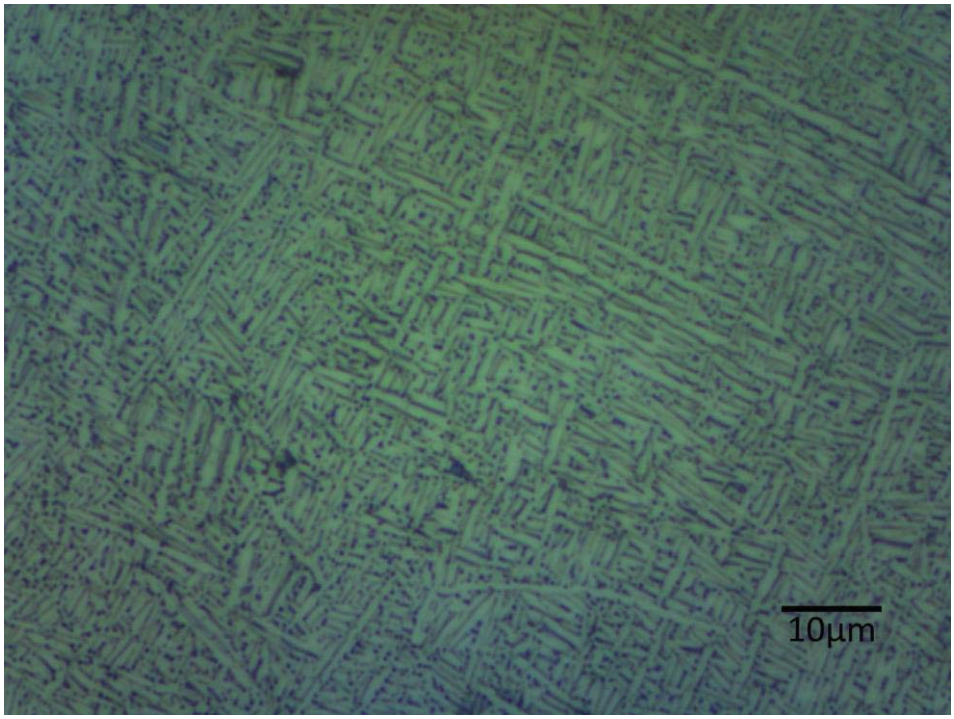

Figure 27: Micrography of the test surface used for single indent tests on EBM sample.

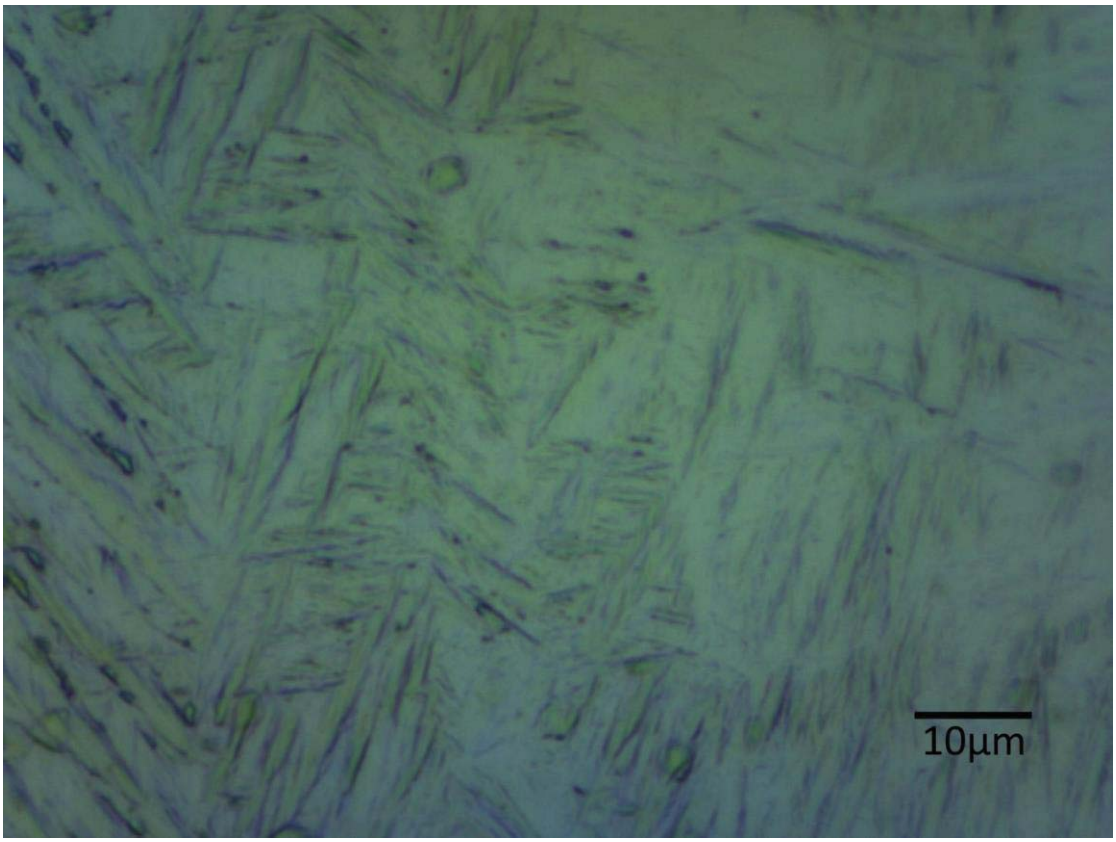

Figure 28: Micrography of the test surface used for single indent tests on SLM sample.

Once the sample has been sufficiently levelled and a proper surface found, the sample was moved underneath a Berkovich indenter to be tested. The Berkovich indenter was slowly brought to contact with the loading surface and then retracted and moved to a different area to avoid corrupted date from the residual indent. The tip was then brought to the surface at a rate of 1µm/min until a contact load of 0.2mN/min was reached. The load was then immediately increased at the specified loading rate. Tests were completed with different loading speeds of 100mN/min, 200mN/min, 400mN/min and 600mN/min. Each different loading speed was done with close proximity to the tests of other speeds in the set. Then the entire test was repeated at a different location to provide multiple sets of data.

Table 7: Testing parameters for single indent load tests.

Testing Parameters				
	Test Set 1	Test Set 2	Test Set 3	Test Set 4
Loading Rate	100mN/min	200mN/min	400mN/min	600mN/min
Unloading Rate	100mN/min	200mN/min	400mN/min	600mN/min
Contact Speed	1μm/min			
Contact Load	0.2mN			
Peak Load	15mN			
Number of Loading Cycles	1			

Table 8: Berkovich Indenter Characteristics

Berkovich Indenter Characteristics	
Modulus of Elasticity	1140
Poisson's Ratio	0.07
Area Function	$24.49h^2 - 29174h + 5445531h^{1/2} - 123460508h^{1/4} + 738450724h^{1/8} - 1441924856h^{1/16} + 821714956h^{1/32}$

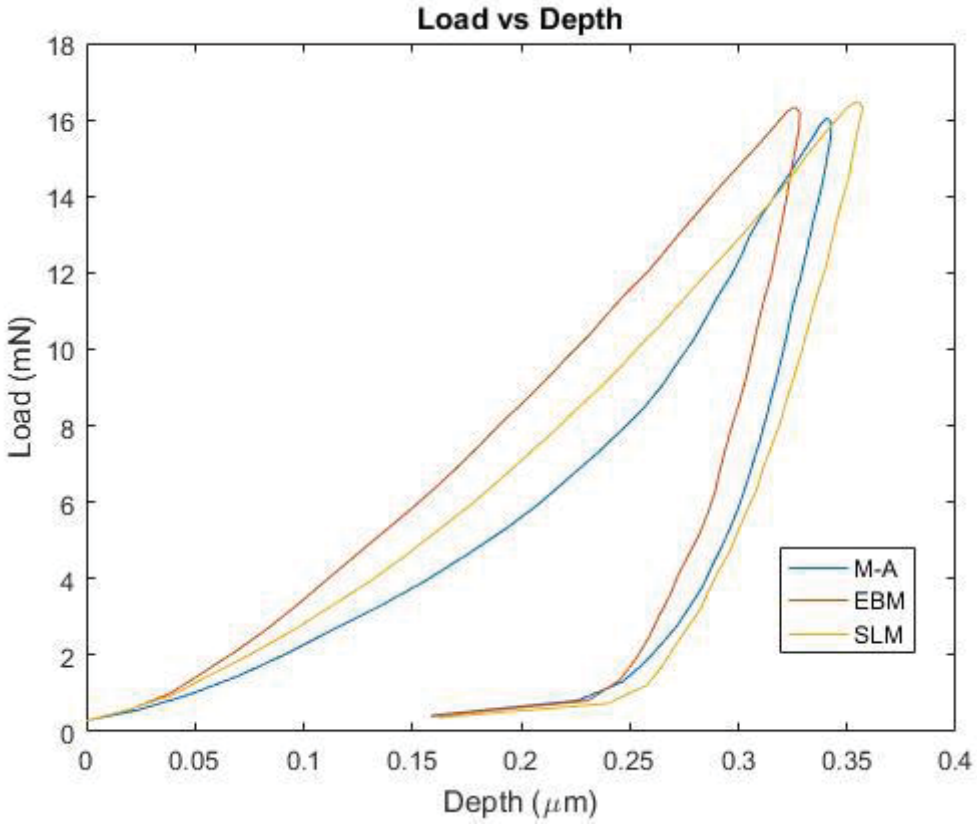

Figure 29: Typical load vs depth graph of a single indent test.

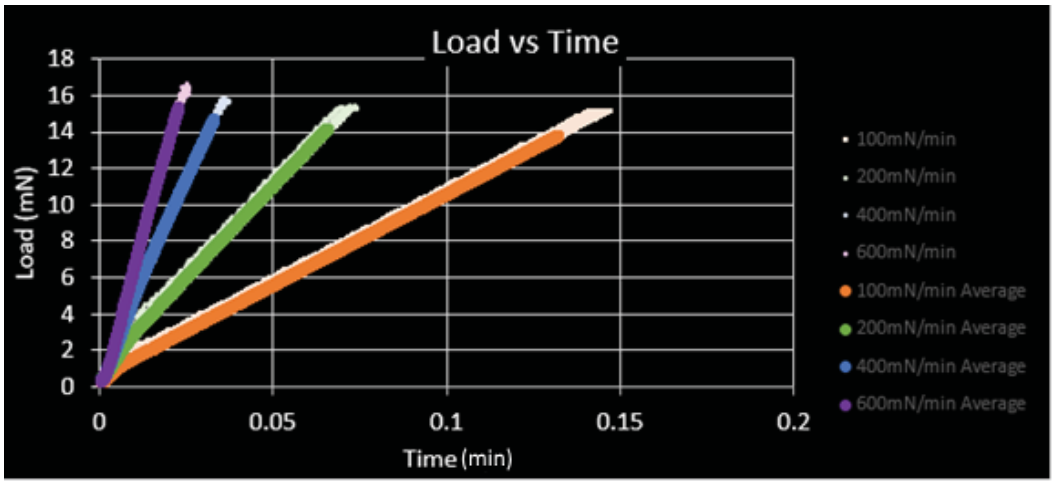

Figure 30: Load vs time graph for the mill-annealed sample.

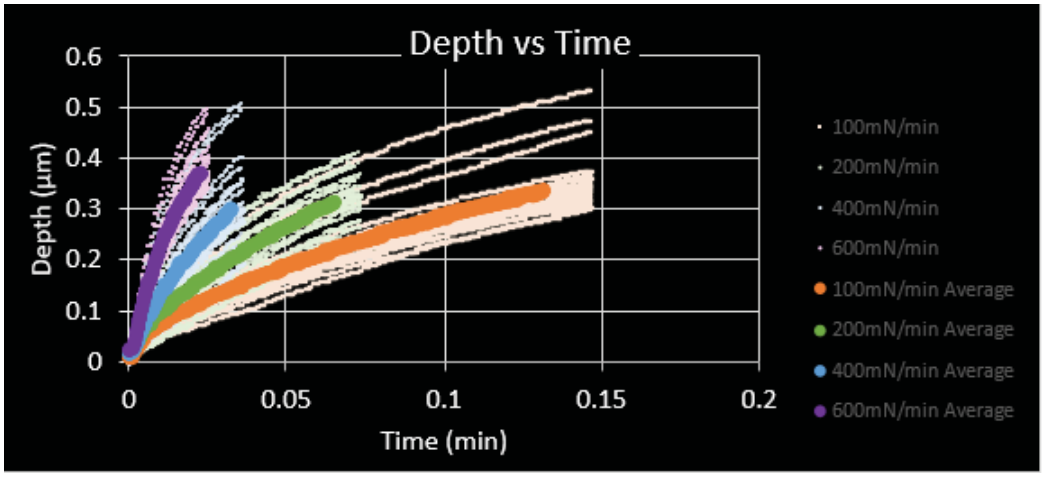

Figure 31: Depth vs time for mill-annealed sample.

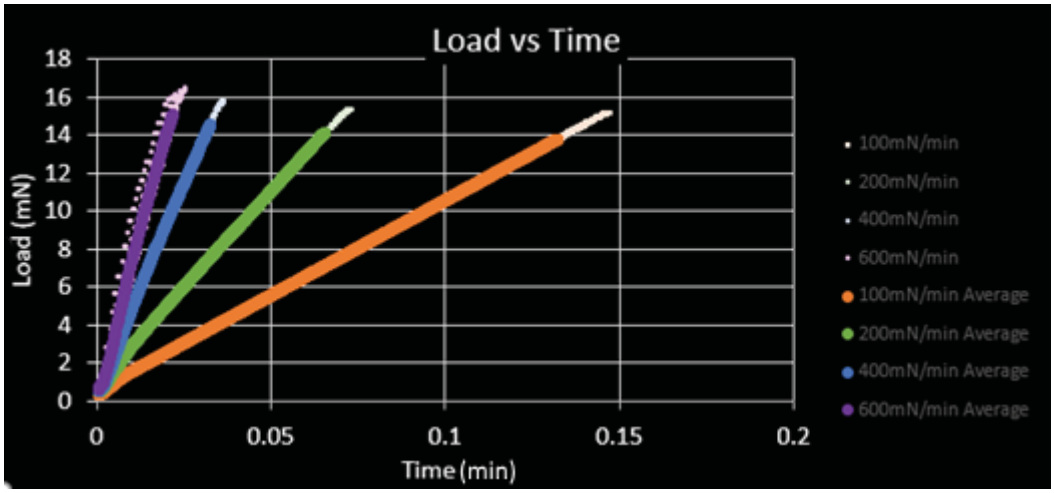

Figure 32: Load vs time graph for the EBM sample.

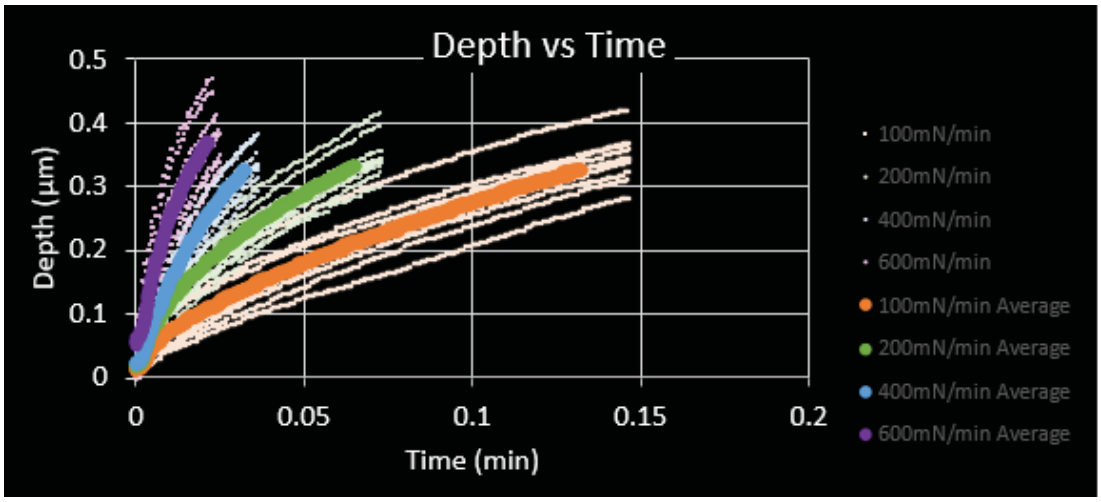

Figure 33: Depth vs time for EBM sample.

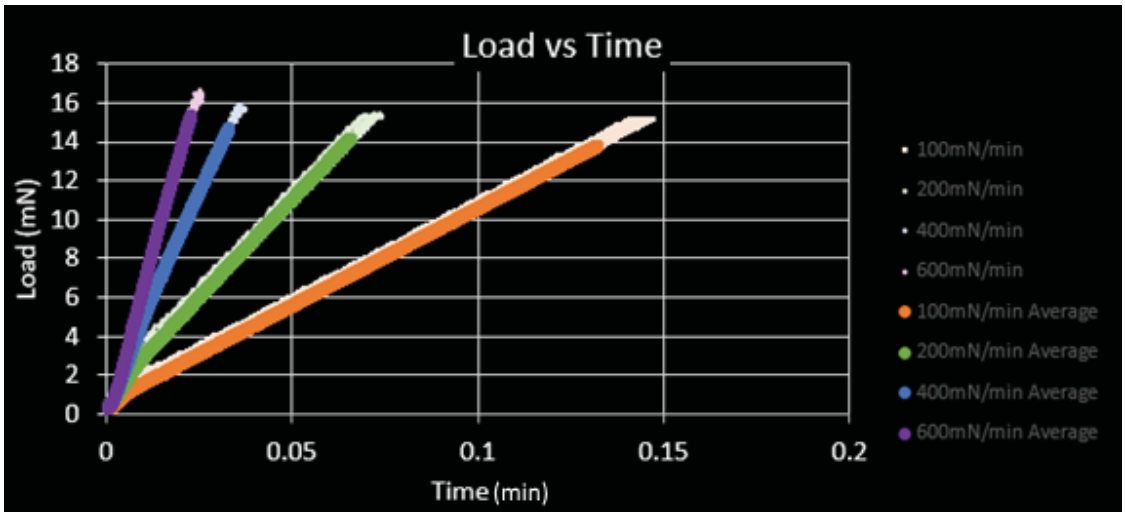

Figure 34:: Load vs time graph for the SLM sample.

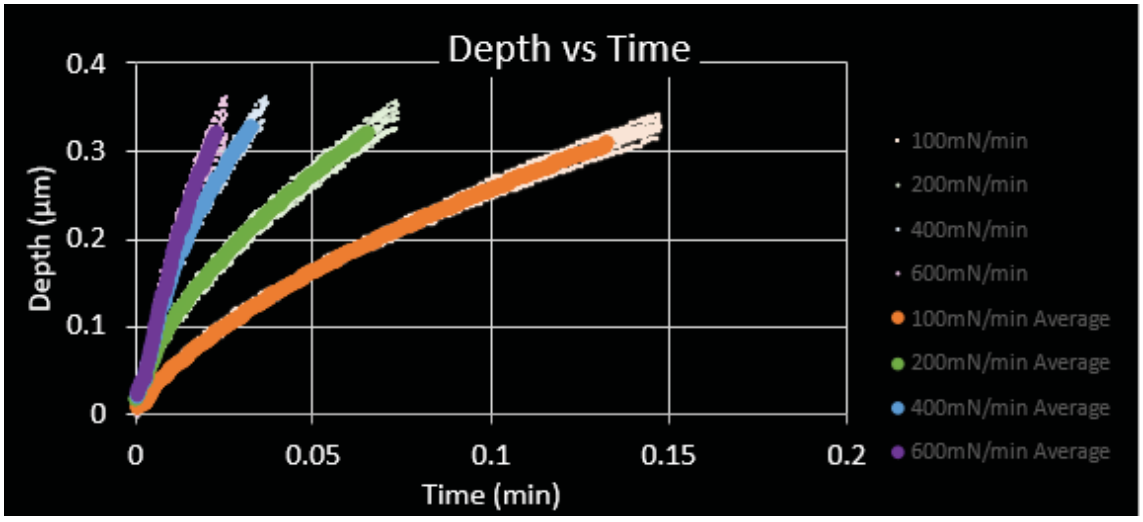

Figure 35: Depth vs time for SLM sample.

The stiffness was calculated using the initial 20% of the unloading curve and the residual stress was calculated using the x-intercept of the slope of the stiffness from the peak load. The reduced modulus of elasticity was then calculated as:

$$E_r = \frac{\frac{\sqrt{\pi}}{2}S}{\sqrt{A_c}} \qquad \text{Eq. (12)}$$

This was converted into modulus of elasticity by:

$$\frac{1}{E} = \frac{1-\nu^2}{E_r} + \frac{1-\nu_i^2}{E_i} \qquad \text{Eq. (13)}$$

$$\nu = 0.342$$

$$\nu_i = 0.2$$

$$E_i = 1150GPa$$

Where ν is Poisson's ratio of the sample, ν_i is the Poisson's ratio of the indenter, and E_i is the modulus of elasticity of the indenter.

In all three samples, there is a significant correlation between elastic modulus and strain rate. As expected, mill-annealed is the most elastic of the samples, followed by EBM and then SLM.

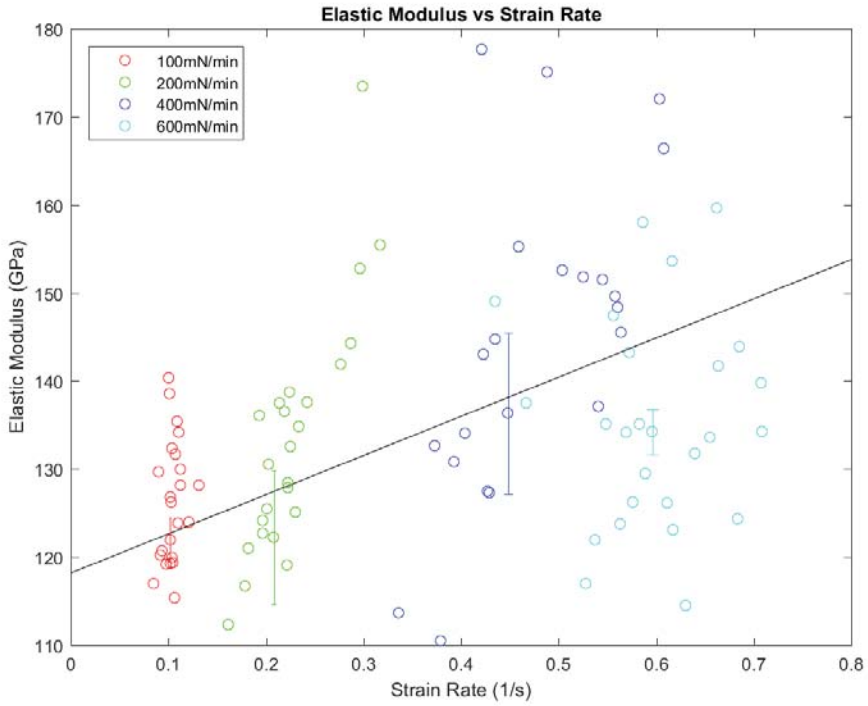

Figure 36: Elastic modulus vs strain rate of the mill-annealed sample.

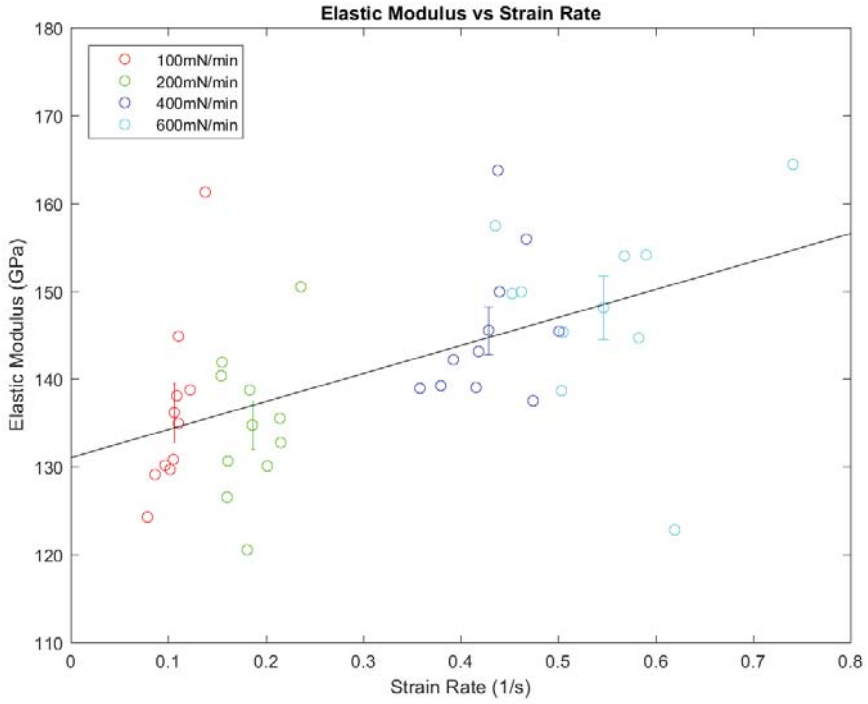

Figure 37: Elastic modulus vs strain rate of the EBM sample.

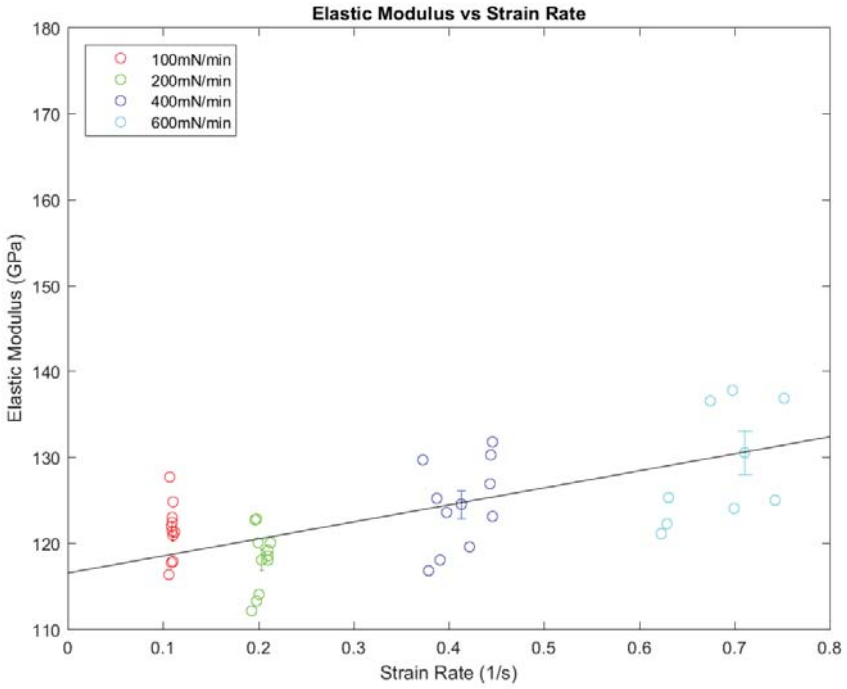

Figure 38: Elastic modulus vs strain rate of the SLM sample.

Table 9: Average elastic modulus for each sample.

Modulus of Elasticity (GPA)		
Mill-Annealed	EBM	SLM
133.86	141.15	123.65

Although strain rate on a macroscale is calculated using flow stress, on a local level it can be calculated using hardness. In this paper, since the results will be used in comparison with each other and for simpler calculations, Marten's hardness is used. Marten's hardness is defined by the peak load divided by the area at that load. To obtain area, the calibrated Berkovich area function that was mentioned earlier must be used along with the maximum depth.

$$HM = \frac{P_{max}}{A_{max}} \quad \text{Eq. (14)}$$

Strain rate is calculated by the change in strain divided by the chain in time. In the case of this paper, it is a close approximation to say the strain rate is:

$$\dot{\epsilon} = \frac{\dot{h}}{h} = \frac{d}{dt}\ln(h) \qquad \text{Eq. (15)}$$

When a hardness vs strain rate graph is created, the resulting slope of a line going through a log/log scale is the strain rate sensitivity. It is calculated as:

$$m = \frac{d}{dt}\frac{\ln(H)}{\ln(\dot{\epsilon})} \quad \text{Eq. (16)}$$

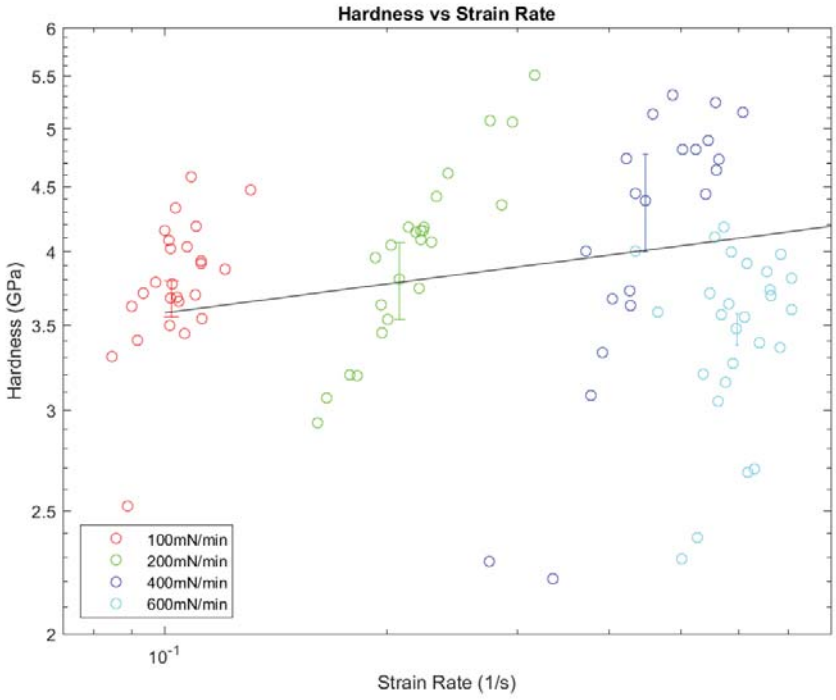

Figure 39: Hardness vs strain rate graph of mill-annealed sample.

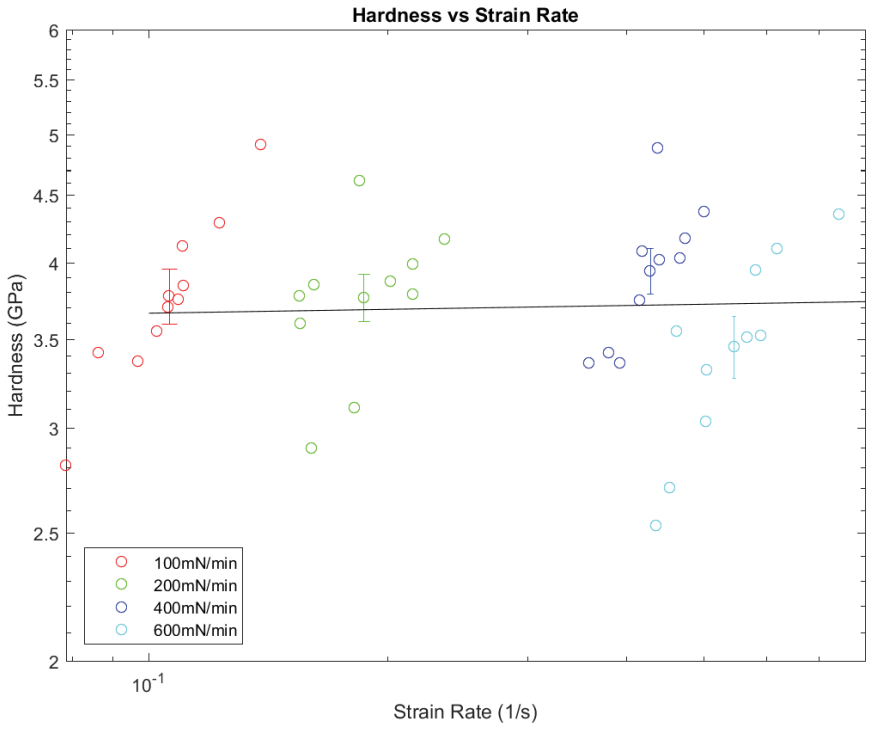

Figure 40: Hardness vs strain rate graph of EBM sample.

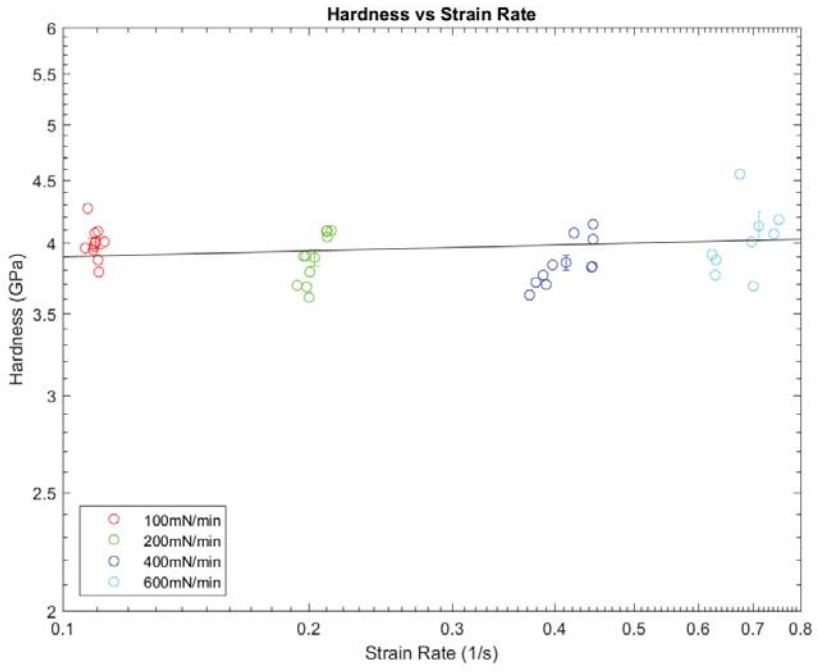

Figure 41: Hardness vs strain rate graph of SLM sample.

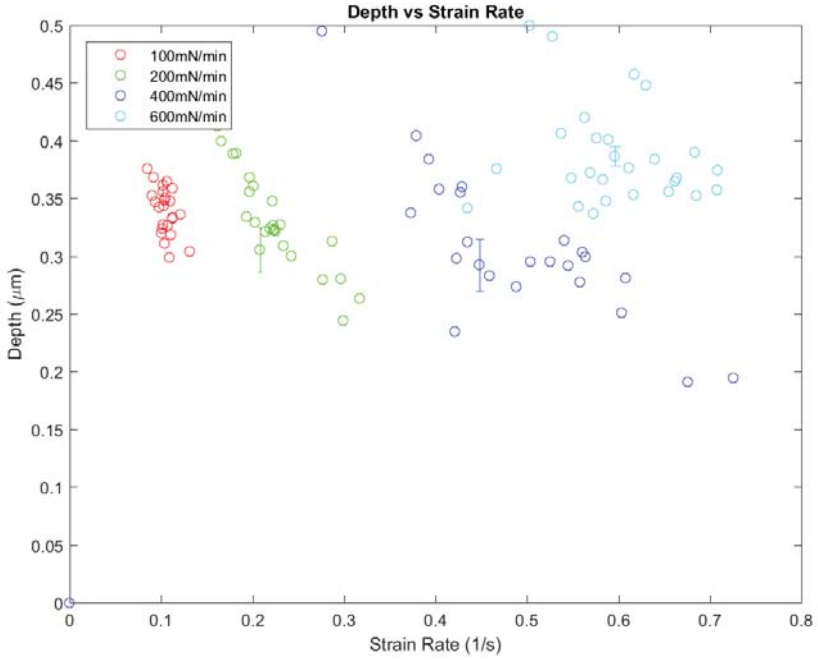

Figure 42: Depth vs strain rate graph of mill-annealed sample.

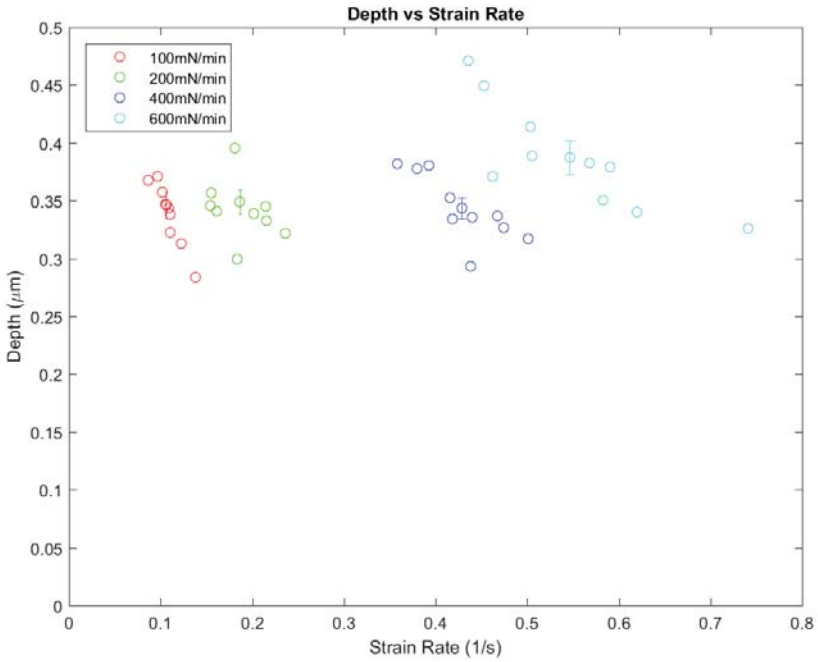

Figure 43: Depth vs strain rate graph of EBM sample.

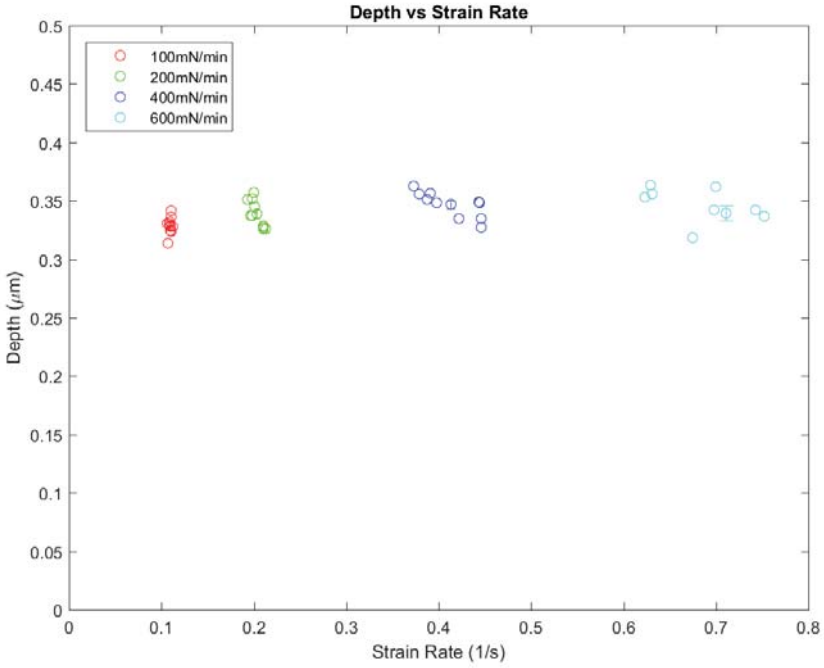

Figure 44: Depth vs strain rate graph of SLM sample.

The data shows that all three samples are subject to a positive strain rate sensitivity. From the data, the conventional mill-annealed surface has a much higher strain rate than the other two surfaces, which may indicate that larger grain size in Ti-6Al-4V induces a higher strain rate sensitivity.

Table 10: SRS of the samples tested.

Strain Rate Sensitivity		
M-A	EBM	SLM
0.0754	0.0097	0.0159

As indicated by others, strain rate sensitivity can be dependent on grain size (32) but it can also be dependent on other microstructure features including the α/β fraction (27). A dependency on grain size may be also related to the crystalline structure of the

material (33). Since the samples here are different grain structures, it makes sense that their respective sensitivities are different.

2.3.3 Multipeak Loaded Constant Rate of Loading Indentation Experiments

In order to help prove the strain rate sensitivity of these materials, further tests were conducted using a similar method of constant rate of loading. However, instead of a single loading and unloading curve with a peak load of 15mN, the data was instead loaded to four different peaks on the same spot. The peaks were 4mN, 7mN, 10mN, 15mN. The indenter was unloaded 90% from each peak and then reloaded. All four peaks were loaded and unloaded at the same constant loading rate. After the four peaks, the indenter was moved to a nearby area and the test was rerun with a different loading rate. Before a new set of tests was run on the samples, the surfaces were again checked and adjusted for levelness.

Table 11: Surface profilometry of samples used for multi-load indentation testing.

Surface Profilometry

	M-A	EBM	SLM
Slope - X	0.1199°	-0.0660°	0.0556°
Slope - Y	0.0706°	0.1827°	0.2746°
CLA - X	0.1589µm	0.0969µm	0.1023µm
CLA - Y	0.1468µm	0.1222µm	0.0626µm

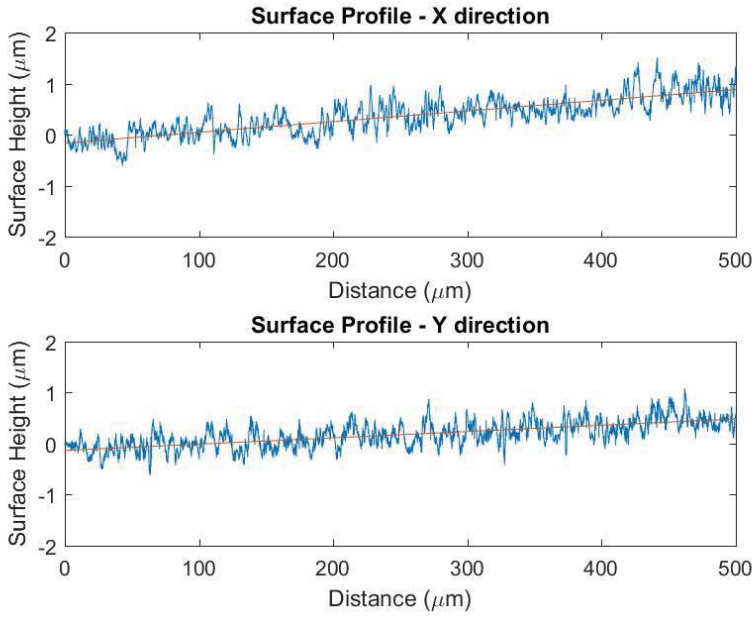

Figure 45: Surface Profile of the area of the mill-annealed surface near where the multi-load indentation tests would occur.

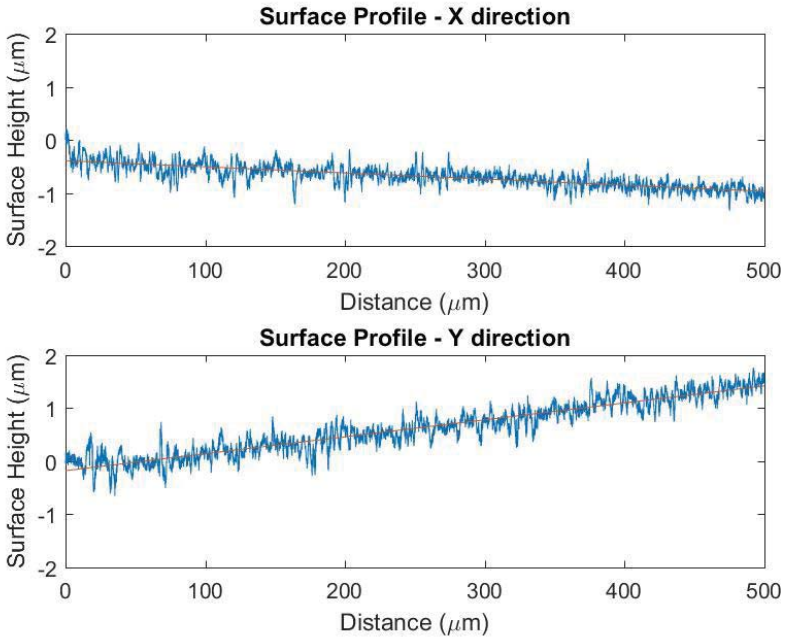

Figure 46: Surface Profile of the area of the EBM surface near where the multi-load indentation tests would occur.

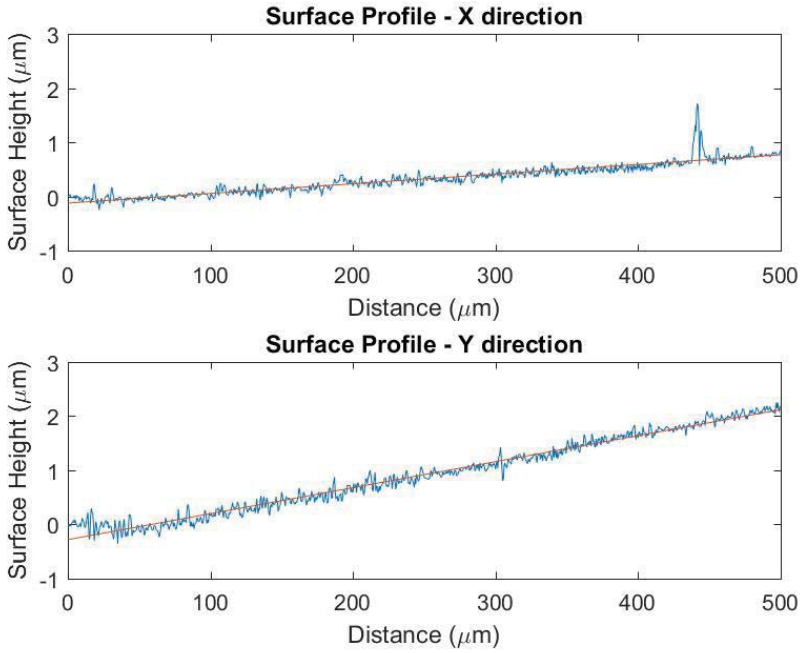

Figure 47: Surface Profile of the area of the SLM surface near where the multi-load indentation tests would occur.

Once the surface was sufficiently level, the surface was moved underneath the indenter tip. As before, the indenter tip was slowly put into contact with the surface and then retracted to move the surface to an unaltered area. The parameters were similar to the previous test aside from the addition of multiple peak loads with a cyclic indentation method.

Table 12: Testing parameters for the multiload indentation tests.

Testing Parameters

	Test Set 1	Test Set 2	Test Set 3	Test Set 4
Contact Speed	1µm/min	1µm/min	1µm/min	1µm/min
Contact Load	0.2mN	0.2mN	0.2mN	0.2mN
Loading Rate	100mN/min	200mN/min	400mN/min	600mN/min
Unloading Rate	100mN/min	200mN/min	400mN/min	600mN/min
Peak Load	15mN	15mN	15mN	15mN
Number of Loading Cycles	4	4	4	4

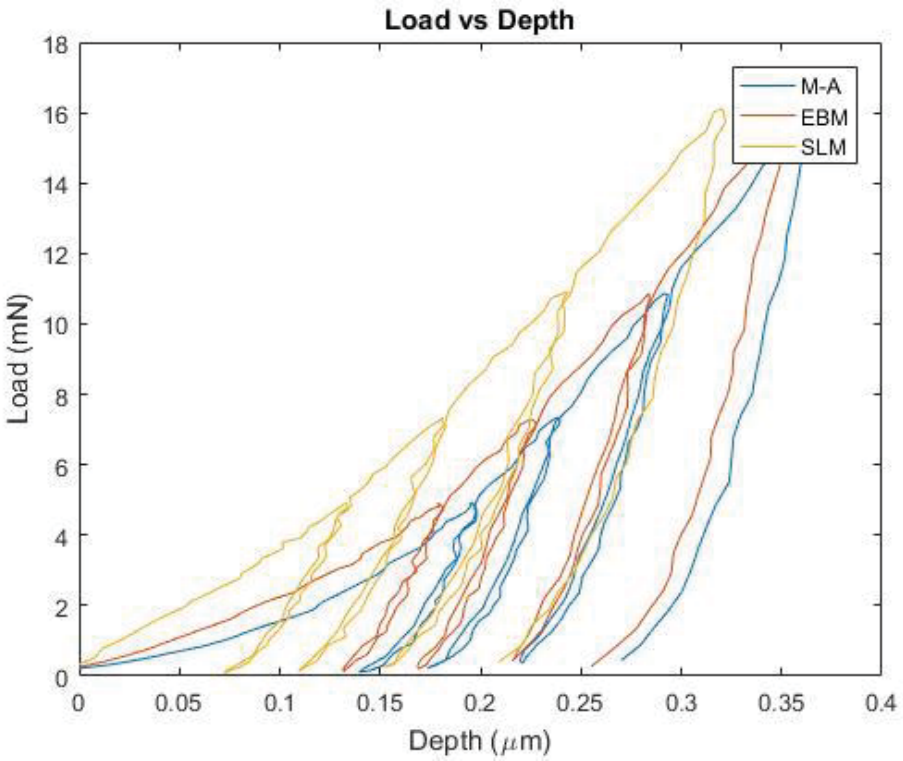

Figure 48: Typical load vs depth chart for a multi-load indentation test.

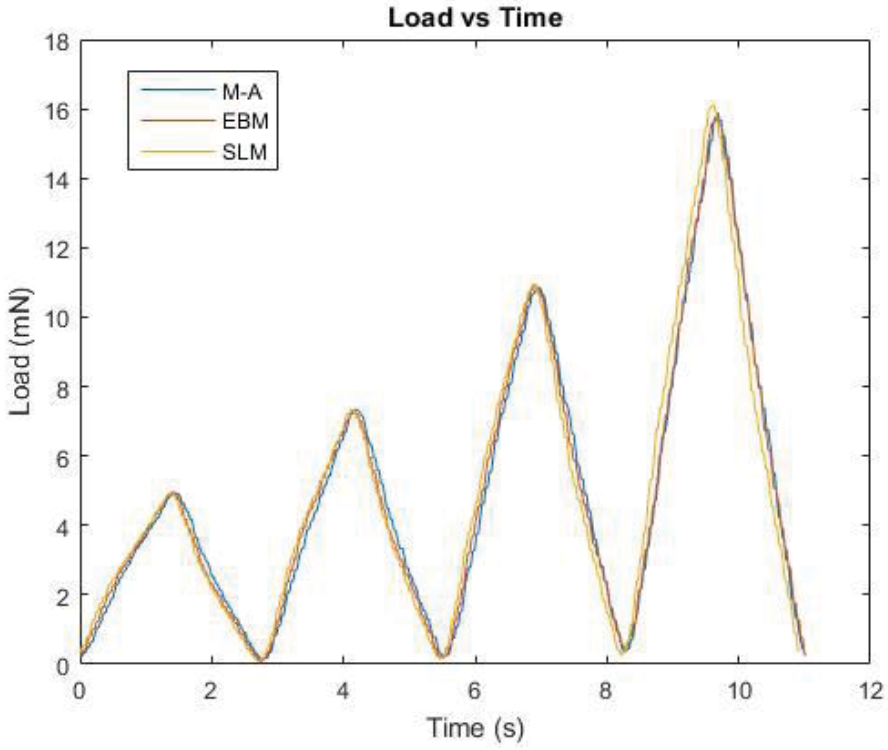

Figure 49: Typical load vs time chart for a multi-load indentation test.

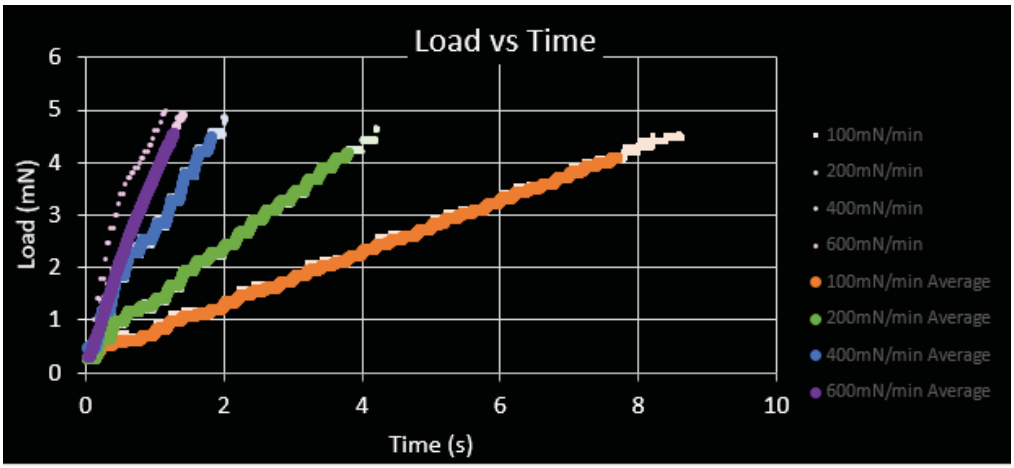

Figure 50: Load vs time chart for the first peak of the mill-annealed sample.

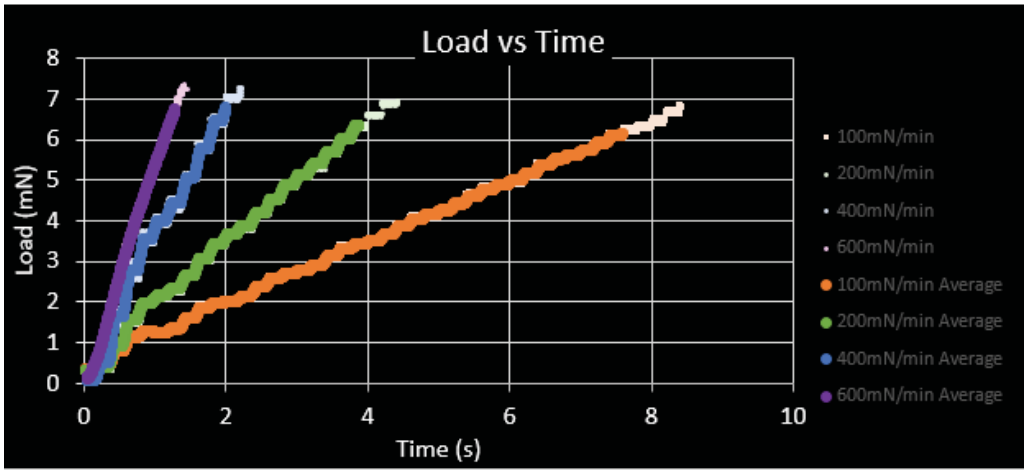

Figure 51: Load vs time chart for the second peak of the mill-annealed sample.

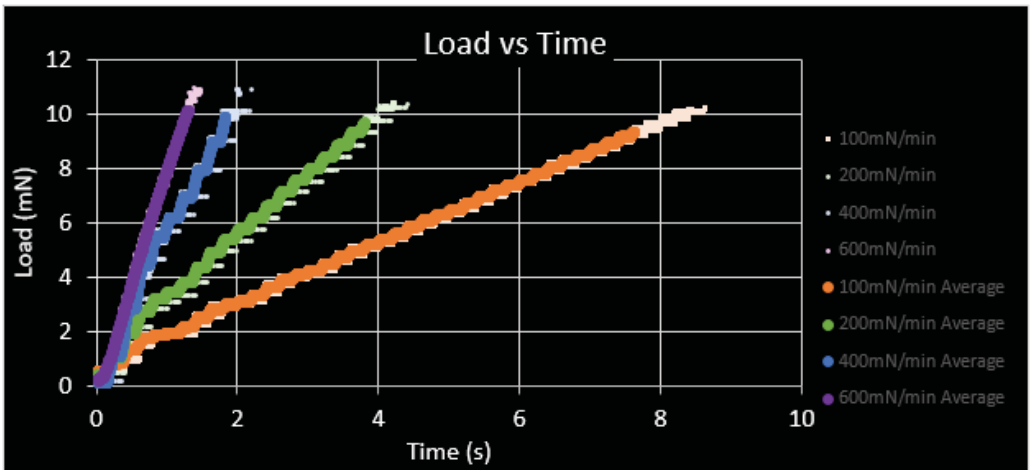

Figure 52: Load vs time chart for the third peak of the mill-annealed sample.

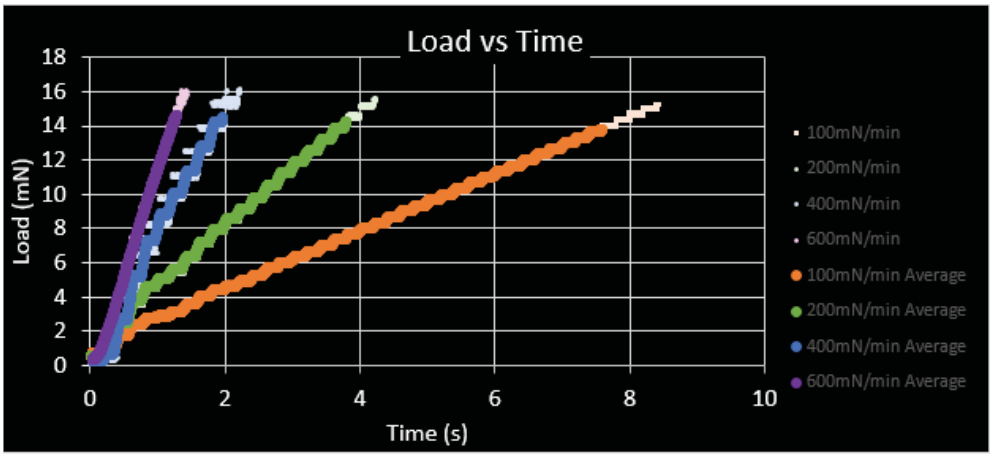

Figure 53: Load vs time chart for the fourth peak of the mill-annealed sample.

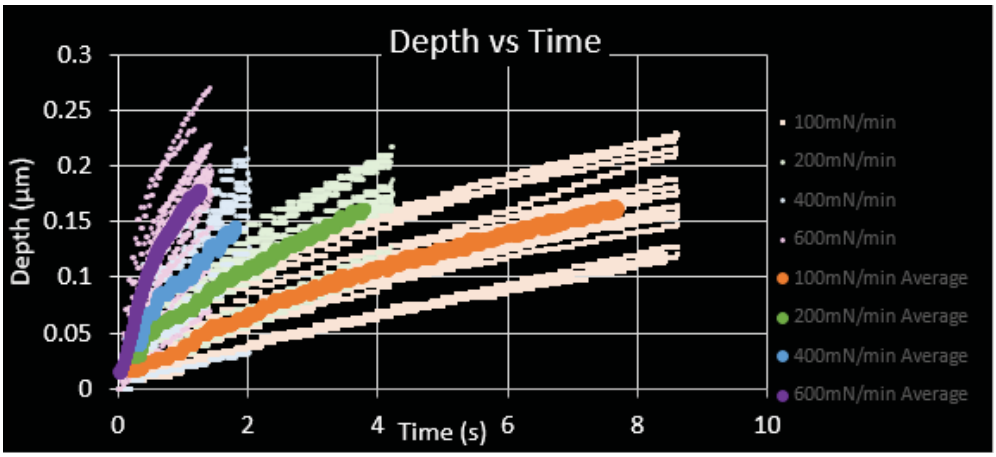

Figure 54: Depth vs time chart for the first peak of the mill-annealed sample.

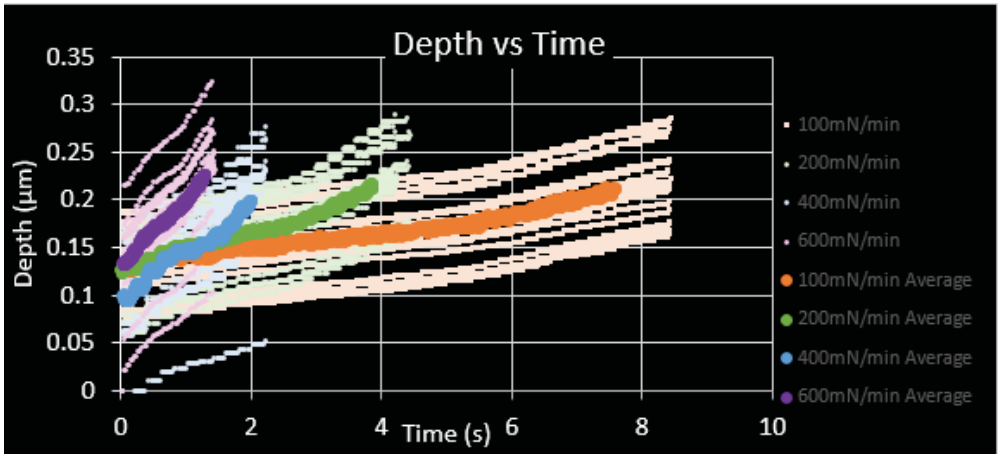

Figure 55: Depth vs time chart for the second peak of the mill-annealed sample.

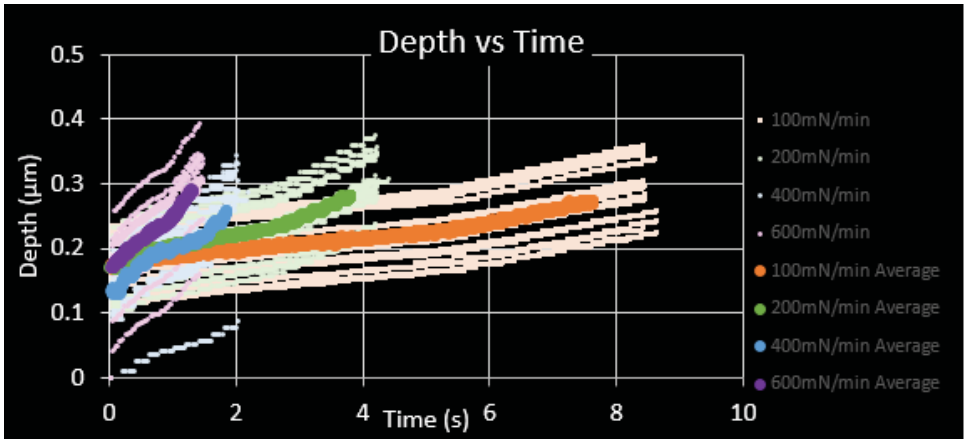

Figure 56: Depth vs time chart for the third peak of the mill-annealed sample.

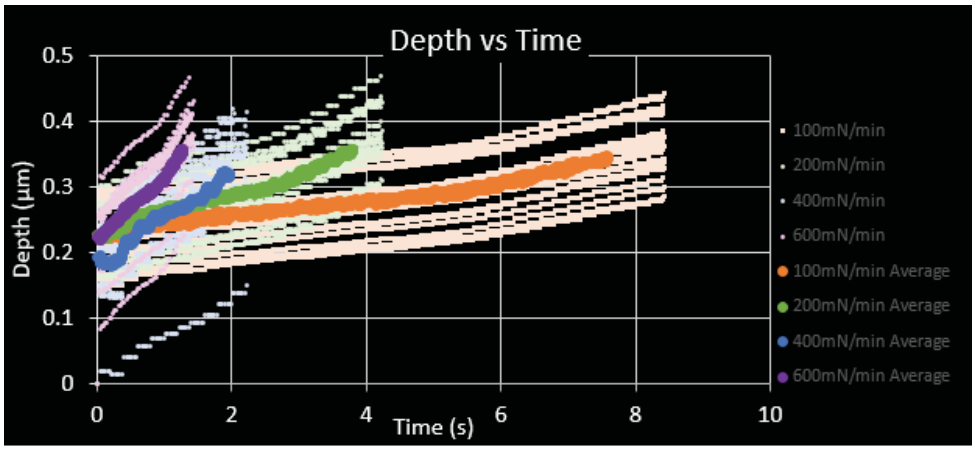

Figure 57: Depth vs time chart for the fourth peak of the mill-annealed sample.

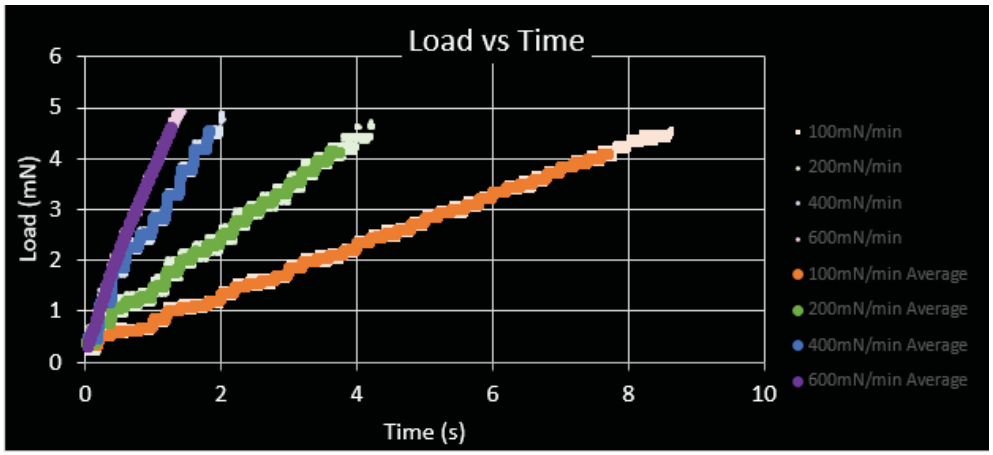

Figure 58: Load vs time chart for the first peak of the EBM sample.

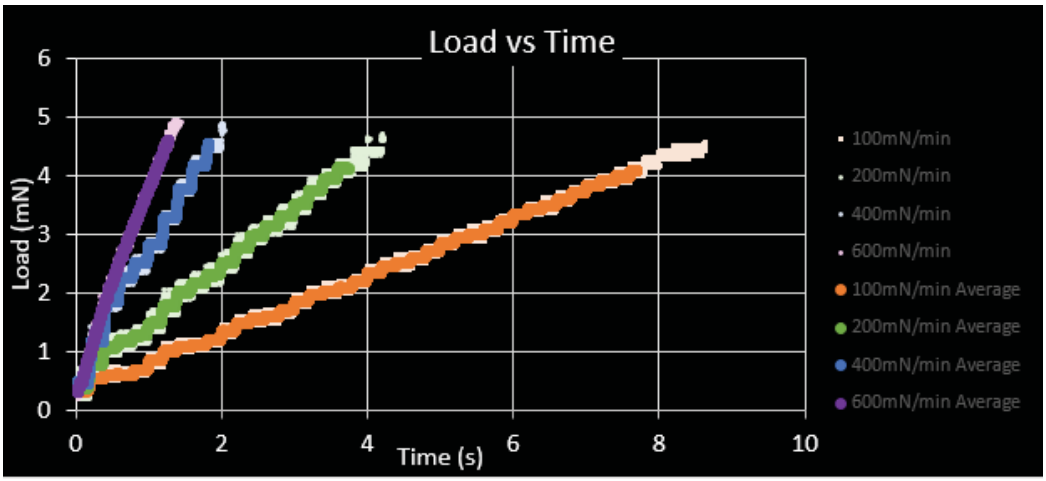

Figure 59: Load vs time chart for the second peak of the EBM sample.

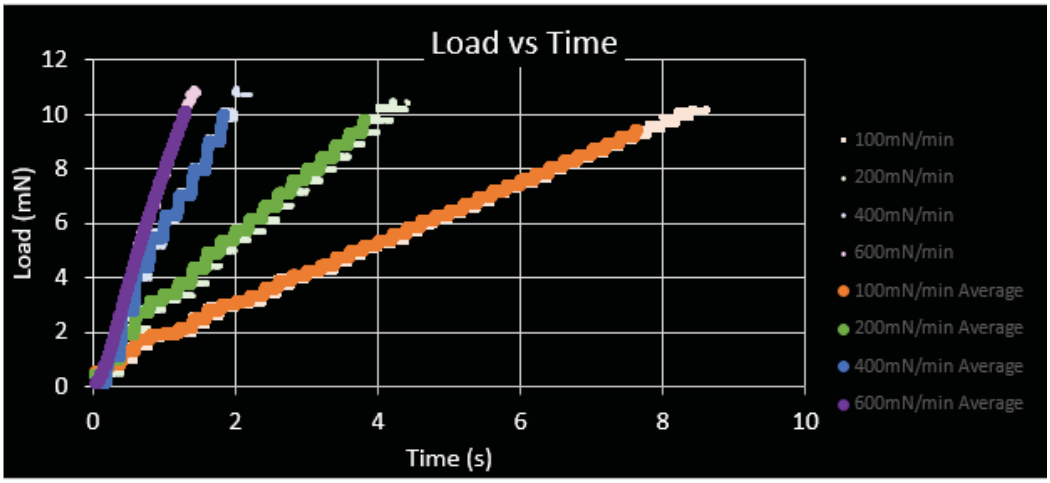

Figure 60: Load vs time chart for the third peak of the EBM sample.

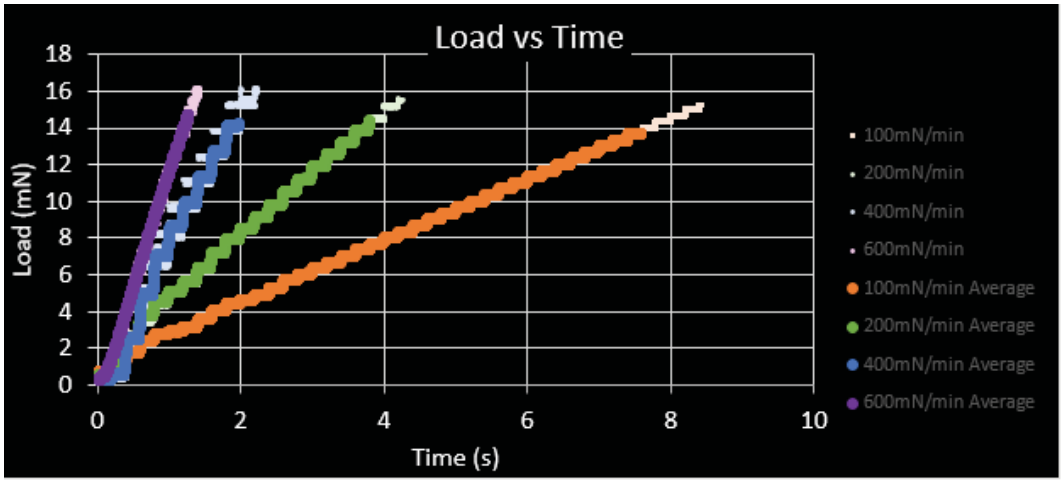

Figure 61: Load vs time chart for the fourth peak of the EBM sample.

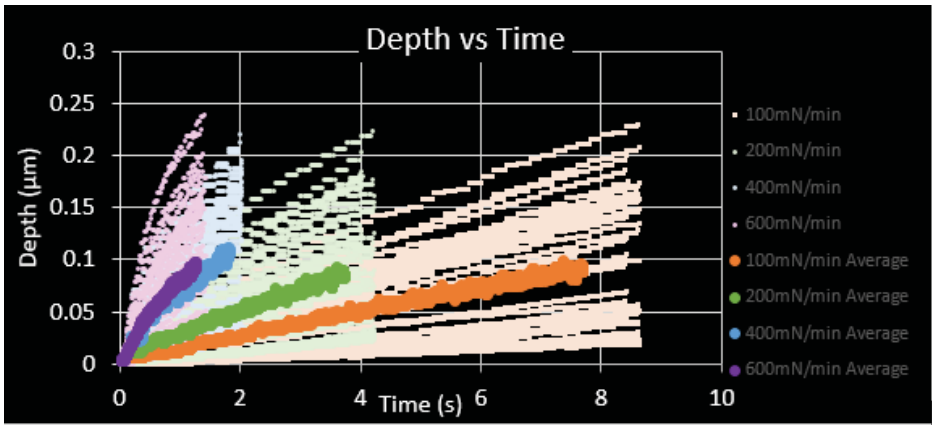

Figure 62: Depth vs time chart for the first peak of the EBM sample.

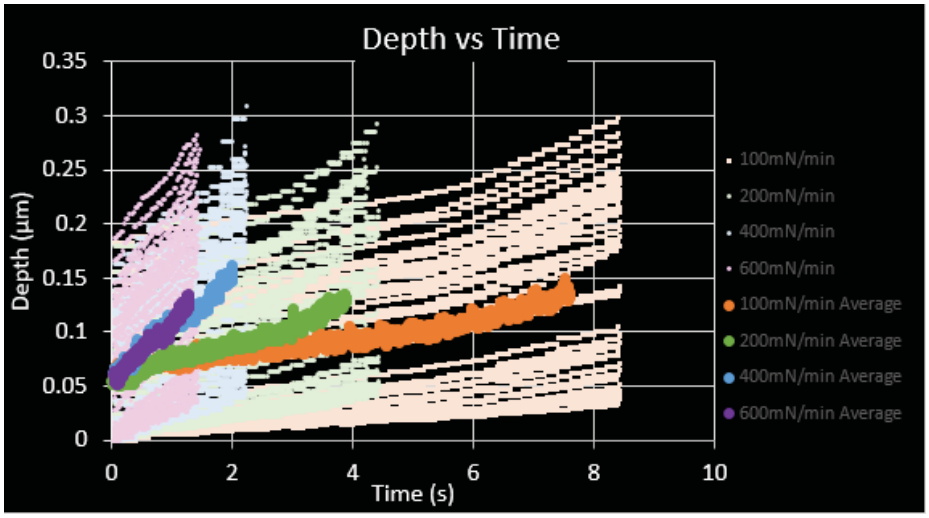

Figure 63: Depth vs time chart for the second peak of the EBM sample.

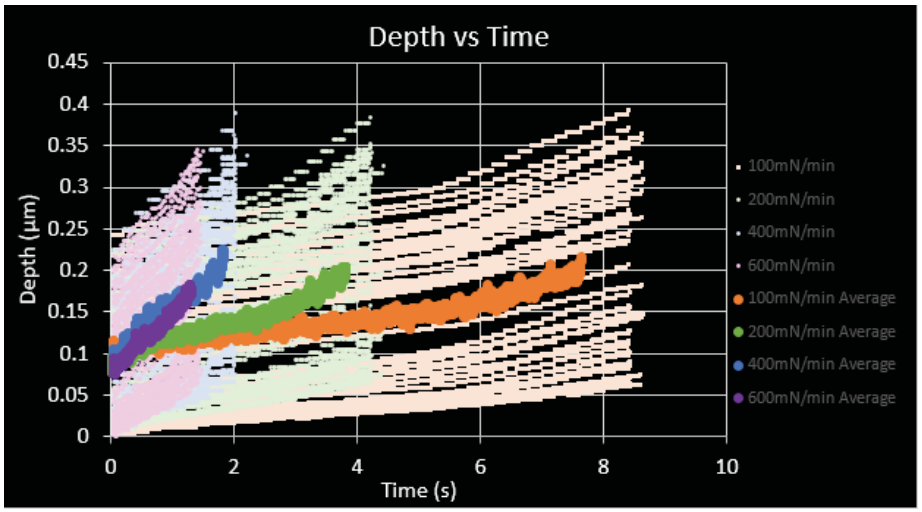

Figure 64: Depth vs time chart for the third peak of the EBM sample.

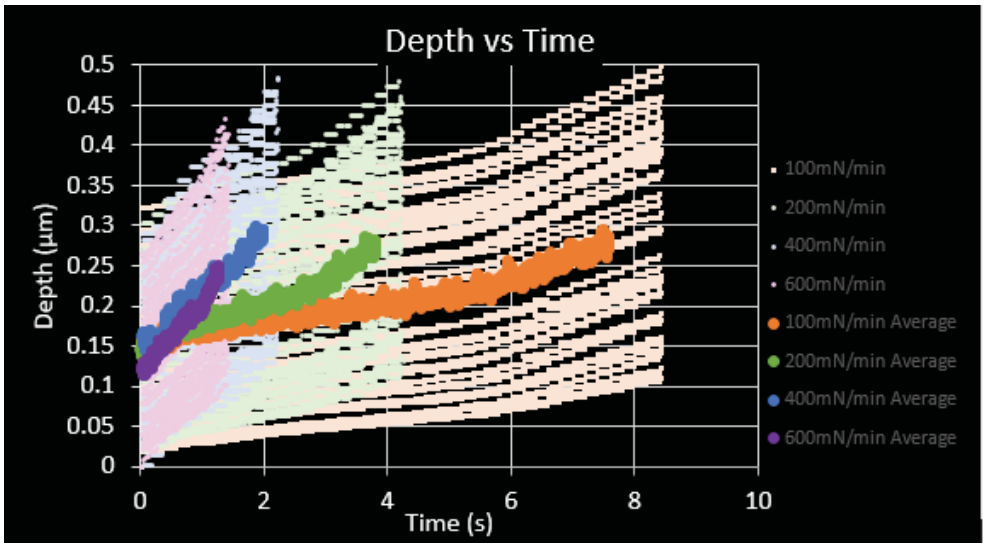

Figure 65: Depth vs time chart for the fourth peak of the EBM sample.

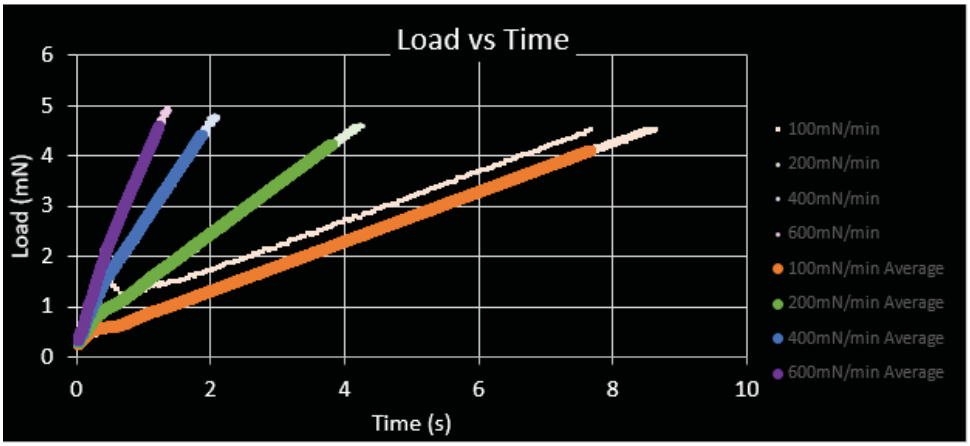

Figure 66: Load vs time chart for the first peak of the SLM sample.

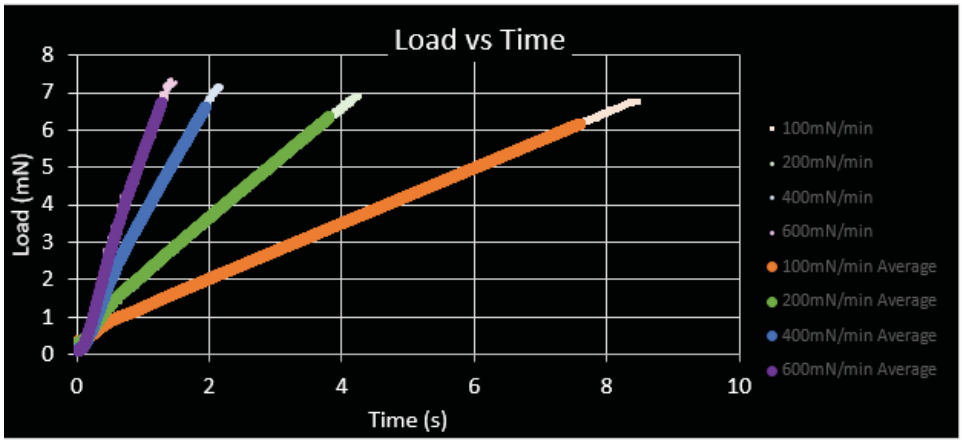

Figure 67: Load vs time chart for the second peak of the SLM sample.

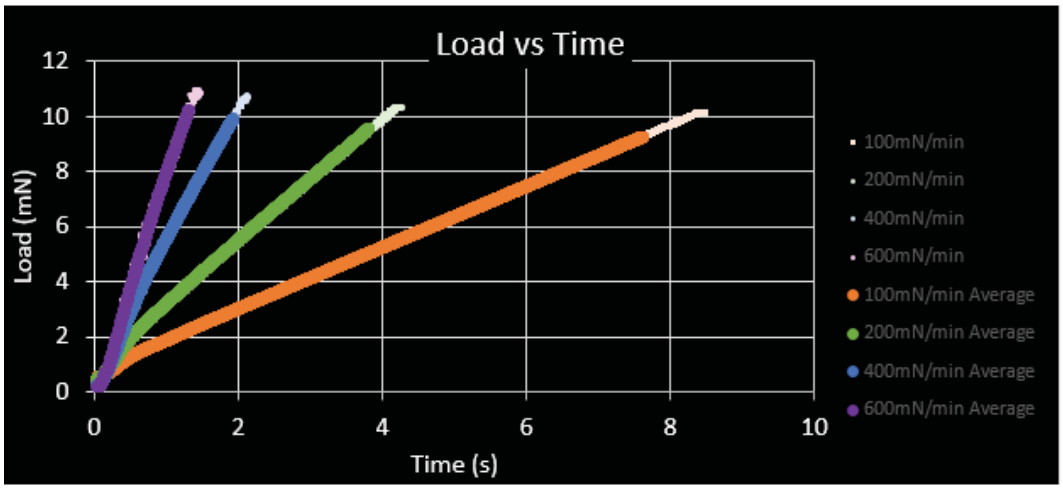

Figure 68: Load vs time chart for the third peak of the SLM sample.

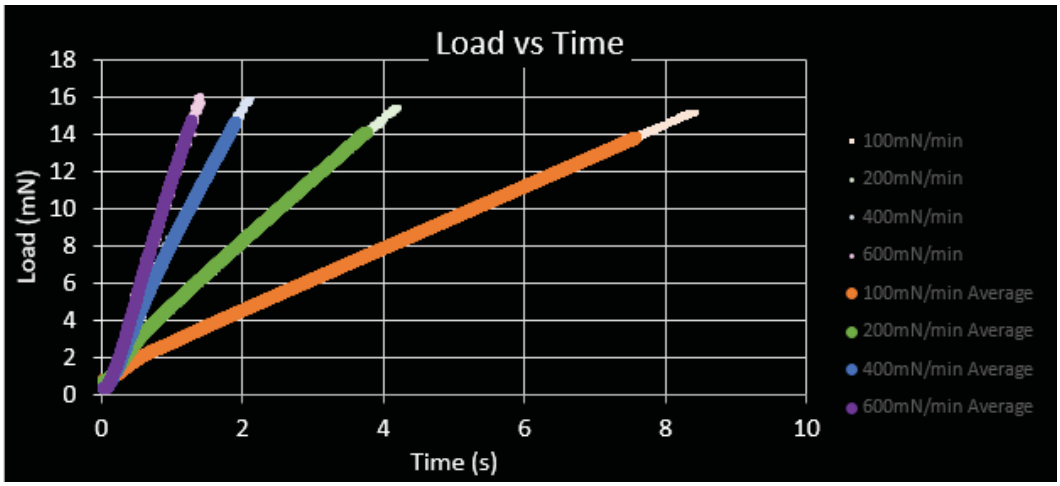

Figure 69: Load vs time chart for the fourth peak of the SLM sample.

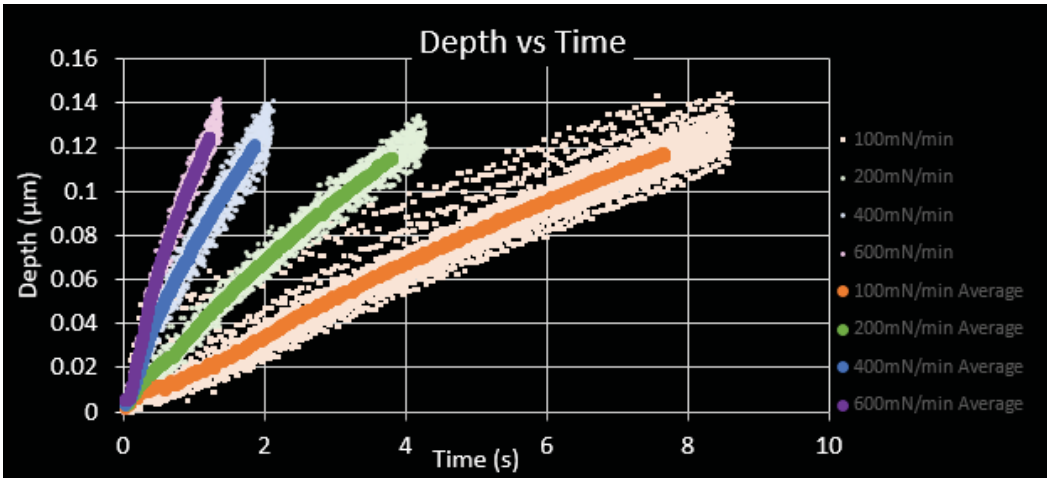

Figure 70: Depth vs time chart for the first peak of the SLM sample.

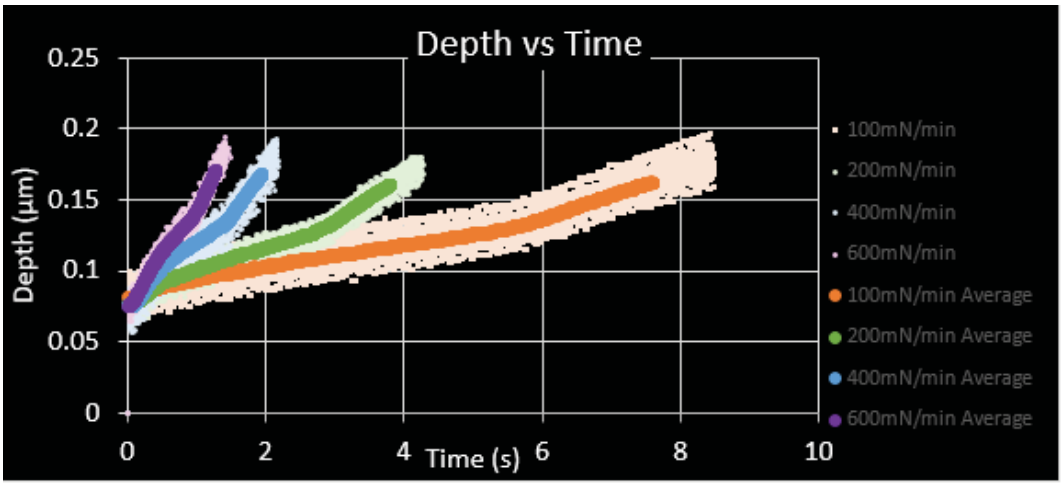

Figure 71: Depth vs time chart for the second peak of the SLM sample.

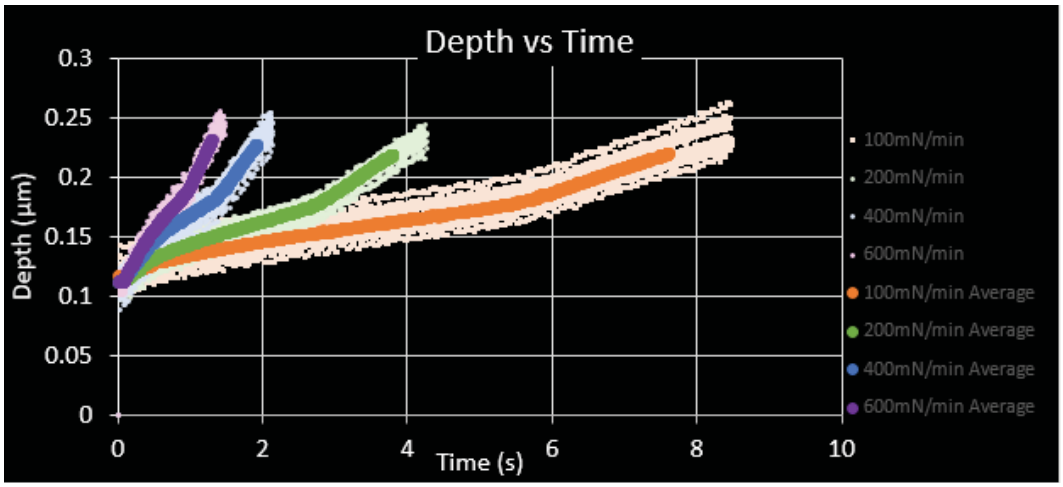

Figure 72: Depth vs time chart for the third peak of the SLM sample.

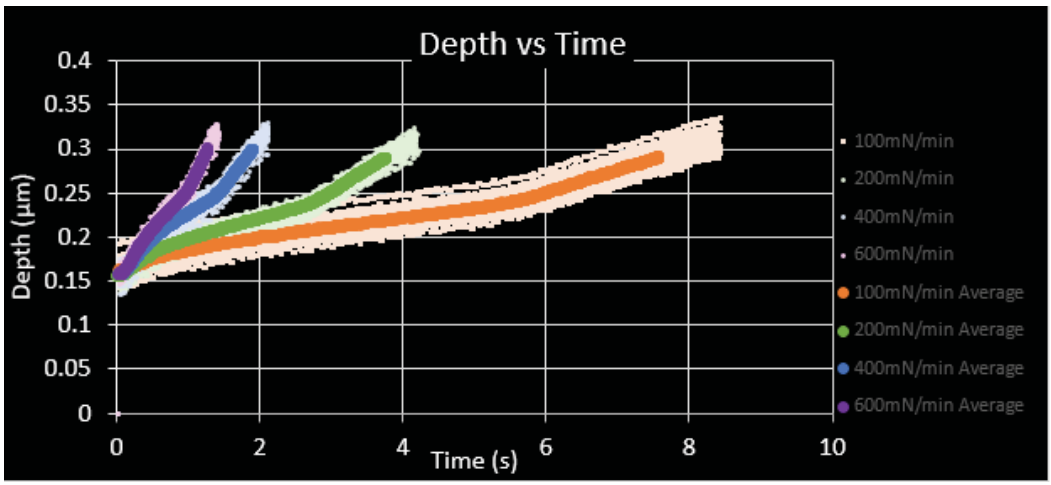

Figure 73: Depth vs time chart for the fourth peak of the SLM sample.

The elastic modulus was calculated using the unloading curve for each individual peak. As before with the single indentation tests, there is a trend of increasing modulus of elasticity with increasing strain rate.

Table 13: Average elastic modulus at each peak.

Modulus of Elasticity (GPa)				
depth	.13µm	.18µm	.25µm	.33µm
M-A	129.75	120.83	117.73	129.3
EBM	176.39	186.72	165.61	164.57
SLM	103.88	108.05	112.45	117.37

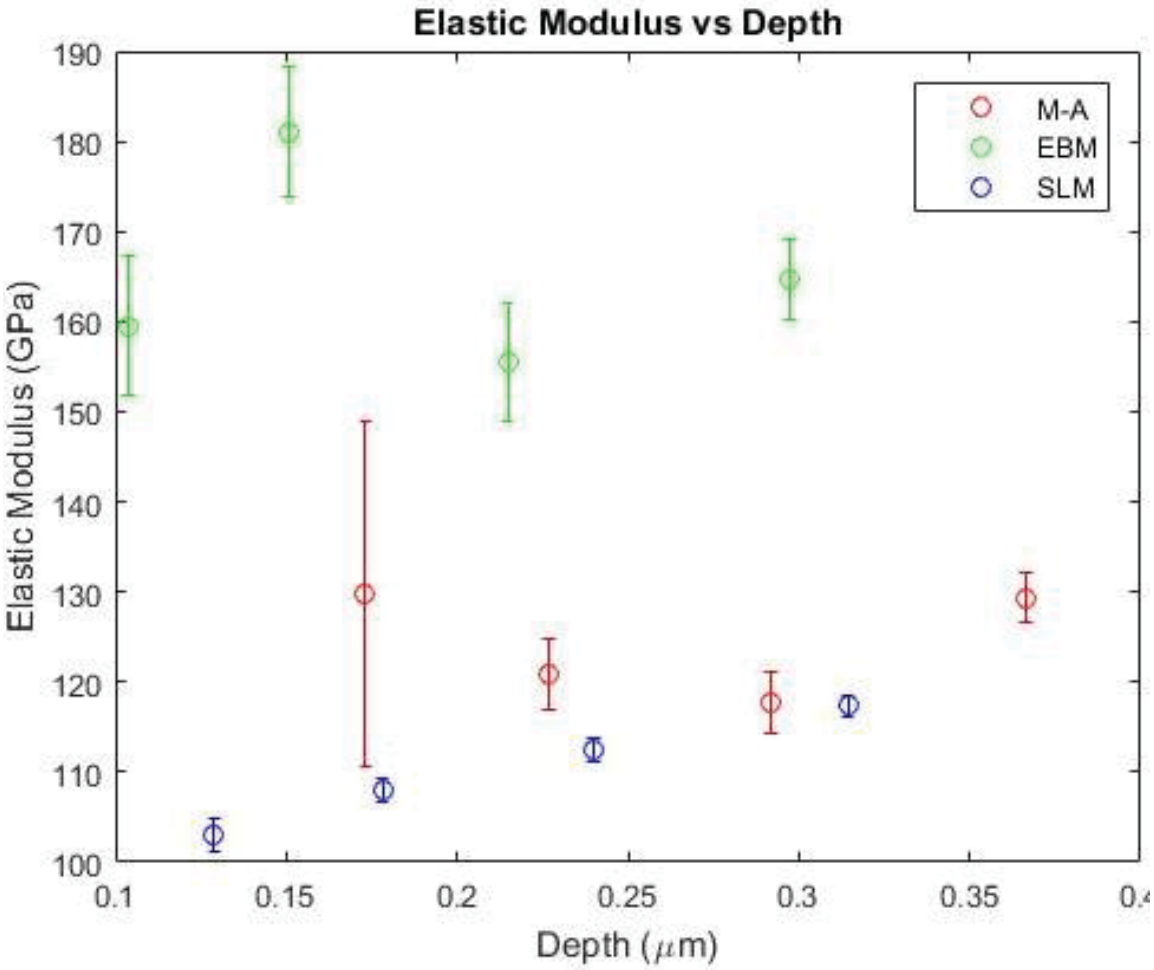

Figure 74: Chart of average elastic modulus vs depth for all samples.

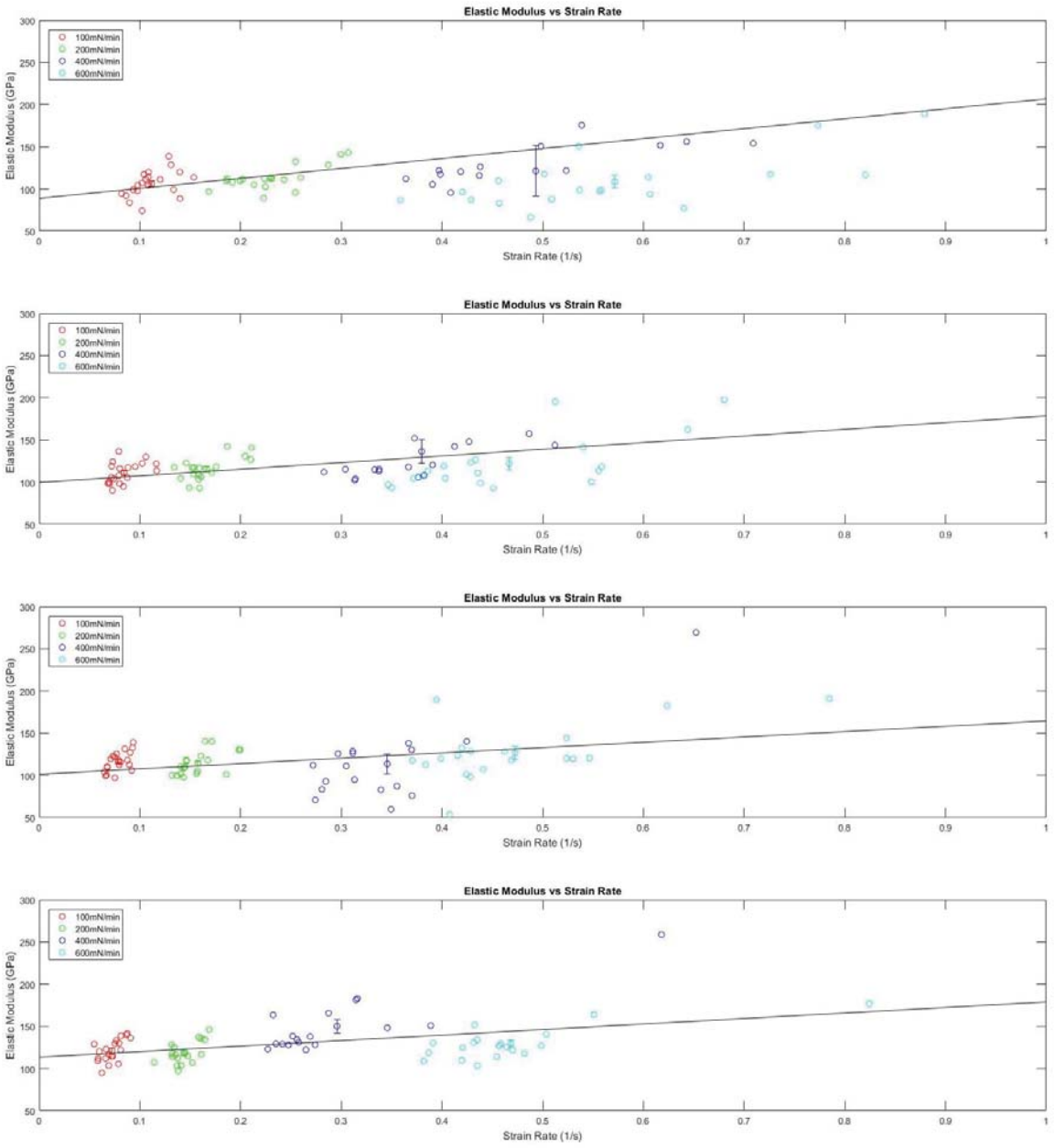

Figure 75: The modulus of elasticity vs strain rate of all four peaks of the mill-annealed sample.

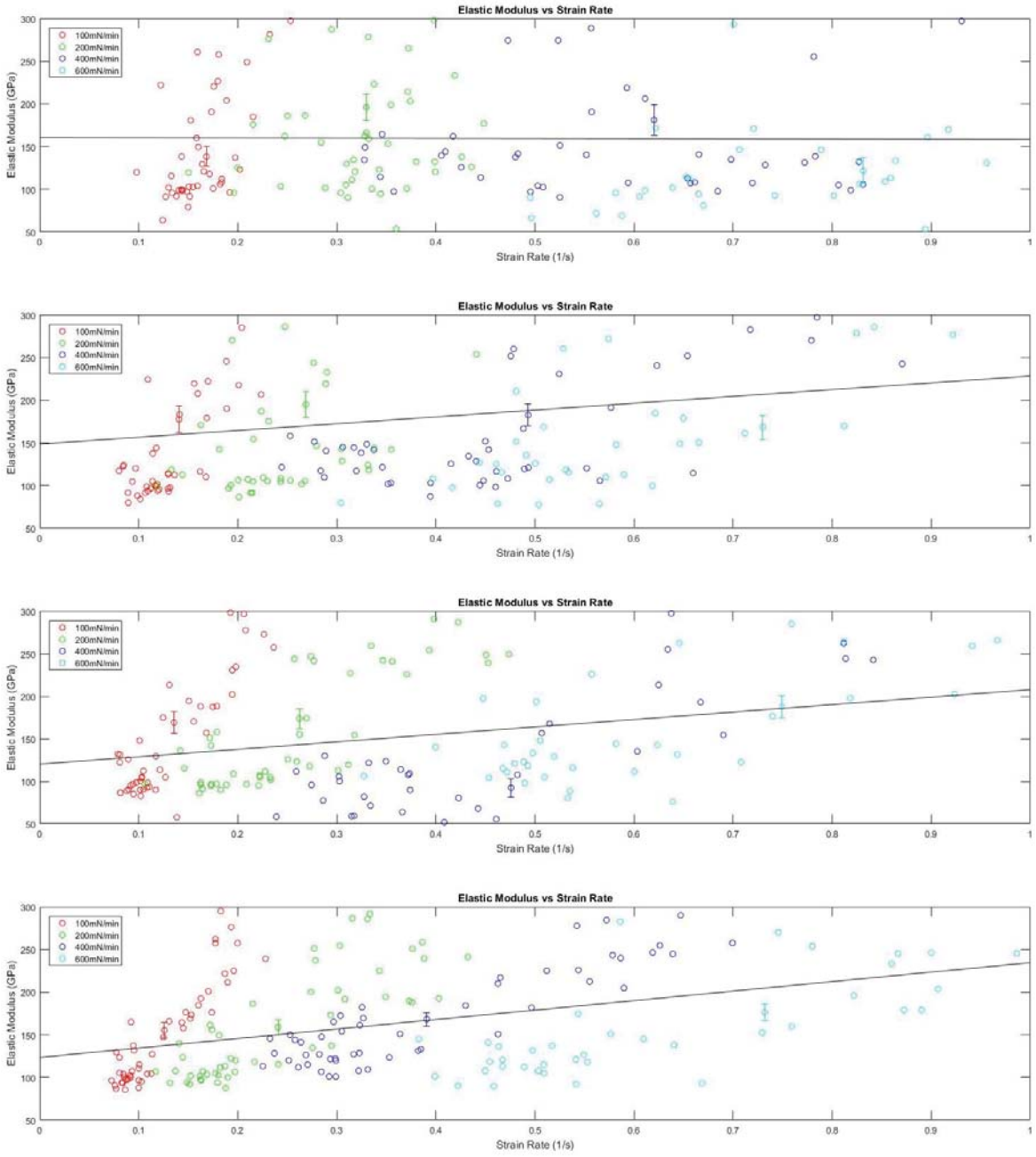

Figure 76: The modulus of elasticity vs strain rate of all four peaks of the EBM sample.

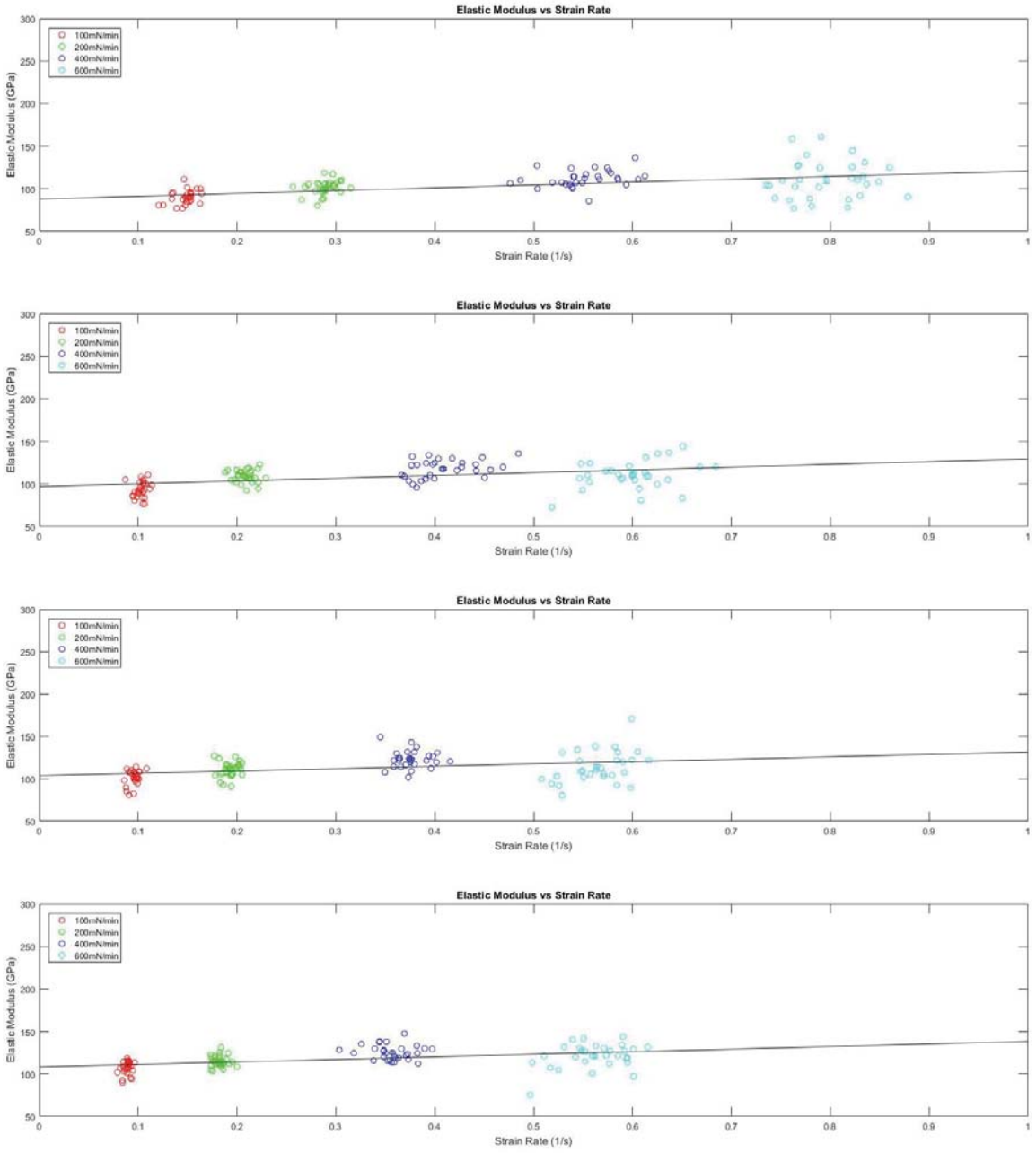

Figure 77: The modulus of elasticity vs strain rate of all four peaks of the SLM sample.

From the data collected, the marten's hardness was then calculated as it was before. The data is then graphed to view the strain rate sensitivity from each peak at different loading rates. The EBM sample had a high hardness value when compared to the other samples. The mill-annealed sample was the softest.

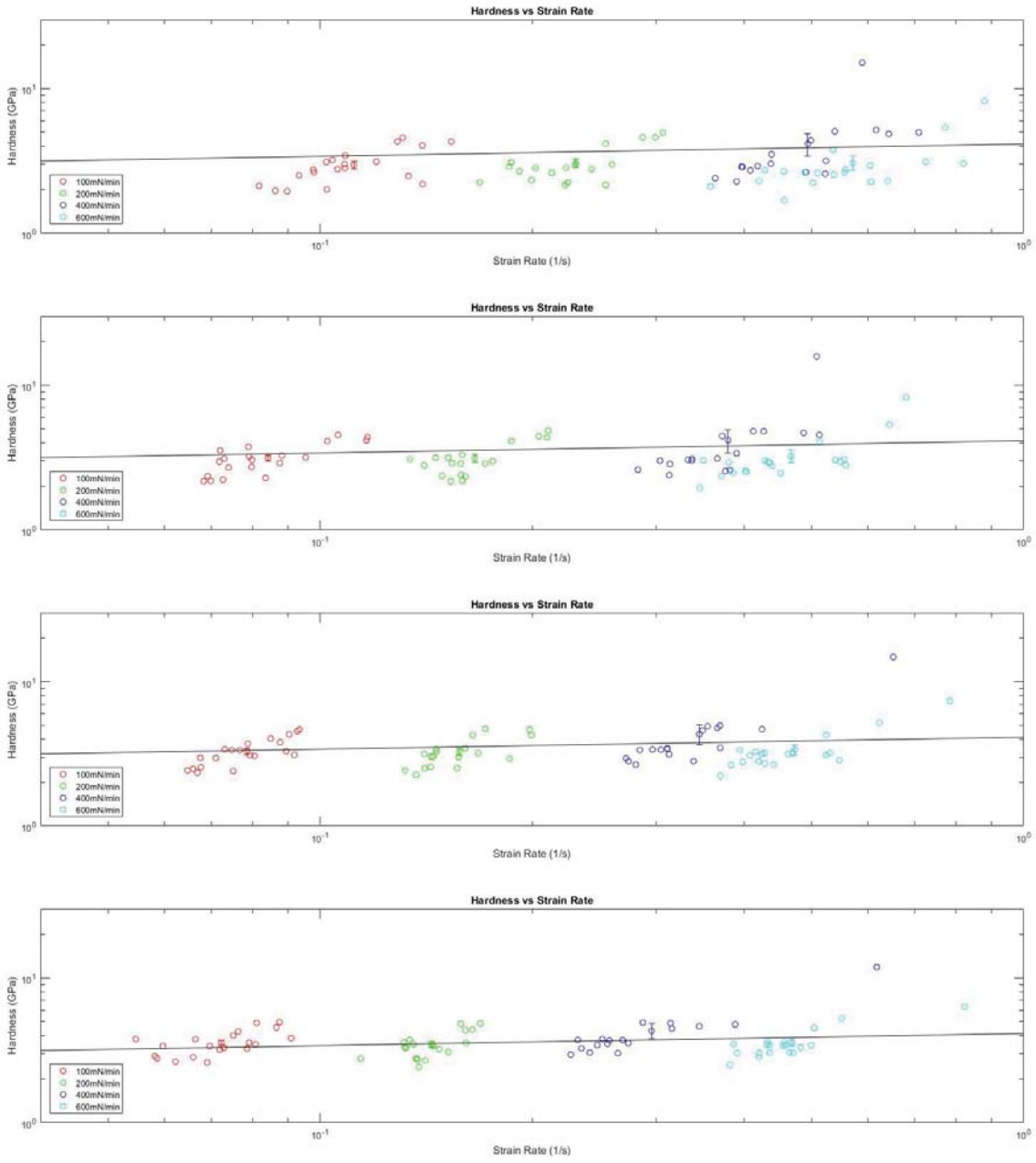

Figure 78: Hardness vs strain rate for the four peaks in the multiload test performed on the mill-annealed sample.

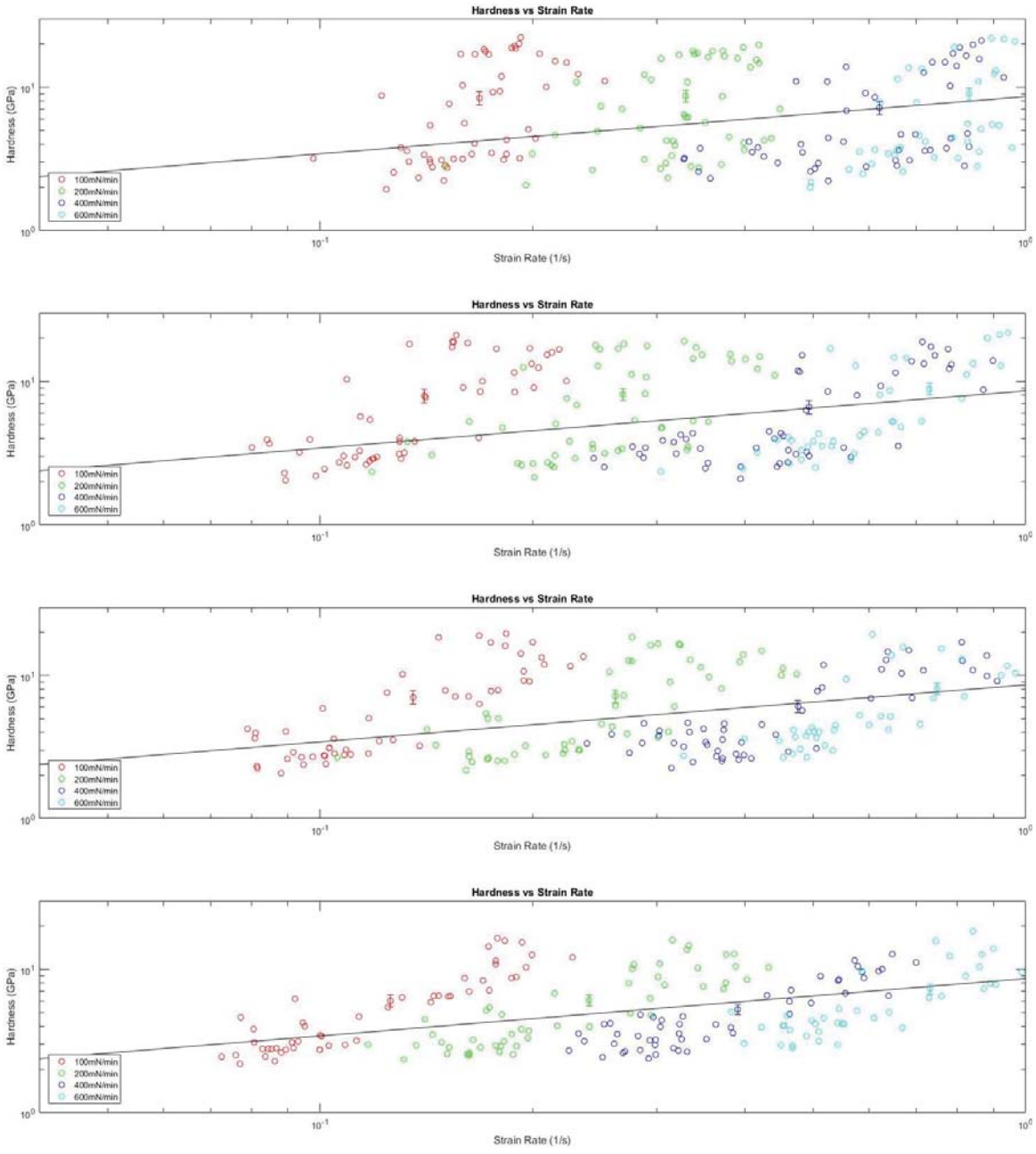

Figure 79: Hardness vs strain rate for the four peaks in the multiload test performed on the EBM sample.

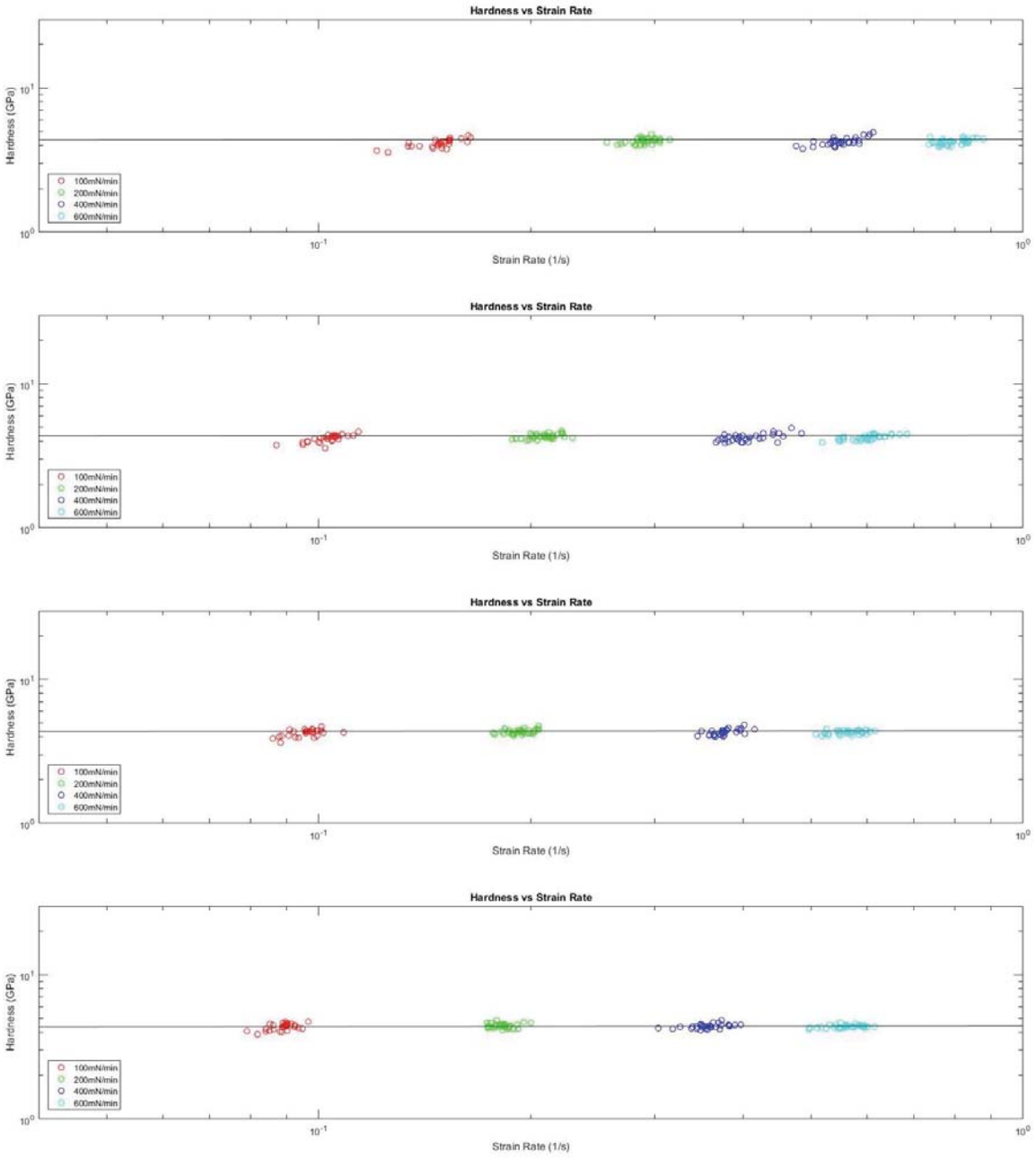

Figure 80: Hardness vs strain rate for the four peaks in the multiload test performed on the SLM sample.

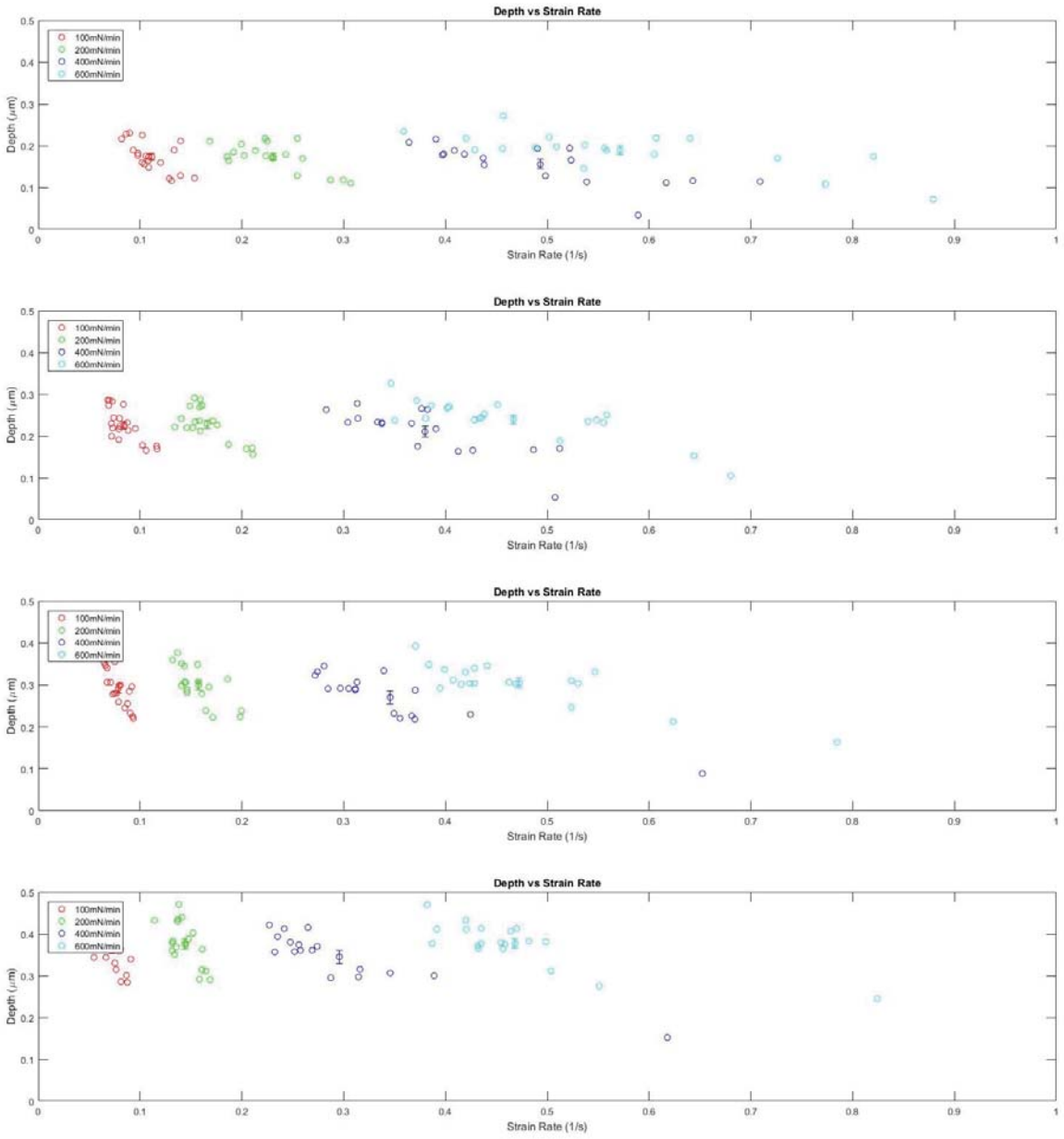

Figure 81: Depth vs strain rate for the four peaks in the multiload test performed on the mill-annealed sample.

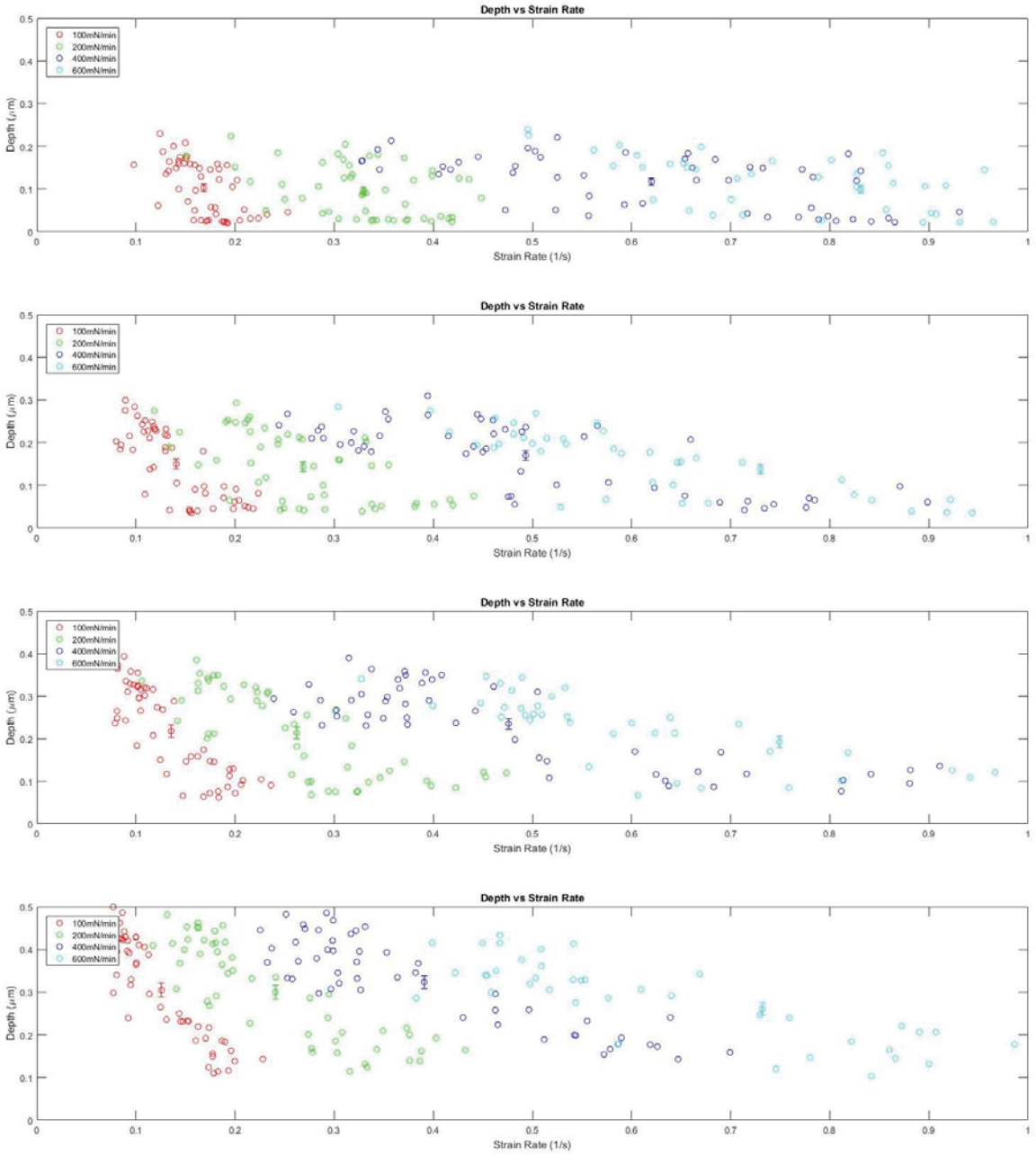

Figure 82: Depth vs strain rate for the four peaks in the multiload test performed on the EBM sample.

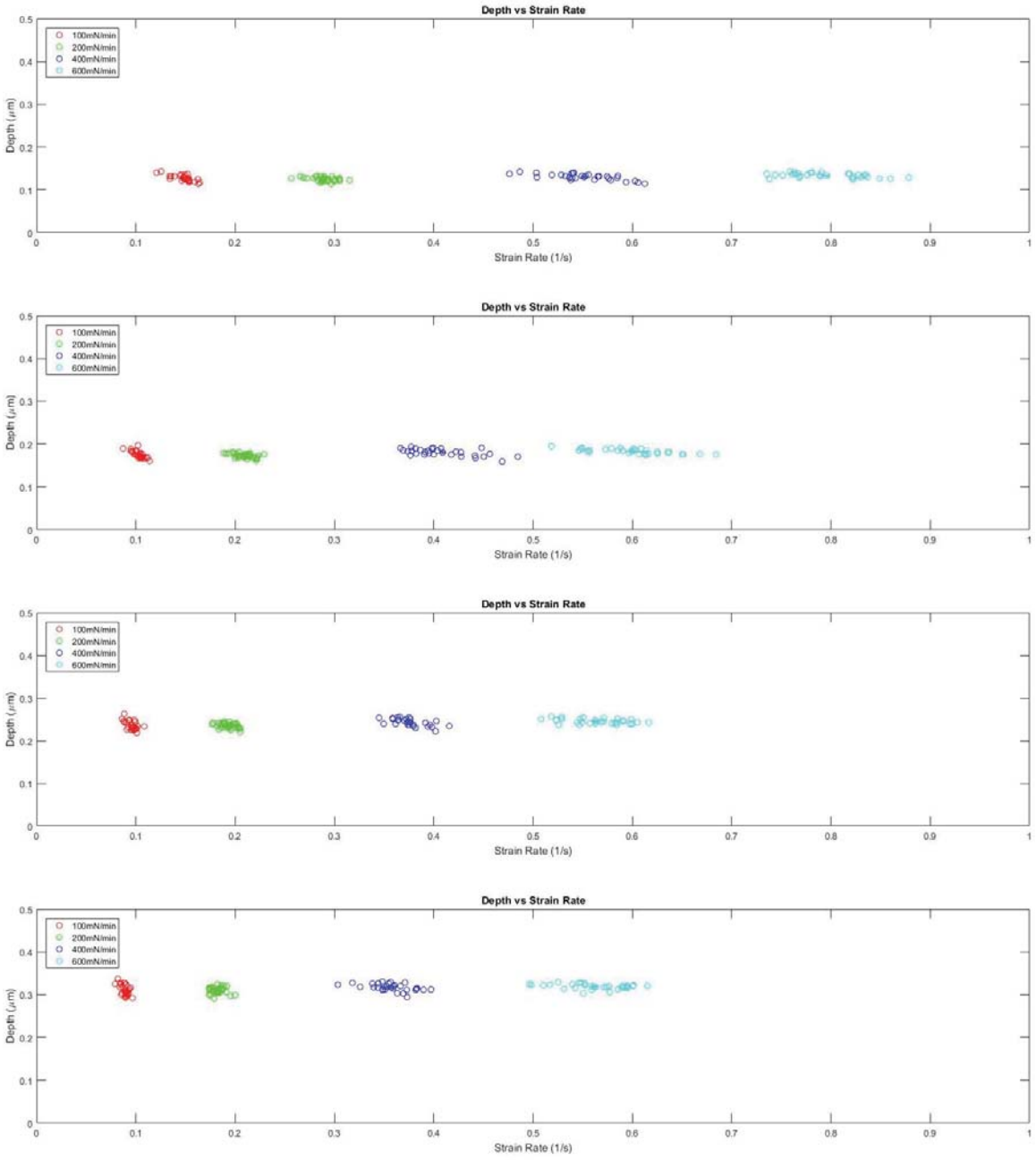

Figure 83: Depth vs strain rate for the four peaks in the multiload test performed on the SLM sample.

The results show that the electron beam melted sample is highly sensitive to strain rate. The mill-annealed titanium also exhibits strain rate sensitivity, but the selected laser melted sample is not very sensitive. Interestingly, for the mill-annealed and selective

laser melted samples strain rate sensitivity seems to decrease at the higher peak load. This could be a correlation between fatigue and strain rate sensitivity. Another possible influence could be a strain hardening effect on the surface as the indenter continues to plastically deform the same point.

Table 14: Strain rate sensitive of each sample.

Strain Rate Sensitivity

Depth	.13μm	.18μm	.25μm	.33μm
M-A	0.1468	0.1202	0.1187	0.084
EBM	0.2272	0.3749	0.4136	0.3993
SLM	0.016	0.0108	0.0069	0.0035

By analyzing the data at each peak (and subsequently each depth) and then comparing the hardness at the last peak of 15mN to the single indent hardness, it is possible to determine if strain hardening is occurring. The mill-annealed and selective laser melted samples both increase hardness with indentation cycle, but the electron beam melted sample shows a negative trend.

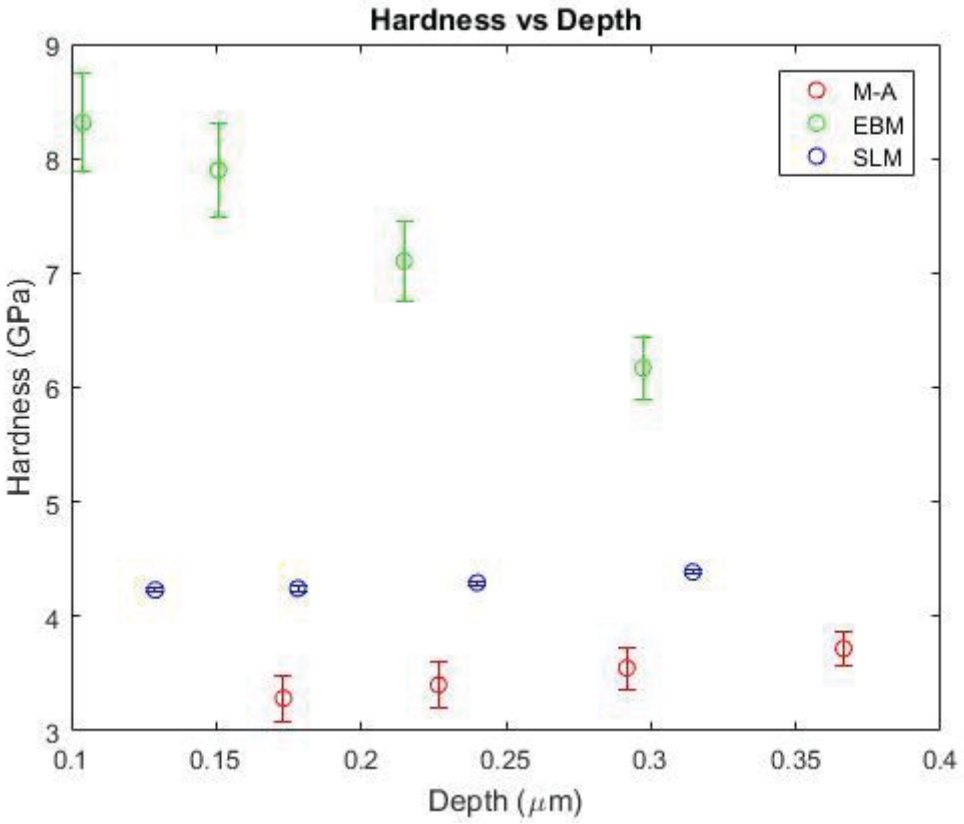

Figure 84: Comparison of the average hardness values at each peak of the multi-load test.

When the hardness is compared to the results from the single indentation test, it shows that the selective laser melted material does not change much in hardness and is close to the value for the single indentation for all cycles. This implies that strain hardening is only a small factor and the dependence of hardness on depth is insignificant.

For mill-annealed, as the depth increases, the hardness is approaching the hardness of the single indentation tests concluding that depth does play a role on hardness for this sample. Also since the hardness is slightly lower, it can be inferred that strain rate did not play a significant role.

For the electron beam melted material, as the number of cycles increases on the multi-load test, there is a negative correlation with hardness. This indicates that the

electron beam melted sample was subject to fatigue. There is most likely a negative correlation of hardness and depth. The result shows that the hardness value is much higher than the single indentation test which may indicate that there is significant strain rate hardening happening as the load is cycled. Otherwise if there was no strain rate hardening, the hardness would end up lower and approach the hardness of the single indentation results.

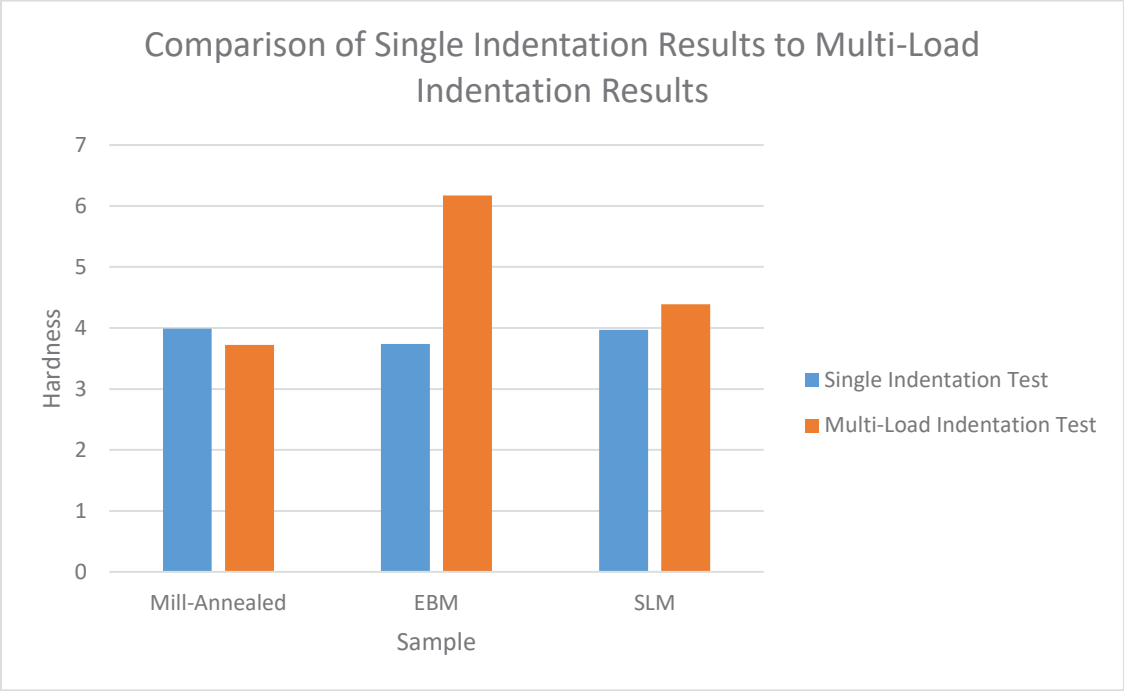

Figure 85: Comparison between single indentation test results and multi-load indentation test results.

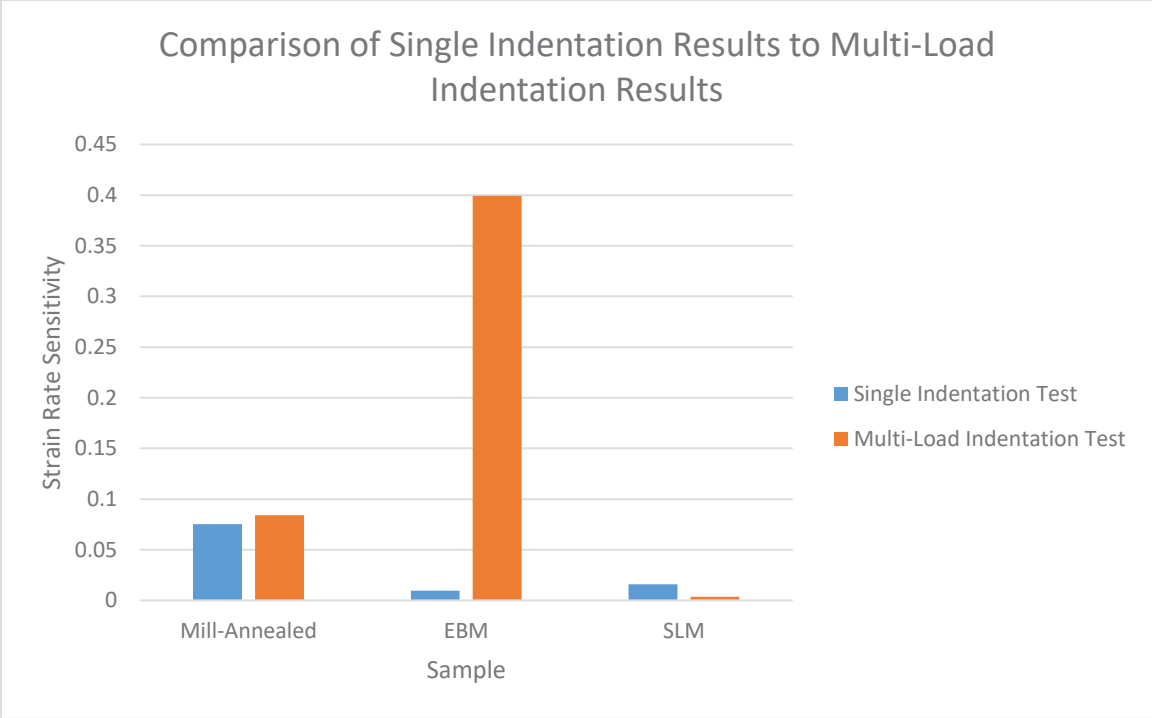

Figure 86: Comparison of strain rate sensitivity between single indentation tests and multi-indentation tests.

CHAPTER 3: PROGRESSIVE WEAR TESTS

3.1 Introduction

With knowledge of the strain rate sensitivity of the three samples of Ti-6Al-4V, the comparison to wear rate can be established. The tests performed are known as progressive sliding wear tests which include increasing the load on the indenter as it slides across the surface until maximum load is reached. The wear is a result of local plasticity when single asperities collapse. This is similar to a running-in wear mechanism. At maximum load, the indenter is retracted and the test is complete. The tests conducted here included a prescan of the surface, the progressive wear test, and a final scan.

Since the ball was spherical in shape, it is possible to calculate the stress on the surface of the part using the Hertzian contact stress theory which is used to find the local contact stress between two surfaces. In this case, it is an elastic sphere and an elastic half-space. The pressure on the surface is variable, but the maximum contact pressure can be calculated by (32):

$$p_0 = \frac{3F}{2\pi a^2} = \frac{1}{\pi}\left(\frac{6FE^{*2}}{R^2}\right)^{\frac{1}{3}} \qquad \text{Eq. (17)}$$

Where F is the applied force, R is the radius of the sphere, d is the depth, and a is the contact radius calculated by:

$$a = \sqrt{(Rd)} \qquad \text{Eq. (18)}$$

3.2 Methods

The three samples used before were again cleaned and sonicated to remove any contaminants. They were then placed into the Nanovea nanoindentation machine where a smooth, flawless surface was found. The surface was then scanned with an optical profilometer to determine levelness and roughness. When the surface was sufficiently

level, it was moved underneath the indenter where a 1mm diameter silicon nitride sphere was installed. The properties of the silicon nitride indenter were gathered from the manufacturer: 310GPa elastic modulus, 0.27 Poisson's ratio.

Table 15: Surface profilometry of the surfaces for the scratch test.

Surface Profilometry

	M-A	EBM	SLM
Slope - X	0.0761°	0.0489°	-0.0345°
Slope - Y	0.0368°	-0.1019°	0.0788°
CLA - X	0.1758µm	0.1174µm	0.0903µm
CLA - Y	0.2091µm	0.0935µm	0.0195µm

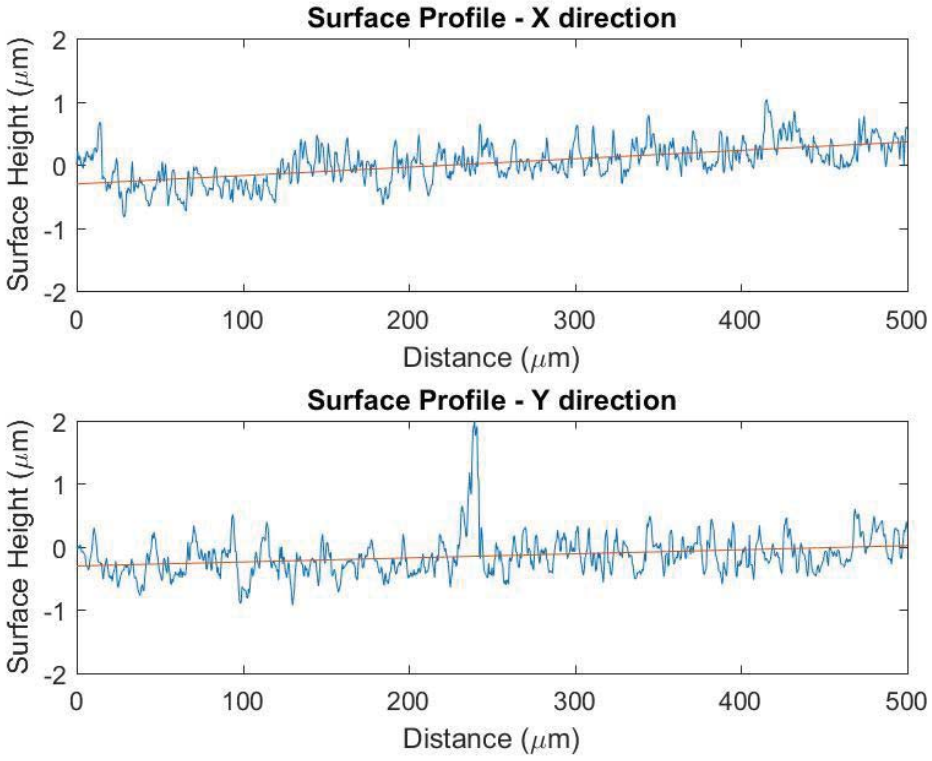

Figure 87: Surface profile of the mill-annealed surface near the scratch test area.

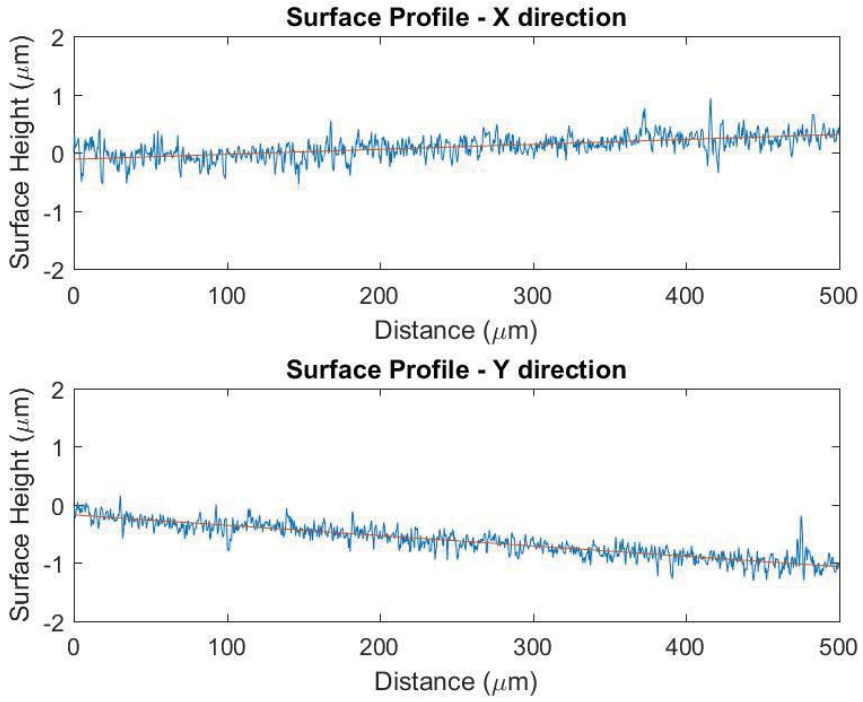

Figure 88: Surface profile of the EBM surface near the scratch test area.

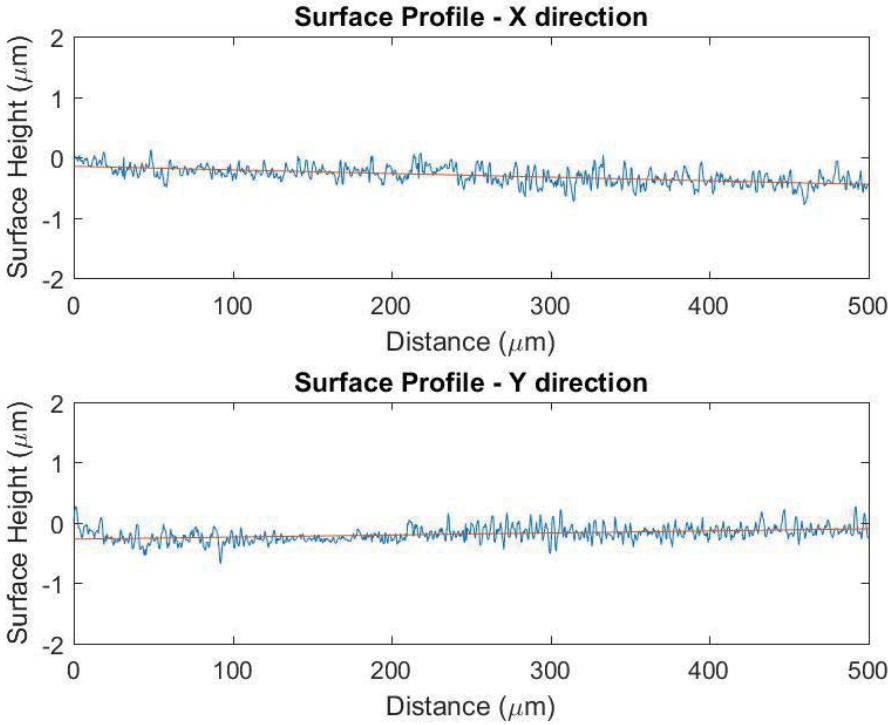

Figure 89: Surface profile of the SLM surface near the scratch test area.

A maximum force of 15mN was applied to the indenter tip. Using the elastic modulus found in the single indentation tests, and a Poisson's ratio of 0.32, the theoretical contact stress was found.

Table 16: Theoretical stress on the sample surface from a 15mN load on the spherical indenter.

Hertzian Contact Stress (MPa)		
M-A	EBM	SLM
498	510	481

To begin the test, the indenter was slowly lowered until contact was made with the surface. It was then retracted and moved to an unaltered spot to avoid residual surface distortion. The indenter was then slowly loaded at 0.1μm/min until a contact load of 0.2mN was achieved, the indenter was slid along the surface creating the surface profile for the scratch area. Then it was retracted and returned to the original position. Again, it approached the surface until a contact of 0.2mN. The indenter was immediately moved at a given speed as it was continually loaded at a specific rate until a maximum load was achieved. Then it retracted and returned to the original position. The speed and rate were varied for each test. The tests were done with speeds of 0.4mm/min, 0.8mm/min, and 1.6mm/min. The loading rates were 100mN/min, 200mN/min, 400mN/min, and 600mN/min performed on each sliding speed rate. After the scratch, another scan was performed as the original one was.

Table 17: Testing parameters for the scratch test.

Testing Parameters				
	Test Set 1	Test Set 2	Test Set 3	Test Set 4
Loading Rate	100mN/min	200mN/min	400mN/min	600mN/min
Unloading Rate	100mN/min	200mN/min	400mN/min	600mN/min
Contact Speed	1µm/min			
Contact Load	0.2mN			
Scratch Speeds (mm/min)	0.4, 0.8, 1.6			
Peak Load	15mN			
Number of Tests	3			

Using the profiles seen on Figure 90, the scratch depth can be measured by subtracting the initial scan from the original depth. As expected, the scratch depth gets deeper as more load is applied.

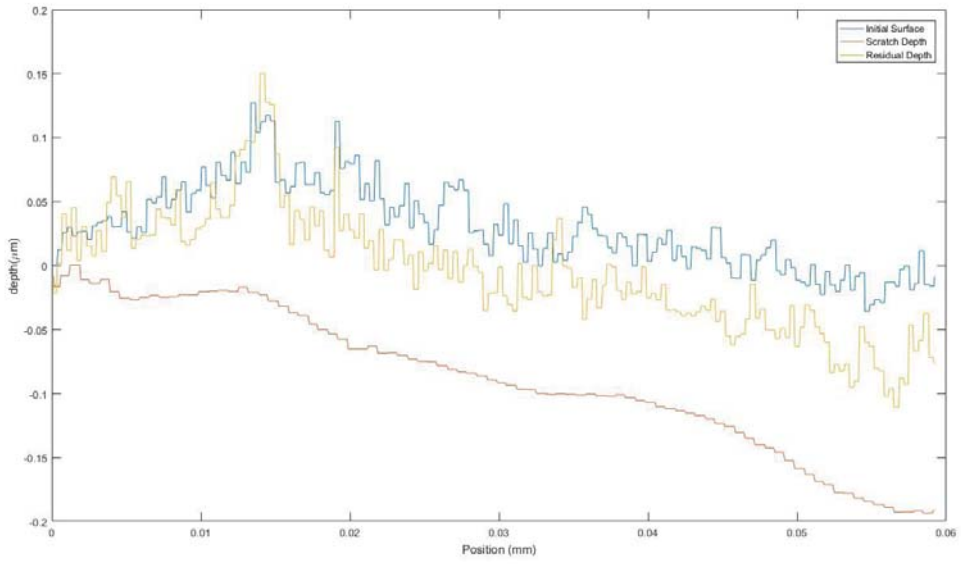

Figure 90: Typical scratch test profiles.

Each test was repeated three times and the average values are shown in their respective charts. The wear values show the selective laser melted material has the most

wear, and the mill-annealed material has the least wear. It must be taken into consideration that the selective laser melted material has a much smoother surface which will affect wear rate.

The charts show an inverse correlation between loading rate and wear depth indicating that wear is affected by strain rate sensitivity. Another noticeable attribute is that the wear rate correlation at 0.4mm/min sliding rate seems to deviate between loading rates. This may be because at a lower sliding speed there is more time for adhesion to occur causing more adhesive wear and less abrasive wear.

The selective laser melted values at 600mN/min have a very large deviation from the other values which cannot be explained at this time.

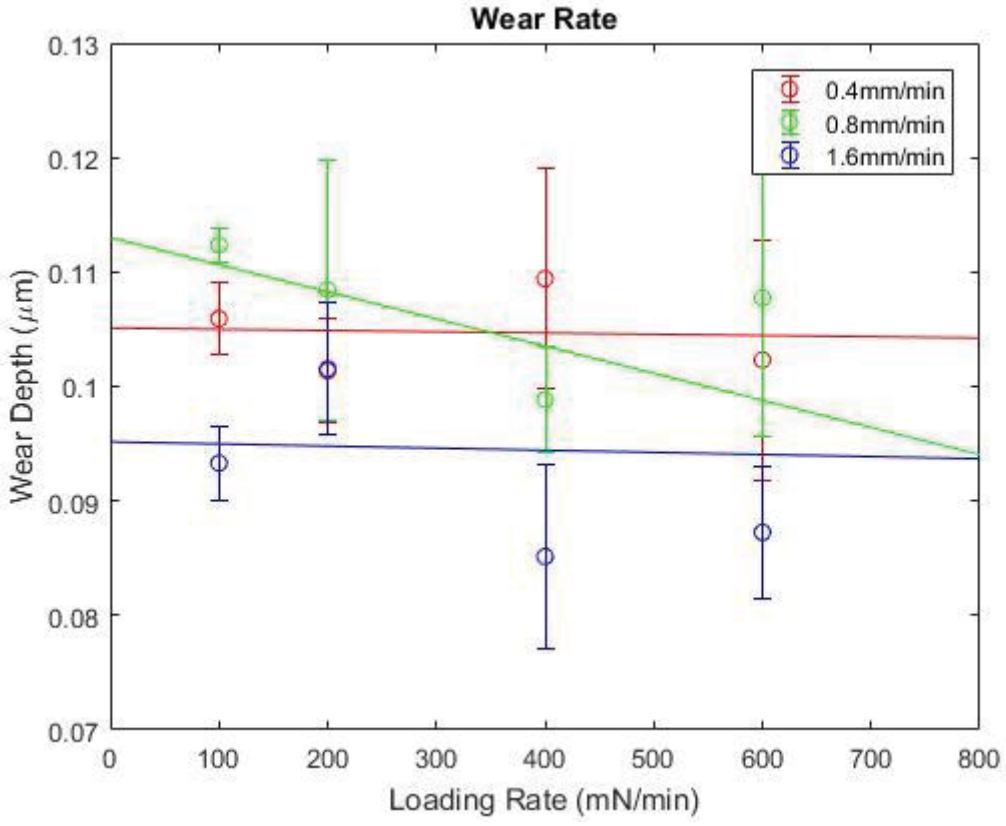

Figure 91: Wear values for the mill-annealed sample.

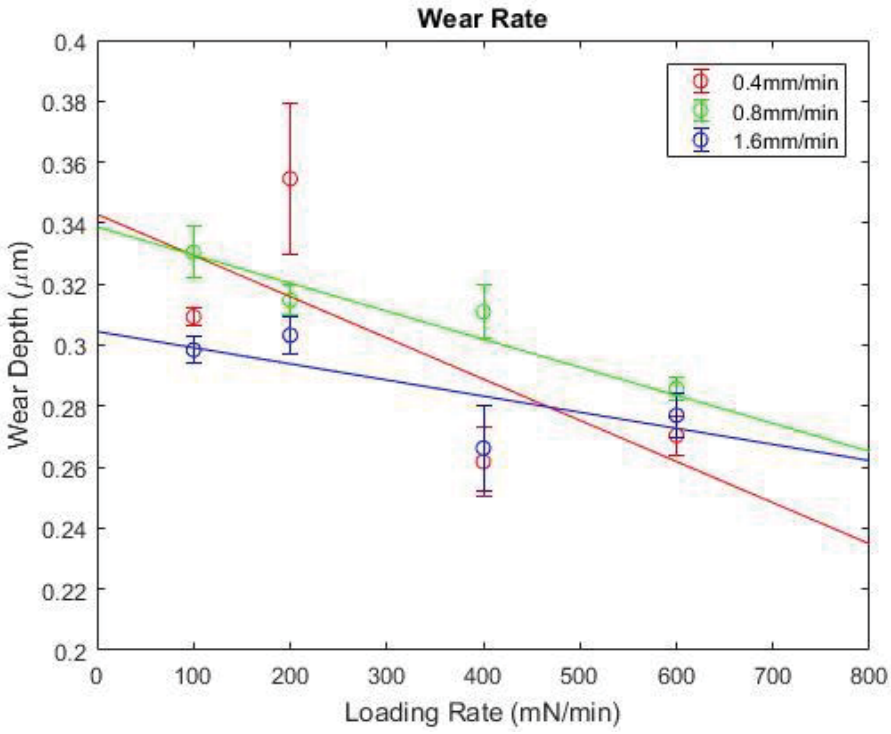

Figure 92: Wear values for the EBM sample.

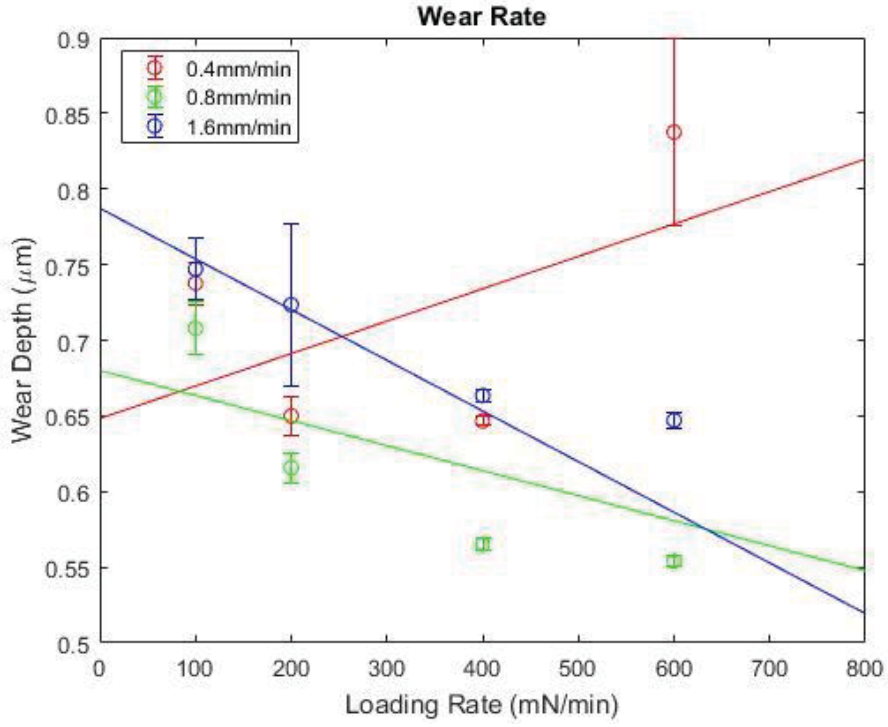

Figure 93: Wear Values for the SLM sample.

CHAPTER 4: CONCLUSION

4.1 Discussion of Results

These experiments in this paper investigate the effect of strain rate sensitivity on wear for conventional mill-annealed as well as additive manufactured Ti-6Al-4V. Single constant rate loading indentation tests were performed to help understand the local strain rate sensitivity of the additive manufactured materials with their grain structures. Multi-load constant rate loading indentation tests were performed on the same samples to give backing to the single indentations and to provide insight on strain hardening and fatigue of the samples under a multi-load test. Finally, scratch tests were performed to determine the correlation between abrasive wear and strain rate.

Studies done here confirm that Ti-6Al-4V is sensitive to strain rate in the course grain mill-annealed form and the fine grain additive manufactured process such as electron beam melting and selective laser melting. The multi-load tests show that strain rate sensitivity has a dependency on how much fatigue the surface has experienced as well as the grain structure of the material. It can also be concluded that, at least at shallow depths, strain rate sensitivity is related to depth of indentation. It also seems that there is a positive correlation between strain rate and elastic modulus.

When the wear mechanism involves running-in (progressive transition before steady state friction), local plasticity occurs due to the collapse of contacting asperities. The fine grain structure found in additive manufactured dual phase titanium is related to plasticity. It is important to understand the change in properties for local plasticity in additive manufactured components. The results conclude that the progressive wear used in the experiments is sensitive to strain rate at least for normal loading rate. The data

found in this study is inconclusive on a relationship between wear rate and sliding rate of the surfaces.

4.2 Future work

It's known that the build direction of the additive manufactured surface influences the microstructure, such as layer boundaries. Since most mechanical parts involving friction and wear interact with more than a single surface, it is important to understand the effects of strain rate on the surfaces perpendicular with build orientation.

It was found here that strain rate sensitivity can be affected by the depth of the indent. It would be of interest to find results of wear tests at different loads and lengths to determine if there is a correlation. These tests may involve repeat progressive loads, or cyclic loads to increase depth of surface.

Finally, considering that porosity of additive manufactured materials has a relationship on fatigue, elasticity, and strength, and these characteristics are related to wear of the surface, it is critical that research be conducted to find relationships between wear rate and porosity.

References

1. *Microstructure and mechanical prop.* **Journal of Physics: Conference, Manikandakumar, Polishetty, Ashwin and Littlefair, Guy.** Geelong, Australia : s.n., 2015. The International Design Technology Conferen.

2. *Microstructure of Ti-6Al-4V produced by selective laser melting.* **Simonelli, M, Tse, Y Y and Tuck, C.** 2012, Journal of Physics: Conference, Vol. 371.

3. **Research and Development.** ***Fusion Implants.*** **[Online] [Cited: 11 6, 2017.] https://www.fusionimplants.com/r-d/.**

4. Electron Beam Melting. ***Arcam EBM.*** **[Online] Arcam. [Cited: 11 6, 2017.] http://www.arcam.com/technology/electron-beam-melting/.**

5. ***Effect of the build orientation on the mechanical properties and fracture modes of SLM Ti-6Al-4V.*** **Simonelli, M, Tse, Y Y and Tuck, C. 2014, Materials Science and Engineering, Vol. 616, pp. 1-11.**

6. ***A method for in.terpreting the data fro~ depth-sensing indentation.*** **Doerner, M. F. and Nix, W.D. 4, 1986, Journal of Materials Research, Vol. 1.**

7. Nanovea. Fracture Toughness Measurement using Nanoindentation. ***Nanovea.*** **[Online] [Cited: 11 6, 2017.] http://nanovea.com/App-Notes/nanofracturetoughness.pdf.**

8. —. Nanoindentation creep measurement. ***Nanovea.*** **[Online] [Cited: 11 6, 2017.] http://nanovea.com/App-Notes/nanocreepmeasurement.pdf.**

9. ***An Improved Technique for Determining Hardness and Elastic Modulus Using Load and Displacement Sensing Indentation Experiments.*** **Oliver, W.C. and Pharr, G. 6, s.l. : Journal of Materials Research, 1992, Vol. 7, pp. 1564-1583.**

10. Leroux, Pierre. An Indentation Test That Measures Yield Strength. ***ASM International.*** **[Online] [Cited: 11 6, 2017.] https://www.asminternational.org/documents/10192/1885193/amp16910p34.pdf/40591614-b9e0-4c38-90d0-e5d85ab5e164.**

11. Fischer-Cripps , Anthony C. ***Introduction to Contact Mechanics.*** **2. New York, NY : Springer Science+Business Media, LLC, 2007.**

12. ***A micro-indentation study of superplasticity in Pb, Sn, and Sn-38 wt% Pb.*** **M.J., Mayo and W.D., Nix. 8, s.l. : Acta Metallurgica, 1988, Vol. 36.**

13. Lucas, Neal Barry. ***An Experimental Investigation of Creep and Viscoelastic Properties Using Depth-Sensing Indentation Techniques.*** **s.l. : University of Tennessee, Knoxville, 1997.**

14. ***Mechanical properties of nanophase TiO2 as determined by nanoindentation.*** **Mayo, M.J., et al. 5, 1990, Journal of Material Research, Vol. 5, pp. 1073-1082 .**

15. ***Nanoindentation strain-rate jump tests for determining the local.*** **Maier, Verena, et al. 11, 2011, Journal of Materials Research, Vol. 26, pp. 1421-1430.**

16. ***Microstructures and Mechanical Properties of Ti6Al4V Parts Fabricated by Selective Laser Melting and Electron Beam Melting.*** **Rafi, H K, et al. 12, 2013, Journal of Materials Engineering and Performance, Vol. 22.**

17. ***Vickers Hardness of Cast Commercially.*** **da Rocha, Sicknan Soares, et al. 2, 2006, Braz Dent J, Vol. 17.**

18. Bhushan, Bharat. ***Introduction to Tribology.*** **New York : John Wiley & Sons, 2013.**

19. ***Wear in relation to friction — a review.*** **Kato, Koji. Tohoku, Japan : Elsevier, 2000, Wear, Vol. 241, pp. 151-157.**

20. ***Advanced mechanical properties of pure titanium with ultrafine grained structure.*** **Sergueeva, A. V., et al. s.l. : Elsevier, 2001, Scripta Materialia, Vol. 45, pp. 747-752.**

21. ***Friction and wear of titanium alloys sliding against metal, polymer, and ceramic counterfaces.*** **Qu, Jun, et al. s.l. : Elsevier, 2005, Wear, Vol. 258, pp. 1348-1356.**

22. ***The Effect of Microstructure on Fracture Toughness and Fatigue Crack Growth Behavior in g -Titanium Aluminide Based Intermetallics.*** **Campbell, J.P., Rao, K.T. Venkateswara and Ritchie, R.O. 2, s.l. : Elsevier, January 30, 1992, A Materials Science and Engineering, Vol. 149, pp. 143-151.**

23. ***The effect of microstructure on the mechanical properties of two-phase titanium alloys.*** **Filip, R., et al. s.l. : Elsevier, 2003, Journal of Materials Processing Technology, Vol. 133, pp. 84-89.**

24. ***Fatigue resistance of titanium with ultrafine-grained structure.*** **Semenova, I.P.: Salimgareeva, G. Kh., et al. 1-2, January 2009, Metal Science and Heat Treatment, Vol. 51, pp. 87-91.**

25. ***Deformation and failure behaviour of Ti-6Al-4V alloy under high rate shear loading.*** **Lee, W. S. and Huang, S. Z. Computational Ballistics II, Vol. 229.**

26. ***Plastic deformation and fracture behavior of Ti-6Al-4V alloy loaded with high strain rate under various temperatures.*** **Lee, Woei-Shyan and Lin, Chi-Feng. s.l. : Elsevier, 1998, Materials Science and Engineering, Vol. A241, pp. 48-59.**

27. ***A nanoindentation investigation of local strain rate sensitivity in dual-phase Ti alloys.*** **Jun, Tea-Sung, Armstrong, David E. J. and Britton, T. Benjamin. s.l. : Elsevier, 2016, Journal of Alloys and Compounds, Vol. 672, pp. 282-291.**

28. ***Mechanical Anisotropy and Stran Rate Dependency Behavior of Ti6Al4V Produced Using E-Beam Additive Fabrication.*** **Ladani, Leila, Razmi, Jafar and Choudhury, Soud Farhan. s.l. : ASME, 2014, Journal of Engineering Materials and Technology, Vol. 136.**

29. ***Strain rate response and wear of metals.*** **Biswas, S. K. and Kailas, S. V. 5, s.l. : Elsevier, 1997, Tribology International, Vol. 30, pp. 369-375.**

30. ***The Effect of Sliding Speed and Normal Load on Friction and Wear Property of Aluminum.*** **Chowdhury, M. A., et al. 1, International Journal of Mechanical & Mechatronics Engineering , Vol. 11.**

31. ***Metallography and Microstructures of.*** **Gammon, Luther M., et al. s.l. : ASME International, 2004, ASM Handbook, Vol. 9.**

32. Young, Warren C. and Budynas, Richard G. ***Roark's Formulas for Stress and Strain.*** **[ed.] Seventh. New York : McGraw-Hill, 2002.**